AURORAL ELECTRON PRECIPITATING ENERGY DURING MAGNETIC STORMS WITH PECULIAR LONG RECOVERY PHASE FEATURES

Flavia Reis Cardoso

Doctorate Thesis at Post Graduation Course in Space Geophysics, advised by Drs. Maria Virgínia Alves, Fernando Luiz Guarnieri, and George K. Parks, approved in november 29, 2010.

URL of the original document:
<http://urlib.net/ 8JMKD3MGP7W/38HLGUE >

INPE

São José dos Campos

2011

AURORAL ELECTRON PRECIPITATING ENERGY DURING MAGNETIC STORMS WITH PECULIAR LONG RECOVERY PHASE FEATURES

Flavia Reis Cardoso

Doctorate Thesis at Post Graduation Course in Space Geophysics, advised by Drs. Maria Virgínia Alves, Fernando Luiz Guarnieri, and George K. Parks, approved in november 29, 2010.

URL of the original document:
<http://urlib.net/ 8JMKD3MGP7W/38HLGUE >

INPE

São José dos Campos

2011

Aprovado (a)   pela Banca Examinadora
em cumprimento ao requisito exigido para
obtenção do Título de Doutor(a)   em

Geofísica Espacial

Dr.   Jonas Rodrigues de Souza
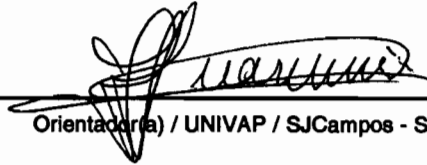
Presidente / INPE / SJCampos - SP

Dra.   Maria Virgínia Alves
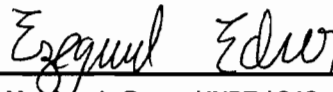
Orientador(a) / INPE / SJCampos - SP

Dr.   Fernando Luiz Guarnieri
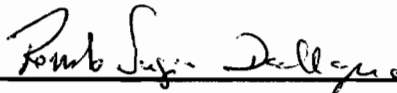
Orientador(a) / UNIVAP / SJCampos - SP

Dr.   Ezequiel Echer
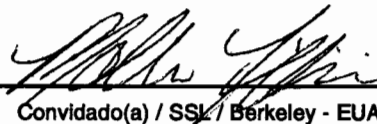
Membro da Banca / INPE / SJCampos - SP

Dr.   Renato Sérgio Dallaqua
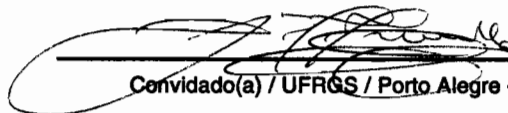
Membro da Banca / INPE / São José dos Campos - SP

Dr.   Matthew O. Fillingim

Convidado(a) / SSL / Berkeley - EUA

Dr.   Luiz Fernando Ziebell

Convidado(a) / UFRGS / Porto Alegre - RS

Aluno (a):   Flavia Reis Cardoso

São José dos Campos, 29 de novembro de 2010

"No meio do caminho tinha uma pedra
tinha uma pedra no meio do caminho
tinha uma pedra
no meio do caminho tinha uma pedra.

Nunca me esquecerei desse acontecimento
na vida de minhas retinas tão fatigadas.
Nunca me esquecerei que no meio do caminho
tinha uma pedra
tinha uma pedra no meio do caminho
no meio do caminho tinha uma pedra."

CARLOS DRUMMOND DE ANDRADE

To my mother, a fighter...

ACKNOWLEDGEMENTS

ABSTRACT

Aurora, light emissions generated by collisions between energetic electrons and atmospheric particles, is often seen in the polar region. Although much is known about the aurora, there are still many questions unanswered. For example, it is not well known what is the source of the energetic particles or by what processes the particles are energized. Understanding the behavior of the aurora is an important scientific problem because it provides information about the processes occurring during the solar wind-magnetosphere interaction. The auroral zone is significantly affected by magnetic storms and substorms. Occasionally, magnetic storms exhibit a long recovery phase which can last for several days. During such events, the auroral electrojet can display high-intensity, long duration activity. These events are known as HILDCAA events (High Intensity Long Duration Continuous AE Activity). The power input to the magnetosphere/ionosphere carried by precipitating electrons is an important parameter which can be estimated by the Ultraviolet Imager (UVI) on board the Polar satellite. This instrument monitors the spatial morphology and temporal evolution of the aurora in the far ultraviolet range in both sunlight and darkness. Applying the necessary instrument corrections and the dayglow removal, it is possible to evaluate the energy coming into the auroral zone. Our goal is to obtain quantitative information about the energy source for magnetic storms with long (LRP) and short (SRP) recovery phases by estimating the amount of precipitation energy input. Precipitation energy has been found highly variable for LRP. A significant energy input during long storm recovery phases implies additional energy source to maintain the magnetic activity in the auroral electrojet which is believed to be related to the fluctuating solar wind magnetic field and velocity. On the other hand, IMF (interplanetary magnetic field) remained southward for a while in SRP events. All the results suggest LRP could be a consequence of a solar wind driven system and SRP would be associated to an energy unloading process.

ENERGIA DE PRECIPITAÇÃO AURORAL DE ELÉTRONS DURANTE TEMPESTADES MAGNÉTICAS COM CARACTERÍSTICAS PECULIARES DE LONGA FASE DE RECUPERAÇÃO

RESUMO

Aurora, emissões geradas por colisões entre elétrons energéticos e partículas atmosféricas, é frequentemente observada na região polar. Embora muito se sabe sobre a aurora, ainda existem inúmeras questões sem respostas. Por exemplo, não se conhece qual a fonte das partículas energéticas ou por quais processos tais partículas são energizadas. A compreensão do comportamento da aurora é um problema científico importante porque provê informação sobre os processos que ocorrem durante a interação vento solar-magnetosfera. A zona auroral é significantemente afetada por tempestades magnéticas e subtempestades. Ocasionalmente, tempestades magnéticas exibem fase de recuperação longa que pode perdurar por vários dias. Durante tais eventos, os eletrojatos aurorais podem apresentar atividade de longa duração e alta intensidade. Esses eventos são conhecidos como eventos HILDCAA (*High Intensity Long Duration Continuous AE Activity*). A potência injetada na magnetosfera/ionosfera, carregada por precipitação de elétrons, é um importante parâmetro que pode ser estimado pelo instrumento *Ultraviolet Imager* (UVI) a bordo do satélite Polar. Esse instrumento monitora a morfologia espacial e a evolução temporal da aurora na faixa do ultravioleta distante em ambas condições de luz e escuridão. Aplicando as correções necessárias ao instrumento e a remoção de *dayglow*, é possível calcular a energia que chega à zona auroral. Nosso objetivo é obter informação quantitativa sobre a fonte de energia de tempestades magnéticas com longa (LRP) e curta (SRP) fase de recuperação, estimando a quantidade de energia de precipitação depositada. A energia de precipitação foi encontrada altamente variável para eventos LRP. Uma significante entrada de energia durante longas fases de recuperação de tempestades magnéticas implica em fonte de energia adicional para manter a atividade magnética no eletrojato auroral, o qual acredita-se estar relacionado com flutuações de velocidade e do campo magnético do vento solar. Por outro lado, o campo magnético interplanetário IMF permaneceu na direção sul por algum tempo em eventos SRP. Todos os resultados sugerem que os eventos LRP poderiam ser uma consequência de um sistema conduzido pelo vento solar e os eventos SRP seriam associados a processos de descarregamento de energia.

LIST OF FIGURES

xvii

CONTENTS

xxii

1 INTRODUCTION

Solar wind is continuously released by the Sun. However, the Sun is a very active region responsible by phenomena as coronal mass ejections, solar flares and fast-speed streams (BURLAGA, 1995). For this reason, solar wind is highly influenced by solar activity, which is known to be controled by a cycle of 11 years (KIVELSON; RUSSEL, 1995).

The planetary magnetic field is confined by the solar wind to a magnetospheric cavity, named magnetosphere (KIVELSON; RUSSEL, 1995). Solar wind pressure, mostly dynamic, establishes an equilibrium boundary with the earth pressure, primarily magnetic, known as magnetopause. Current systems and plasma featured regions are formed inside magnetosphere (PARKS, 2004).

Particles and magnetic field, known as interplanetary magnetic field (IMF), present in the solar wind, are believed to strongly influence the earth magnetosphere dynamics. Hence, phenomena occurring inside the magnetosphere are frequently atributed to the solar wind-magnetosphere coupling. As a consequence, geomagnetic activities, permeated by magnetic storms, substorms, and a more recent finding named HILDCAAs, deposit large amounts of energy into the magnetosphere. Geomagnetic activity is dicussed in section 1.1.

Auroral activity enhancements are also associated with energy deposition into the polar region. A main source of such energy input are the precipitating particles in the auroral zone which are responsible for the aurora triggering. UVI (Ultraviolet Imager) on board Polar spacecraft is capable of estimating the electrons deposition energy by the aurora emission measurements. A huge obstacle for that has been the solar contribution, known as dayglow, to the total emission. Solar radiation can be absorbed by the atmosphere resulting in excitation, dissociation and ionization, and can also be scattered by the molecules. Auroral activity and dayglow literature accomplishments are presented in sections 1.2 and 1.3.

1.1 Geomagnetic Activity

Geomagnetic disturbances are a consequence of the enhanced energy from the solar wind-magnetosphere coupling mechanism. Those activities affect directly magnetospheric current systems. Geomagnetic indices have been developed to measure the magnetic activity level through magnetic field perturbations produced by current intensity enhancements. Therefore, phenomena as magnetic storms, substorms and HILDCAAs, can be identified

and continuously monitored by the geomagnetic indices.

Geomagnetic storms are identified by the Dst index (SUGIURA, 1964) which is an instantaneous global average of the earth magnetic field horizontal component H (RUSSEL, 1991). Usually, a magnetic storm starts with an abrupt H component increase at the earth surface. This step may last for hours as it can be observed in Figure 1.1. The initial phase is then followed by a fast decrease corresponding to the main phase. Next, Dst index presents a fast recovery feature as a first stage, followed by a long and gradual recovery process. Typical magnetic storms last from one to five days. Initial phase can reach 25 hour duration, main phase can last about one day and recovery phase can extend for days (RUSSEL, 1991; GONZALEZ et al., 1994).
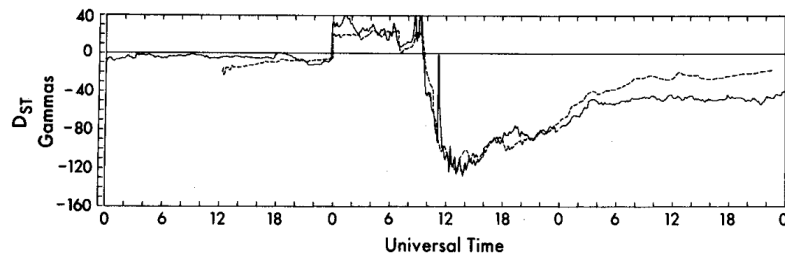
Figure 1.1 - Dst index profile during magnetic storm.
SOURCE: (KIVELSON; RUSSEL, 1995).

Initial phase features are produced by the magnetopause current enhancement (KIVELSON; RUSSEL, 1995). When solar wind dynamic pressure increases, the magnetopause is compressed and it moves toward Earth. Then, current intensity grows producing a northward directed magnetic field wich is added to the earth magnetic field and leads to the peak (positive values) observed in the Dst profile.

Particles injected into the magnetosphere are responsible by the ring current intensity enhancement, which, in turn, produces a magnetic field with direction opposite to that at the Earth's surface. Consequently, a decrease in the earth magnetic field horizontal component is noticed at the Dst profile. During recovery phase, dissipation processes in the ring current takes place and magnetic field intensity at the earth surface returns to pre-storm conditions.

The Dst index is also employed to measure the magnetic activity level. Magnetic storm

intensities are classified according to the Dst index as: weak for -30 nT to -50 nT interval, moderate for -50 nT to -100 nT, intense for values between -100 nT to -250nT, and finally, superstorms when Dst falls below -250 nT (GONZALEZ et al., 1994).

Besides magnetic storms, a shorter timescale phenomenon is identified in the magnetospheric dynamics, so-called substorm. This transient process initiates in the nightside and injects a significant amount of energy in the auroral ionosphere and magnetosphere (MCPHERRON, 1979; AKASOFU, 1964). As first step, named growth phase, energy is extracted from solar wind and stored in the magnetotail. Next, a fast energy release process takes place, which may be associated with aurora occurrence and auroral electrojet intensifications. This substorm expansion is estimated to last about one hour. Recovery phase brings back pre-substorm values during roughly 90 minutes.

The relationship between magnetic storms and substorms is a key issue within solar wind-magnetosphere-ionosphere coupling (SHARMA et al., 2003b; KAMIDE et al., 1998). Past theories pointed out that ring current enhancement related to magnetic storms would be a consequence of many substorms (SHARMA et al., 2003a). In this process, each substorm would inject particles from the plasmasheet which would be then trapped in azimuthal drift paths forming a symmetrical ring current. The current explanation is that the ring current system development results directly from a sustained enhancement of the convection electric field.

Observations suggest that ring current is not symmetrical during storm onset due to a partial ring current closing in part through the ionosphere and in part into the magnetosphere (SHARMA et al., 2003a). The enhanced cross-magnetospheric electric field produces Alfvén layers inward motion which pushes the ring current closer to the Earth and energizes the plasma as well. When the enhanced field decreases, particles fall into closed drift paths and the ring current becomes symmetric. The fast ring current decay during magnetic storm recovery phase can be related to plasma convection out of the system through open paths.

Occasionally, the ring current takes more time than usually to return to pre-storm conditions. This long magnetic storm recovery phase seen simultaneously with intense and continuous auroral activity is known as HILDCAA, from High Intensity Long Duration Continuous AE Activity (TSURUTANI; GONZALEZ, 1987). The auroral activity can be measured by the AE index, which monitors the horizontal component of the disturbed magnetic field in the auroral zone (ROSTOKER, 1972; DAVIS; SUGIURA, 1966). In fact, AE is a

composition of AL and AU indices, which are, in turn, a representation of the maximum magnetic perturbation generated by the westward and the eastward electrojet. HILDCAA events are then defined by some following criteria (TSURUTANI; GONZALEZ, 1987):

(1) *high intensity* - AE index peak must be higher than 1000 nT during the event;

(2) *long duration* - high and continuous AE activity must last for at least two days;

(3) *continuous* AE *activity* - AE index value must not fall below 200 nT for intervals longer than two hours at a time;

(4) the event must occur outside the main phase of a geomagnetic storm.

The intention of setting such strict criteria was to certify the presence of high intensity and long duration activity and also separate mechanisms generating HILDCAAs and magnetic storms (TSURUTANI; GONZALEZ, 1987). If a event does not fit within one or more criteria, there is still possibility that the physical processes are similar to those found during HILDCAAs (TSURUTANI et al., 2004).

Gonzalez et al. (1994) discuss the difference among magnetic storms, substorms and HILDCAAs, in terms of AE and Dst indices, and IMF z-component, as it is displayed in Figure 1.2. A modest southward IMF lasting about one hour is a sufficient condition leading to a substorm. Occurrence conditions for HILDCAAs also show a modest IMF magnitude. Intense magnetic storms take place under large amplitude Bz IMF and sustained duration. Tsurutani e Gonzalez (1987) conjectured the requirement for a geomagnetic storm occur was that IMF southward component should be less than -10 nT for at least three hours.

All known processes for ring current decay, as charge exchange, Coulomb collisions, convection, wave-particle interactions, have time scales of hours to fraction of days. In fact, such mechanisms can not explain magnetic storm recovery phases that last as long as days or weeks. Then, Tsurutani e Gonzalez (1987) pointed out a source to high intense auroral activity as an intermittent magnetic reconnection between southward component of interplanetary Alfvén wave fluctuations and magnetopause magnetic fields (TSURUTANI et al., 2004). Tsurutani et al. (1990) found that Alfvénic wave intervals were present over 60% of the time and the southward component of Alfvén waves was in good correlation with AE presenting a lag of 43 minutes.
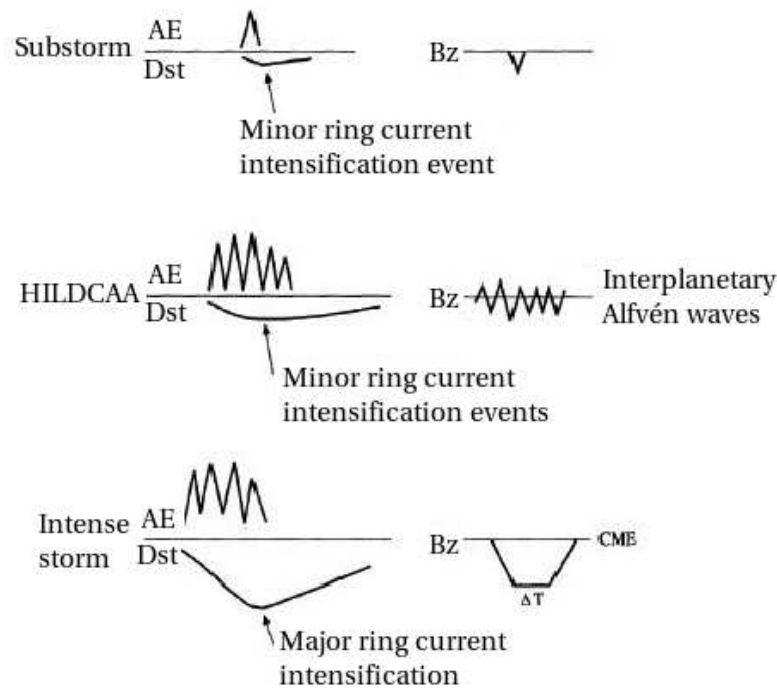
Figure 1.2 - Scheme of AE and Dst indices and southward IMF component for three classes of magnetic activity, substorms, HILDCAA and magnetic storms.
SOURCE: (GONZALEZ et al., 1994).

Large amplitude Alfvén waves are observed during corotating interaction regions (CIRs) (TSURUTANI et al., 1995; TSURUTANI et al., 2006). One third of the CIR events observed near Earth are geoeffective followed by moderate/intense magnetic activity (Dst<-50nT) (ALVES et al., 2006). Such structure is generated by fast speed streams interacting with the slower solar wind streams ahead of them. High-speed streams are emanated from coronal holes in the Sun which, in turn, are well developed during the declining phase of the solar cycle.

Soraas et al. (2004) discuss that Dst index is in good correspondence with ring current particle injections during a magnetic storm. Hence, a long recovery in the Dst would be a consequence of particle injection. Also, AE index exhibits a good correlation with ring current particle injections. Apparently, HILDCAA events are associated with injection of protons into the outer portion of the ring current. Then, a slow decay in the Dst index is not related to other magnetospheric current systems or to a slower decay rate of the ions in the ring current. When the injection occurs during a storm recovery phase there is a delay in the Dst recovery and when it occurs out of a storm, Dst can maintain negative

5

values for long intervals.

Tsurutani et al. (1995) proposed that consecutive injections caused by substorms were related to the prolonged Dst recovering during HILDCAAs. Later, Tsurutani et al. (2004) worked on the relation between AE and -AL indices and substorm onsets using auroral images from POLAR Ultraviolet Imager (UVI). They found no correlation between substorms and AE/AL intensifications although substorm expansion phases can occur simultaneously to HILDCAAs. Then, they suggested that repetitive particle injections are caused by enhanced inward convection due to dawn-to-dusk electric fields during southward intervals of the Alfvén wave trains.

AE and AL indices also measure changes in convection, which is not a generator mechanism of a substorm, and therefore, may not be a good substorm indicator (KIM et al., 2008). Besides of that, the use of global quantities may not be a reasonable mean to describe local processes. In fact, auroral indices, as AE/AL, and ring current indices, as Dst, are not the ideal tools on the spatial investigation of substorm particle injections (SHARMA et al., 2003b). Kim et al. (2008) investigated the contribution of substorms to the particle injections using LANL (Los Alamos National Laboratory) electron flux data and global auroral images from WIC (Wideband Imaging Camera) on board IMAGE. Results showed large majority of repetitive particle injection during HILDCAA events are associated with substorm onsets.

Lee et al. (2006) pointed out that substorms are related to successive northward turnings of Alfvén waves during HILDCAA phenomena. This indicates that repetitive featured substorms related to high-speed streams are triggered by the IMF. Apparently, substorms are responsible by plasma sheet particles motion toward the inner magnetosphere, and consequently, consecutive particle injections associated with substorm onsets may contribute to long Dst recovery. On the other hand, enhanced earthward convection during repetitive southward intervals of the Alfvénic IMF is also a likely mechanism. Therefore, consecutive substorms and enhanced convection driven by large amplitude Alfvén waves within fast-speed streams may play an important role in HILDCAA events (KIM et al., 2008).

1.2 Auroral activity

The optical spectrum of an aurora extends from ultraviolet to infrared with large quantitities of line and band features (KIVELSON; RUSSEL, 1995). Auroral light is emitted by excitation process derived from atmospheric and precipitating particle collisions. Such mechanism can be divided in two steps. First, precipitating energetic auroral particles convert kinetic energy to chemically excited states of atmospheric species through collision process. Thus, the chemically excited states relax and release photons of wavelengths determined by the energy transition.

When precipitating auroral particles are electrons, the resulting emissions are named electron aurora. Precipitating protons create secondary electrons, which, in turn, also collide with atmospheric constituents and excite them to energetic states in the same way as primary electrons. Such emission is also an electron aurora. There is no way to distinguish the species of precipitating particles without additional information (FREY, 2007).
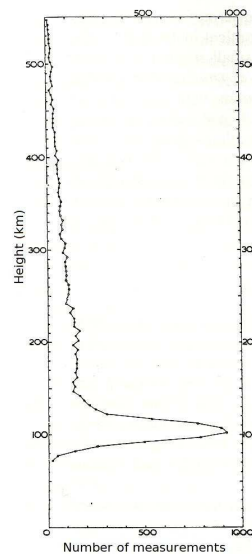
Figure 1.3 - Height (km) versus number of measurements in a statistical distribution of 12,330 height measurements of the northern lights.
SOURCE: (STORMER, 1955).

The auroral light contains atomic lines and molecular-band spectra of the main upper atmosphere constituents and also from minor species, and for this reason, it is considered the "fingerprint" of the atmospheric composition (KIVELSON; RUSSEL, 1995). Hence, the

auroral height distribution depends on the precipitating particles energy and pitch-angle distribution as well as on the atmospheric constituents. The distribution of 12,330 auroral source points of northern lights is displayed in Figure 1.3. As observed, auroral arcs and bands lie mostly within the height interval of 95-150 km.

As auroral emission results from the excitation mechanism caused by electron impact, this emission is found to be proportional to the energy deposition into the atmosphere. Thus, the energy input into the polar region can be estimated from light emission in the auroral atmosphere.

Lummerzheim et al. (1997) studied the energy input in the auroral region using hemispheric power quantity derived by NOAA/TIROS and the energy calculated from images obtained by Polar Ultraviolet Imager (UVI). Hemispheric power is estimated from particle precipitating energy flux along the satellite track extrapolated for the entire auroral oval through statistical precipitation patterns. Energy flux can also be extracted from UVI images with a better resolution than hemispheric power. Even though the images are within ultraviolet range there is still some solar contribution (dayglow) besides aurora in the UVI data. Dayglow is the topic of the next section. The data is organized according to solar zenith angle (SZA) values, and the average is obtained for each bin. Pixels into the auroral zone are excluded. Then, the brightness average for each bin is subtracted from pixels with the same SZA. Hemispheric power exhibits a satisfactory agreement with UVI energy flux. However, this quantity can miss entire substorms or under/overestimate it due to limited sampling.

Besides auroral emission, electron precipitation affects the ionospheric energy deposition directly by ionization and *bremsstrahlung* X-rays production, and indirectly by Joule heating through ionospheric Pederson conductance increase. Ostgaard et al. (2001) used Polar Ionospheric X-ray Experiment (PIXIE) and UVI images to derive total energy dissipation by electron precipitation. The comparison of such quantity to geomagnetic indices during substorms shows a nonlinear relation between energy dissipation and AE as well as with AL index (OSTGAARD et al., 2001). Energy flux is found to be well correlated to AL which indicates that electron precipitation modulates the westward electrojet intensity by affecting the Hall conductance. On the other hand, AU index exhibits a poor correlation with the energy flux. This result suggests that there is an electric field dominance in the dusk sector which affects only slightly the eastward electrojet conductance.

Evidences show that electron precipitation and X-ray micropulsations occur almost simul-

taneously troughout the auroral zone during a substorm. Parks et al. (1968) showed that electron injections and micropulsations have different temporal signatures for each local time through X-ray baloon measurements in high-latitude regions. Each specific form of these both phenomena is probably associated with a phase of the substorm development (CORONITI et al., 1968). Thus, substorm is present not only in auroral disturbances but also in electron precipitating and micropulsation activity (MCPHERRON et al., 1968). In fact, this indicates that magnetospheric dynamical processes determine the local time features of the substorm.

Polar cap area variability also has connection with magnetospheric dynamics. Brittnacher et al. (1999) worked on the area of the polar cap, as a function of local time and substorm phase for different IMF values during three substorm events, using POLAR UVI. They found that polar cap size expands during the substorm growth phase due to a decrease of particle precipitation. Also, polar cap increase is seen independent of the southward IMF component intensity. In summary, polar cap boundary is strongly influenced by oval thinning, decrease in polar cap structures, the poleward expansion of the substorm at midnight and the fading of luminosity below the instrument sensitivity treshold.

Some auroral intensifications present different characteristics than those known for substorms. Short-lived auroral intensification which does not expand in the auroral region is called pseudobreakup. Fillingim et al. (2000), Fillingim et al. (2001) and Parks et al. (2002) worked on these events through ion and electron distribution functions and magnetic field measurements in the magnetotail from Wind satellite when its ionospheric footprint observed by Polar was associated with auroral brightenings. They found that plasma sheet dynamics present the same features during pseudobreakups and substorms. This behavior indicates that an auroral disturbance feature is determined in another region, possibly in or above the ionosphere (auroral acceleration region).

Chua et al. (2004) worked on IMF and seasonal variations during substorms using hemispheric power computed from Polar UVI. They showed that southward IMF component implies in longer substorm expansion phases and greater peak hemispheric power than northward IMF component. The timescale of substorm recovery does not depend significantly on IMF z-component variation although it is influenced by seasonal changes. In fact, substorm timescales are found to be more sensitive to IMF Bz orientation during summer. Seasonal variation leads to the implication that auroral intensifications may develop differently in northern and southern hemispheres. Hence, results suggest that ionosphere plays an important role in the auroral dynamics.

Aurora is actually observed as asymmetric when comparing northern and southern hemispheres. Ostgaard et al. (2007) found that cusp auroras are controlled by IMF y-component and dipole tilt angle. Substorm onset locations are also seen as asymmetric in both hemispheres and governed mainly by IMF clock angle. Fillingim et al. (2005) suggested that a strong IMF y-component modifies the ionospheric convection and field aligned current patterns leading to an auroral asymmetry.

Parks et al. (2000) studied the aurora behavior when the solar wind nearly disappeared, that is, solar wind density reached unusually small values (0.2/cc). The aurora was seen at higher magnetic latitudes which indicates that electron precipitating source moved north-ward as the geomagnetic activity decreased. They found that solar wind density alone is not a primary parameter controlling the auroral activity.

During geomagnetically disturbed conditions the energy transfer into the ionosphere is mostly carried by electromagnetic waves and particle precipitation. Alfvén waves may then play an important role in the energy transfer mechanism to the auroral region. Wygant et al. (2000) showed that perpendicular electric fields in the plasma sheet boundary layer (PSBL) at $4 - 6R_E$ were associated with Alvén waves for two cases measured by Polar satellite. Such waves carried large and sufficient Poynting flux toward the ionosphere to power magnetically conjugate auroral emissions. Figure 1.4 is a cartoon of a magnetic flux tube exhibiting the incident Alfvénic Poynting flux being converted to energyzed particles and joule heating in the ionosphere.

Keiling et al. (2002) investigated 40 plasma sheet crossings by Polar and also concluded that Afvénic Poynting flux in the midtail region is associated with and capable of pow-ering localized regions of magnetically conjugated aurora. Large Alfvénic Poynting flux often occurs in the plasma sheet boundary layer during the expansion phase of substorms (KEILING et al., 2000). Thus, auroral phenomena have been connected to energy transfer processes by large Alfvén waves in the PSBL.
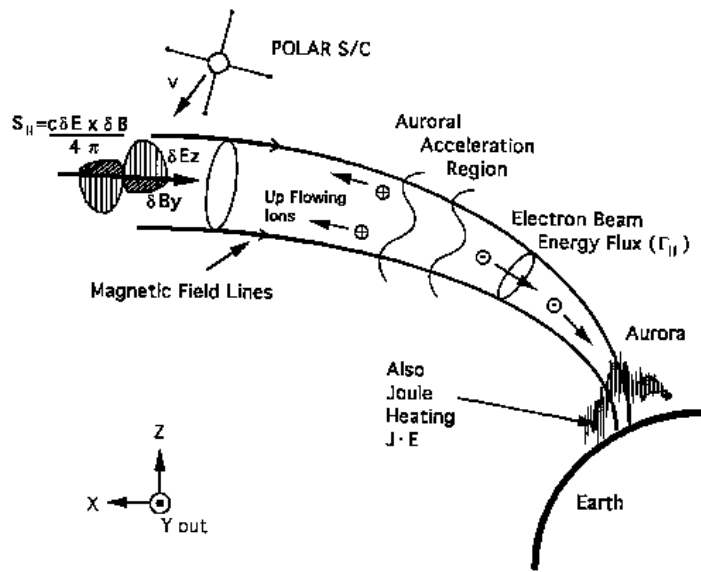
Figure 1.4 - Cartoon of incident Poynting flux converted to aurora and joule heating of the iono-
sphere.
SOURCE: (WYGANT et al., 2000).

1.3 Dayglow

Sun is the dominant energy source for terrestrial atmosphere. Solar radiation can be absorbed by the atmosphere resulting in excitation, dissociation and ionization. Usually, fluorescence is a consequence of those processes and it is commonly known as airglow. When the atmosphere is sunlit, the dayside airglow is known as dayglow.

Excitation of electronic transitions between ground and excited states of an atom or molecule results in resonance fluorescence. Hence, the emission rate is proportional to the species concentration. Resonance emission lines of the atomic and molecular components of the thermosphere (N_2, O_2, O, O^+ and minor species) are mostly in the ultraviolet region of the airglow spectrum (MEIER, 1991).

Figure 1.5 displays Earth ultraviolet dayglow spectrum divided in EUV, FUV, MUV and NUV, which means extreme, far, middle and near ultraviolet, respectively. Regions of absorption by oxygen species are indicated by thick horizontal lines. Emission band intervals are presented for N_2 and NO while for atomic and ionic species the stronger emission lines are exhibited. Those lines and bands contain signatures of major and minor atmospheric species concentration and information about the excitation mechanism strengths.

11
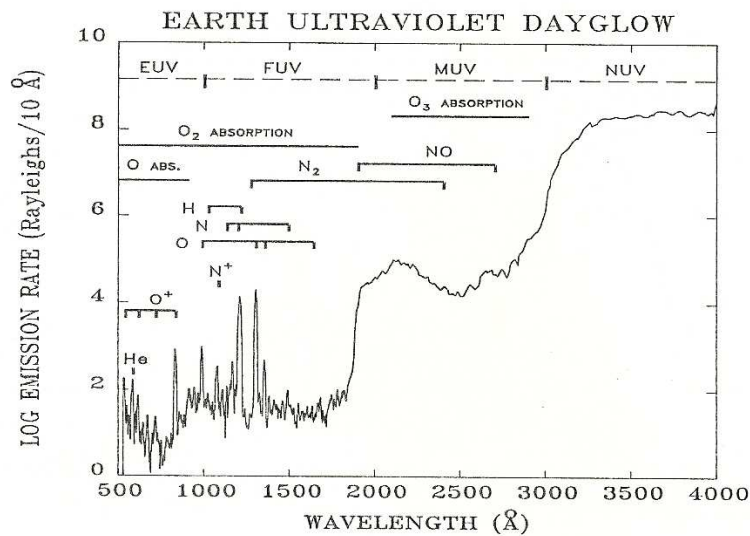
Figure 1.5 - Earth dayglow spectrum adjusted to nadir view from 200 km at midmorning. SOURCE: (MEIER, 1991).

Only a small fraction of the solar radiation below 3000 Å reaches the ground. Atomic oxygen lines are seen at 1304, 1356 and 1641 Å and the strongest nitrogen lines are located at 1134, 1168, 1177, 1200 and 1493 Å. The excitation of these nitrogen lines are a consequence of electron impact on N and N_2 and photodissociation of N_2.

N_2 Lyman Birge Hopfield (LBH)-band lies in the FUV and presents behavior of photoelectron-excited dayglow emissions. Figure 1.6 shows N_2 LBH-band vertical column emission rate in the nadir view versus solar zenith angle for OGO-4 satellite. Emission rates are of order of 4 to 8 kR for the entire LBH-band system. Variation in the sunlit atmosphere roughly follows the cosine of the solar zenith angle.

Under darkness condition, the airglow is known as nightglow. This fluorescence is produced by atom-atom and ionic recombination. Figure 1.7 represents ultraviolet nightglow in an emission rate versus wavelength plot. As it can be observed, there are apparently no emissions in between the features. In the past, N_2 LBH-band emissions were supposed to be nightglow, but afterwards, that was inferred to the spacecraft-atmosphere interaction (MEIER, 1991).

Craven et al. (1994) worked on FUV dayglow after an interval of intense geomagnetic activity and noticed a localized 55% decrease in the dayglow brightness in the morning
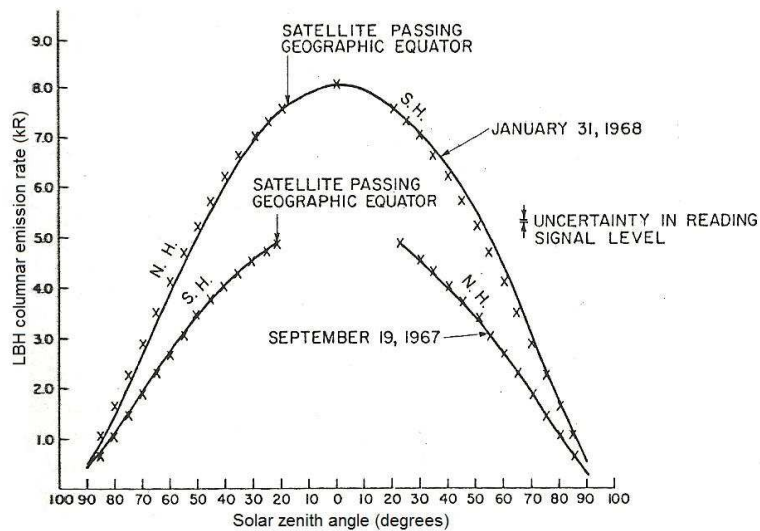
Figure 1.6 - N_2 LBH-band emission rate in the nadir view by solar zenith angle for OGO-4 satellite. Prinz and Meier, 1971.
SOURCE: (MEIER, 1991).
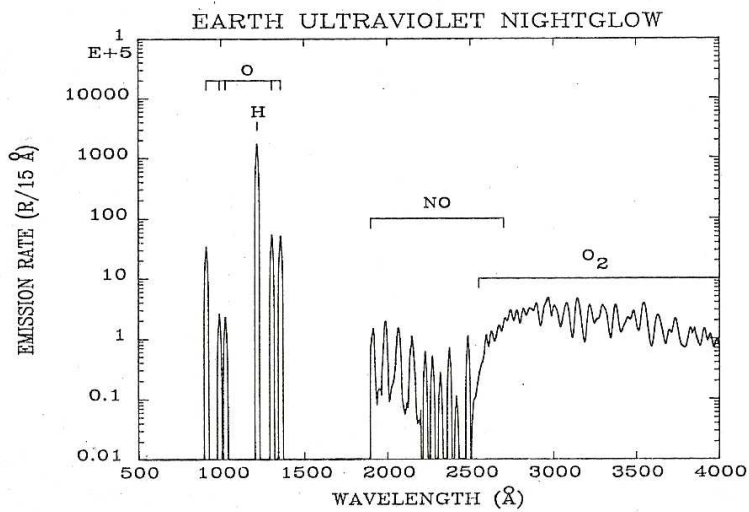
Figure 1.7 - Composite UV nightglow spectrum for 600 km altitude in a nadir viewing and equatorial plane.
SOURCE: (MEIER, 1991).

sector at 130.4 nm. They atributed such reduction to the auroral heating which causes a decrease in column density of O relative to N_2.

Meier et al. (2002) studied ionospheric and dayglow response to the radiative phase of the Bastille day flare, occurred on July 14, 2000. Figure 1.8 shows the atmospheric response at the peak of the flare obtained by AURIC (Atmospheric Ultraviolet Radiance Integrated Code) model. Dot lines refer to pre-flare values while the solid lines are related to the peak of the flare. Left panel presents total photoionization and heating rate versus altitude. Right panel shows excitation rates of N_2 LBH and OI 98.9 with the altitude as well. The photoionization rate behaves qualitatively similar to excitation rates on the right panel, since these dayglow emissions are produced by impact excitation. There is a noticeable difference on the pre-flare and the peak values. EUV (extreme ultraviolet) is estimated to increase 50% during the flare, which is comparable to solar cycle minimum to maximum variation. The X-radiation increase is given by a factor of 200.
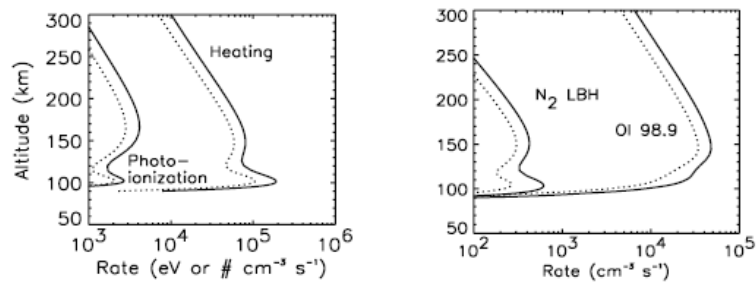
Figure 1.8 - Atmospheric response at the peak of the Bastille day flare obtained by AURIC model. Left panel presents total photoionization and heating rates versus altitude. Right panel shows excitation rates of N_2 LBH and OI 98.9 with altitude. Dot lines refer to pre-flare values while the solid lines are related to the peak of the flare.
SOURCE: (MEIER et al., 2002).

1.4 Objectives

It is known that some magnetic storms present peculiar long recovery phase features. On the other hand, all known processes for ring current decay, as charge exchange, Coulomb collisions, convection, wave-particle interactions, have time scales of hours to fraction of days. In fact, such mechanisms can not explain magnetic storm recovery phases that last as long as days or weeks.

A relatively recent magnetospheric phenomenon named HILDCAA (High intensity long duration continuous AE activity) is believed to be responsible for longtime magnetic storm recovery phases (TSURUTANI; GONZALEZ, 1987). During this intense and long auroral activity process, large amounts of energy are deposited into the magnetosphere/ionosphere.

The main objective of this work is to calculate the auroral energy deposition by precipitating particles during magnetic storms with long (LRP) and short (SRP) recovery phases. This procedure provides quantitative information about the energy injection and also about the differences between short and long (HILDCAA) recovery phases in magnetic storms. Energy input is estimated through ultraviolet images obtained by UVI instrument on board Polar spacecraft. Applying spacecraft position corrections and dayglow removal on the UVI images, it is possible to evaluate more accurately quantitative energy.

Also, it is important to understand the energy transfer mechanisms present during magnetic storms. The way as precipitating particles relate to magnetospheric currents and to solar wind parameters can yield clues about the magnetospheric dynamics. This could be a step for reaching coupling processes knowledge and permiting space weather predictions in future. Energy carried by the solar wind could be monitored ahead of the Earth's magnetosphere and then continuously would inform the magnetosphere state.

Specifically, our objectives are described in details as follows.

a) Our main objective is to obtain quantitative information on the auroral electron precipitating energy for magnetic storms through LBH long Polar UVI images. In order to achieve that, an accurate dayglow model has to be developed.

b) To stablish the differences between SRP and LRP magnetic storms in terms of electron precipitation energy.

c) To investigate the relation between precipitation energy input and auro-

ral/equatorial magnetospheric current systems during SRP and LRP events.

d) To calculate power input from different methods and compare to that obtained from UVI images. One method derive precipitation energy from geomagnetic indices through linear and nonlinear empirical relations. The other method is obtained from particle influx observations by NOAA-POES spacecraft particle detector.

e) To compute the magnetosphere-solar wind coupling energy parameter derived from empirical relation and compare to UVI auroral precipitation energy. Here we investigate the role of the solar wind conditions in the electron precipitation during SRP and LRP magnetic storms.

f) To investigate the spatial evolution of the aurora during the selected phenomena.

g) To verify the solar wind conditions during each event.

This thesis is organized as follows. The methodology of this work is presented in Chapter 2, where the instruments are described in Section 2.1, the necessary data treatment is explained in Section 2.2, our auroral energy estimate derived from UVI images is detailed in Section 2.3, the hemispheric power obtained by NOAA POES is found in Section 2.4, and, finally, the selection of magnetic storms is displayed in Section 2.5. The characteristics of the events, which are divided in two groups, SRP and LRP featured, are described in Chapter 3. Our results are separated in three parts. First, we present auroral energy input for SRP and LRP events in Chapter 4, which describes UVI energy estimate and its relation with geomagnetic indices, the energy input calculated from empirical equations based on geomagnetic indices and hemispheric power obtained by NOAA POES. Next, spatial features of the aurora are shown in Chapter 5. Last, we investigate the influence of the solar wind in the auroral energy input in Chapter 6, by calculating solar wind energy input and analyzing solar wind parameters. Finally, Chapter 7 brings our conclusions.

2 METHODOLOGY

2.1 Instrumentation

Aurora is the emission light resulting from particle collisions and it is generated throughout the spectrum, from the X-ray to the infrared. Much of the past works about aurora used to be imaged in visible light (TORR et al., 1995). For this reason, usually, studies were restricted to nightside and twilight auroras due to the bright scattered sunlight on the dayside of the Earth. Even using ultraviolet images, data had to be limited to conditions of large solar zenith angles. The same problem of scattered long wavelength sunlight remains in the far ultraviolet range (FUV), and filtering in the FUV was not really well developed at that time. Moreover, the past known instruments did not have a despun [1] platform capability. Because of that, earlier images had to be obtained taking into account the spacecraft spin, orbital motion and mirror scaning.

The qualitative study in auroral image data have developed rapidly over the past three decades. However, the field of quantitative imaging is relatively new. The Ultraviolet Imager (UVI) was developed to provide quantitative study of the auroral region. Such instrument is on board Polar spacecraft belonging to Global Geospace Science (GGS) which, in turn, is a part of the International Solar-Terrestrial Physics (ISTP) program (NASA, a) .

The auroral images used in this work are obtained from the UVI instrument. The Polar spacecraft and the UVI are described in the following sections.

2.1.1 Polar spacecraft

Polar spacecraft was launched on February 24, 1996 (NASA, b). Its orbit spends 18 hours and it is highly elliptical, with perigee at 1.8 R_E and apogee at 9 R_E. The satellite was initially in the inclination of $86°$ and it precessed slowly at a maximum rate of $10°$ per year to higher latitudes, passed over the north pole and continued southward to lower latitudes.

Problems identified in the deployment of one of the Polar's electric field booms resulted in a spacecraft despun platform wobble of a period about 6 seconds, which affects the imagers located in that place. The wobble effect is smearing the image of about 10 pixels in the wobble direction since the image integration time is roughly 37 seconds. Such effect is not always seen in auroral images but it can be easily identified when the imager

---

[1]A despun platform does not rotate with the spacecraft.

is looking at the stars, the fixed bright sources. The auroral emissions are not constant during the image integration as the stars, and for this reason, the image is not smeared (GERMANY et al., 1998).

2.1.2 Ultraviolet Imager (UVI)

UVI is a small sophisticated camera with a two-dimensional intensified-CCD detector (TORR et al., 1995) (NASA, c). The imager is mounted on a pointable despun platform which permits continuously auroral imaging as the spacecraft rotates. This system operates in the far ultraviolet, over a wavelength range from 1300 to 1900 Å. Also, the instrument presents a wide field of view and a filter wheel to select one of the five available far ultraviolet spectral regions for imaging.

The spatial resolution and the extent of coverage vary significantly during the 18 hour orbit. The highly eccentric Polar orbit spend about 9 hours at distances greater than 6 R_E from the Earth, when it is possible to image the entire oval over a timescale much longer than the characteristic time related to auroral phenomena. The field of view required for those conditions is about 8°. The two-dimensional image is a 224 by 200 pixels array across the two perpendicular diameters of the circular field of view, which yields a per pixel spatial resolution of 0.036° in one direction and 0.04° in other direction. The choice of field of view is a trade-off between spatial resolution and global coverage.

The imager is capable of measuring features under both sunlit and nightside conditions simultaneously. In order to make it possible, the instrument is constituted by filters which measure only the features of interest. First, the visible scattered sunlight has to be reduced by a factor of 10^9 through instrument filtering. Although the FUV component of the scattered sunlight (wavelength < 3000 Å) is very weak when compared to longer wavelengths, it is still significant within FUV weak emissions range and should also be avoided. All of that requires that the filters contain stray and out-of-band light rejection besides of narrowband FUV interference filters.

Five filters are used to isolate emissions from atomic oxygen (OI) multiplet lines at 1304 Å and at 1356 Å, N_2 Lyman Birge Hopfield (LBH) separated in long (LBHl 1400-1600 Å) and short (LBHs 1600-1800 Å) wavelength ranges, and long wavelength scattered sunlight. Figure 2.1 shows the bandpasses of the five filters used in the UVI instrument over the high latitude vacuum ultraviolet spectrum of the dayside features in a soft aurora condition.
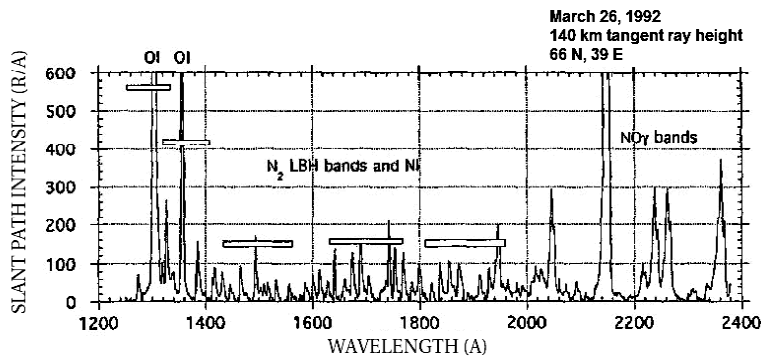
Figure 2.1 - High latitude vacuum ultraviolet spectrum of the dayside features in a soft aurora condition and the bandpasses of the five filters used in the UVI instrument. SOURCE: (TORR et al., 1995).

The most prominent ultraviolet auroral emissions are the OI multiplets at 1304 Å and 1356 Å and the N_2 Lyman Birge Hopfield (LBH) bands, with the exception of HI Lyα (Hydrogen Lyman-α emission line) at 1216 Å (GERMANY et al., 1990) (GERMANY et al., 1994). The OI 1304 Å emission is attenuated due to its high efficiency for multiple scattering, and for this reason, its use for auroral imaging is limited, in spite of its possible use as an indicator of oxygen concentration. The multiple scattering for OI 1356 Å and N_2 LBH emissions can be ignored, because the multiple scattering efficiency is small in these cases. The OI 1356 Å emission is highly absorbed by O_2, in the Schumann Runge continuum, which makes the emission intensity vary with the penetration depth (increasing energy) of the incident electrons since O_2 density changes with the altitude.

The N_2 LBH emission is a result of the excitation mechanism by electron impact because this emission is a dipole electric forbidden transition. Therefore, the LBH emission intensity is directly proportional to the auroral energy flux injected by particle precipitation into the atmosphere, neglecting the photoelectrons produced on the dayside (TORR et al., 1995) (GERMANY et al., 1990) (GERMANY et al., 1998). However, the LBHs emission is attenuated in the atmosphere because shorter LBH wavelengths still lie in the range of the O_2 absorption. Then, the LBHs emission varies with particle precipitation depth penetration, and in other words, with the energy of the injected particles. Those production and loss processes dependent on particle mean energies allow the use of such emission as a diagnostic of mean energy. On the other hand, as these loss processes are not present in the LBHl wavelength range, the LBHl emission is more indicated to measure the energy flux.

19

The LBHl emission would be then exclusively dependent on energy flux and totally independent of average energy as modeled by Germany et al. (1990) (GERMANY et al., 1994) . In this model, the LBH is modeled as an ideal case of two LBH bands, one at the wavelengths where there is absorption and the other one where attenuation is ignored. But, in practice, the LBH bandpass ranges are constituted by many bands with consequently different loss factors.

Figure 2.2 shows modeled vertical column brightness versus mean energy, for a Gaussian energy distribution with an influx energy of 1 mW/m^2, considering the UVI instrumental bandpass (GERMANY et al., 1998). In this more realistic case, the LBHl emission intensity changes by roughly 10% between 1 and 10 keV, and therefore, it leads to the fact that LBHl emission presents a weak dependence on average energy. Also, the same model shows a small dependence on other variables as diurnal, seasonal, magnetic activity and neutral atmospheric composition changes. Thus, as all the effects mentioned are negligible, they can be ignored for the energy calculation.
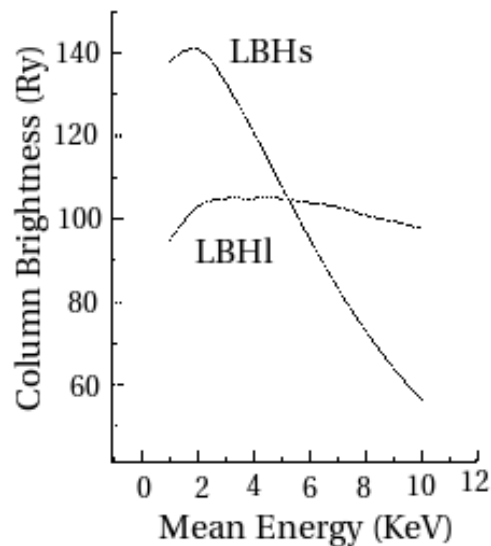
Figure 2.2 - Modeled vertical column brightness versus mean energy for LBHl and LBHs wavelength range.
SOURCE: (GERMANY et al., 1998).

Correct photometric calibration of the UVI instrument, performed in laboratory and also from the spacecraft in orbit, permits that the UVI response to be directly related to the

emission brightness. Before the UVI instrument counts can be converted to photon emission flux ($photons \times cm^{-2} \times s^{-1}$), some special care about calibration is needed. The photons background should be removed because when the UVI is closed up there are still counts of photons. The pixel intensities shoud be homogenated since some pixels are found brighter even if exposed to the same emission intensity. Each filter and each integration interval should be calibrated taking into account the gain of the instrument for each case.

The LBHl emission measured as photon flux ($photons \times cm^{-2} \times s^{-1}$) can then be converted into nadir surface brightness (*Rayleighs*) by a factor of 30.17 (1 $photons \times cm^{-2} \times s^{-1}$ = 30.17 *Rayleighs*). In turn, the surface brightness can be converted into injected energy flux ($ergs \times cm^{-2} \times s^{-1}$), considering the almost linear proportion between these two quantities as it can be observed in Figure 2.3 (GERMANY et al., 1998). The variation of LBHl emission with mean energy can be neglected, as discussed previously. Therefore, the relation between LBHl emission and energy flux is 1 $photons \times cm^{-2} \times s^{-1}$ = 30.17/110.0 $ergs \times cm^{-2} \times s^{-1}$.
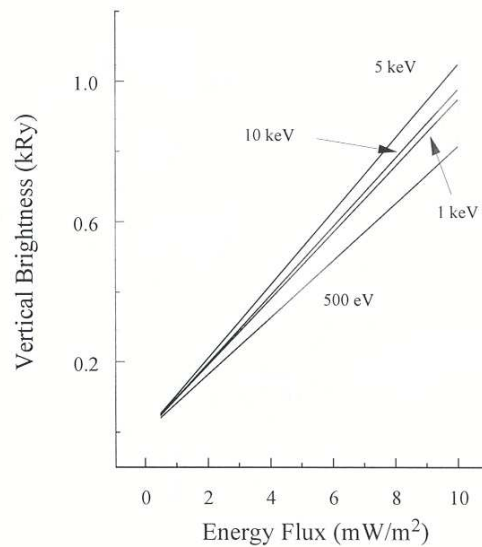
Figure 2.3 - Modeled vertical column brightness versus energy flux for mean energies of 0.5, 1, 1.5 and 10 keV.
SOURCE: (GERMANY et al., 1998).

2.2 Data treatment

The key point of this work is to estimate quantitatively the energy deposition by particle precipitation through auroral emissions in the UVI images. In order to achieve that, some steps had to be performed: raw UVI images need to be calibrated and corrected, and solar contamination must be removed from the data. In other words, images must have both instrumental and solar backgrounds removed before analysis.

LBHl emissions in UVI images are directly proportional to electron precipitating energy and, for this reason, are indicated for quantitative studies. Spacecraft line of sight (LOS) correction is applied to all LBHl images. Such correction changes the image for a nadir view perspective, removing the apparent brightness enhancement effect caused by the spacecraft view angle. The LOS correction method is presented below.

LOS corrected UVI images include auroral emissions and also undesirable solar contribution. Therefore, aurora energy estimate is obtained by removing the solar contribution from the measured energy. We developed a method to estimate the dayglow energy, and then, calculate the auroral energy. As our interest in this work is a quantitative analysis, we had to be careful about the accuracy of our method. Our dayglow estimate method will be described later.

2.2.1 LOS correction

The spacecraft view angle changes during the orbit time, and as a consequence, the apparent emission brightness as well. The line of sight (LOS) emission intensity increases with the instrument look angle due to the enlargement of the optical length path through a given column-integrated emission layer (GERMANY et al., 1998). The spacecraft look angle θ is defined as the angle between the line at the emission point which goes down to the center of the Earth (local zenith) and the line connecting the emission point to the satellite.

Figure 2.4 shows LOS brightness intensity versus spacecraft look angle for LBHl and LBHs band emissions with a mean energy of 10 keV. Each modeled point is associated with a single pixel in the UVI field of view. The cosine line seen in Figure 2.4 is the LOS intensity enhancement caused only by geometric factors. For the LBHl emission, the brightness increase behavior is close to cosine, although it presents a slight difference caused by a non-geometric component. The enhanced O_2 absorption along the slant path becomes a competition factor with the augmented emission, which results in an emission

intensity value less than expected by the LOS geometry (GERMANY et al., 1998). Such loss processes are addressed to the shorter wavelengths of the LBHl band. The absorbed wavelengths are a negligible part of the total LBHl band, and thus, it is a small effect for the LBHl filter. On the other hand, the LBHs band emission is extremely affected by the slant path and can not be corrected by the LOS geometry.
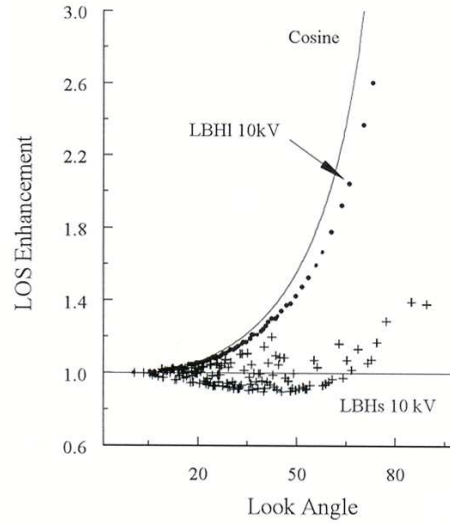
Figure 2.4 - Modeled LOS brightness intensity versus spacecraft look angle for LBHl and LBHs band emissions with a mean energy of 10 keV. Each modeled point represents an observation corresponding to a single pixel of the UVI field of view. The cosine line is the LOS intensity enhancement caused by only geometric factors.
SOURCE: (GERMANY et al., 1998).

UVI LBHl images can be corrected by the LOS geometry factor then. This correction changes the image for a nadir view perspective (null look angle), replacing the spacecraft position to the end of a vertical line (local zenith) passing through the emission point. An empirical fit of the cosine line and the LBHl LOS enhancement is given by (GERMANY et al., 1998):

$$LOS = \frac{e^{0.06(1-\frac{1}{cos\theta})}}{cos\theta}.$$
(2.1)

In this work, LOS correction, determined by Equation 2.1, is applied to all UVI images, since we use the LBHl filter.

2.2.2 Dayglow estimate method

UVI images contain auroral emissions and solar bright contribution as well. The solar contamination, known as dayglow, is generated by photoelectrons produced by solar EUV (Extreme UltraViolet) radiation and scattered solar UV (UltraViolet) photons. The UVI instrument on board Polar satellite was built carefully in order to reduce drastically the dayglow on the data. Despite of that, there is still some solar contribution which should be removed, if the auroral energy estimate is desirable.

First, it is necessary to estimate the dayglow energy in order to be able to remove it from the UVI images. An important assumption here is that pixels with the same solar zenith angle (sza) present the same dayglow intensities (solar zenith angle is defined between the pixel-Sun line and the local zenith). For this reason, the dayglow estimate is approximated as only a function of sza.

The data used in the dayglow estimate as well as in the events occurrence are restricted for the year of 1998. Along the year, the sunlit region changes due to the Earth's axis tilt variation. In this case, the region imaged by UVI was the north pole. Dayglow is then estimated by binning image pixels by solar zenith angle. Somehow, auroral emissions had to be excluded from this calculation. In this work, the UVI images were chosen carefully so there was no auroral contribution on the data. This was quite a challenge because auroral region presents some magnetic activity most of the time. For this reason, auroral contribution is considered negligible when UVI images present really low magnetic activity.

A set of 1,308 UVI images was used for gathering pixels according to sza. The power average was calculated for each sza bin allowing the dayglow energy be estimated in function of sza. UVI energy, obtained in photon flux units, were converted to units of power to obtain energy average. The power quantity has no dependence on area, as energy flux, and can be easily summed. Power average was then divided by the pixel area in order to get dayglow in units of energy flux. Figure 2.5 shows the dayglow energy flux average obtained in this work.

Even though our data is constituted by a reasonable number of UVI images, there is a lack of dayglow estimate for smaller and larger sza values, as we would expect. These extreme sza angle pixels are located in lower latitudes which means that the instrument rarely images these regions. In such sza ranges, the errors, related to the energy flux average, are
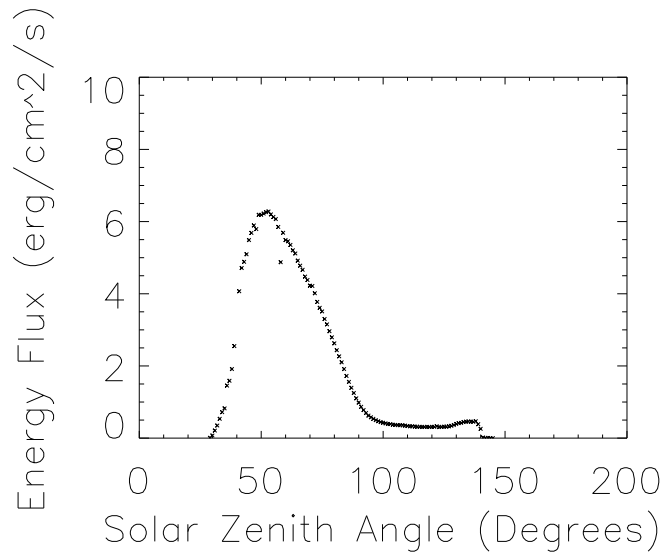
Figure 2.5 - Dayglow energy flux average calculated from 1,308 UVI images in function of solar zenith angle.

large due to the reduced number of pixels in the bins.
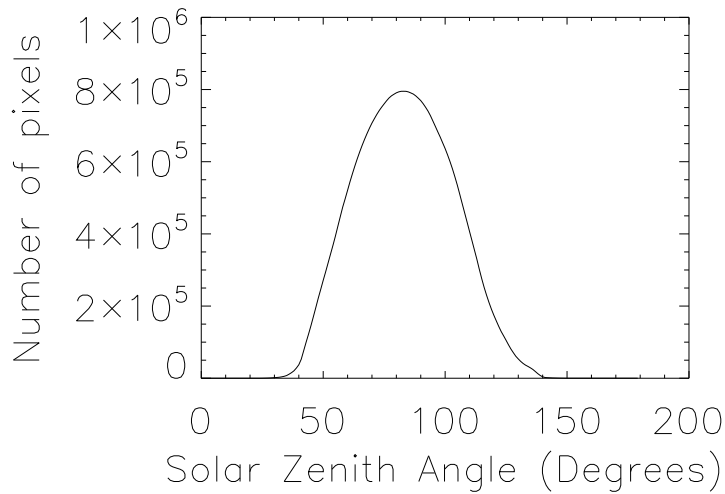
Figure 2.6 - Number of pixels contained in the bins in function of solar zenith angle.

Figure 2.6 displays the number of pixels in each sza bin. In order to minimize errors caused by a small number of pixels in some bins, only groups with number of pixels

greater than 75% of the most "populated" bin are considered here.
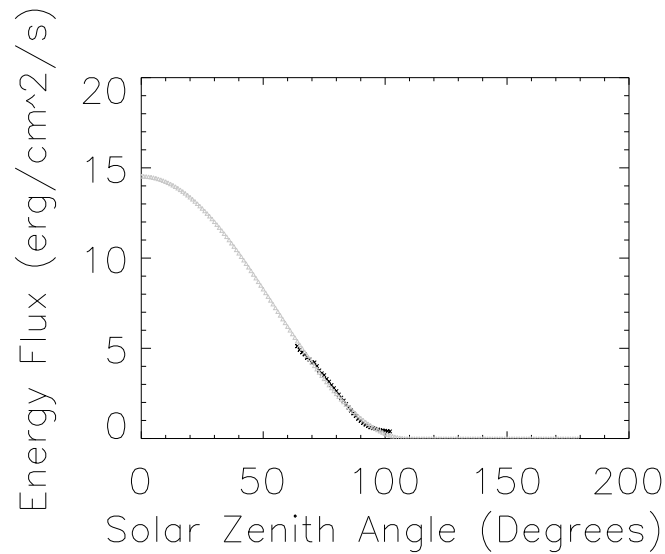
Figure 2.7 - Black color line represents dayglow average energy flux calculated for bins where the number of pixels is greater than 75% of the most "populated" bin. Gray color line corresponds to a dayglow estimate extrapolating the previous estimate with the help of an empirical function from Germany et al. (1990).

With all previous data treatment so far, the dayglow energy flux estimate (black color) is limited to a small range within sza extent (1 to 180 degrees), as we can observe in Figure 2.7. Since dayglow will be removed from UVI images afterwards, the estimate needs to cover all the sza range.

An empirical function is then used to extrapolate the dayglow energy estimate to all sza values. The empirical equation is given by (GERMANY et al., 1990):

$$dayglow = amp \times cos^2(phi \times sza), \tag{2.2}$$

where *amp* is the amplitude, *phi* and *sza* are the angles: the amplitude is an adjustment due to the solar activity variation; the *sza* angle is calculated for the pixel located on the surface of the Earth; the angle *phi* is an adjustment to sza due to the fact that the pixel source is in the atmosphere, above the surface of the Earth.

The parameters *amp* and *phi*, present in Equation 2.2, are determined for the best fit with the dayglow energy flux estimated from data, indicated by black color line in Figure

2.7. All of that was calculated with the help of a routine developed in this step, using a statistical method known as Chi Square, which simply calculates the minimum difference for each point. The final dayglow energy flux estimate is shown in Figure 2.7, as a gray color line, in function of sza.

Therefore, a dayglow energy flux estimate was obtained by a method developed in the course of this work. During all the steps here, a special care was focused on creating an accurate method in order to obtain reliable outcome.

2.3 UVI auroral energy estimate

As already mentioned previously, our intention is to estimate quantitatively particle precipitation energy through auroral emissions from UVI images. All the discussed data treatment becomes necessary since the aim is the auroral energy calculation. LOS correction as well as the dayglow energy estimate have then been performed over the UVI images. In doing this, solar contribution can be subtracted from LBH long UVI images. Figure 2.8 shows UVI LBHl images with (panel a) and without (panel b) dayglow contribution. After all, auroral energy can finally be evaluated.

The next step was to determine the best way of obtaining auroral energy. The calculation over each pixel is not so useful since its size is highly variable during the satellite orbit. Then, two manners of estimating auroral energy have been performed in this work. First, energy flux was calculated as an average for bins of $10°$ magnetic latitude and 3 hours Local Time (LT) size. Second, it was computed for the entire auroral region, from $50°$ to $90°$ magnetic latitude. Each UVI image had to be checked before the estimate in order to avoid "bad" data, which means that the image should not have lines or spots not produced by emissions.

The energy estimate from $10°$ latitude and 3 hours Local Time (LT) bins yields information about what is happening locally during an auroral event. In this step, an algorithm was developed to calculate energy flux for each bin in UVI images and to restrict the data only for bins with all the area within the UVI field of view. While spatial resolution is sacrificed by not working at the per pixel level, the uncertainties in the parameters inferred from the UVI images are reduced when averaging over the spatial bins.

For global analyses, energy is computed for the entire auroral region. UVI field of view changes significantly during the Polar's orbit, and consequently, the imaged area also varies notably. Then, energy flux in the whole field of view shows a strong dependence
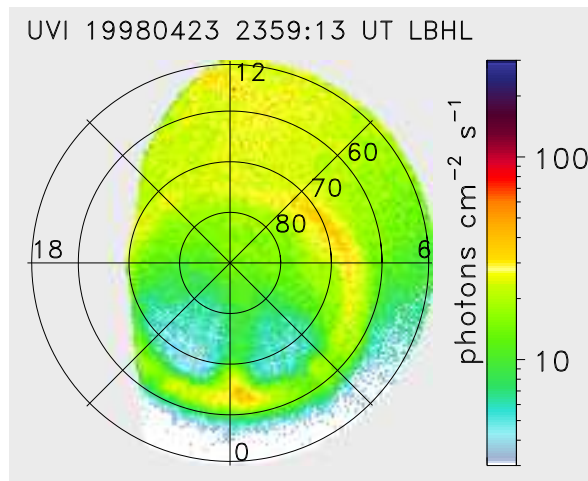
(a) LOS correction applied
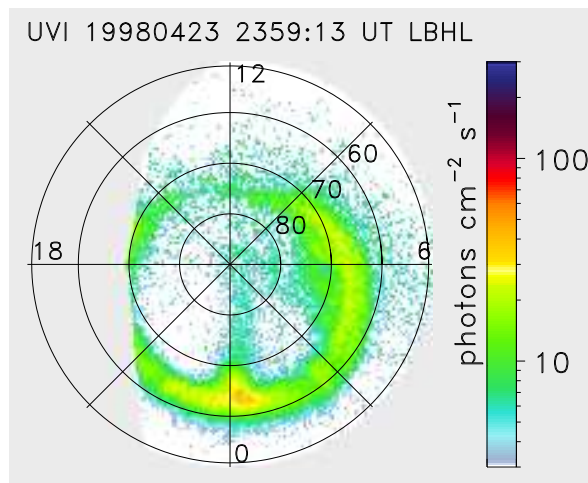
(b) LOS correction applied and dayglow removed

Figure 2.8 - LBHl UVI image of April 23, 1998 at 23:59:13 UT.

on the computational area. In order to minimize such influence, area is limited to 60% of the total auroral region considered here as 50° to 90° latitude range. This theoretical area is not reached by the UVI field of view which makes the chosen percentage number a reasonable value.

The previous global and local auroral energy calculation methods are then complementary. Auroral energy estimated for bins has no area dependence but it yields only local information. On the other hand, the total auroral region energy provides global scanning of the auroral activity although some area influence still remains. Both procedures are necessary and complementary in order to obtain more precise and accurate results.

2.4 NOAA POES Hemispheric power

Hemispheric power is an estimate of the precipitating particle power responsible for the aurora phenomena (EMERY et al., 2006). Particle precipitation is monitored during a single transit over the polar region, and afterwards, power input is estimated over all the polar region.

Instruments are flown on board the NOAA Polar-orbiting Operational Environmental Satellite (POES) which refers to a series of polar orbiting meteorological satellites first launched in November of 1978, formerly named TIROS. The spacecrafts are characterized by low-altitude (850 km) and polar (98 degrees inclination) orbit (NOAA, 2007).

The Total Energy Detector (TED) monitors energy fluxes from electrons and positive ions over the energy range between 50 and 20,000 eV. The detector watches over the energetic charged-particle environment near Earth by counting those particles which pass through the analyzers.

Hemispheric power is estimated as the total power deposited in the entire polar region through measurements obtained during a unique satellite path of about 25 minutes. Observations performed since 1978 from around 300,000 spacecraft tracks over the polar region are used to correct the estimate by taking into account how the satellite passes over a statistical auroral oval. Figure 2.9 displays power flux ($ergs/cm^2/s$) in the statistical auroral oval extrapolated from measurements during a single pass in September 30, 2010, as an example. Black line identifies the spacecraft track and the estimated power for this pattern is 2.3 GW.

The precipitation power estimated by this method is directly derived from observations and becomes a comparison tool in relation to the UVI evaluation method. Although UVI has a much better resolution, it is still worth to examine both method results.
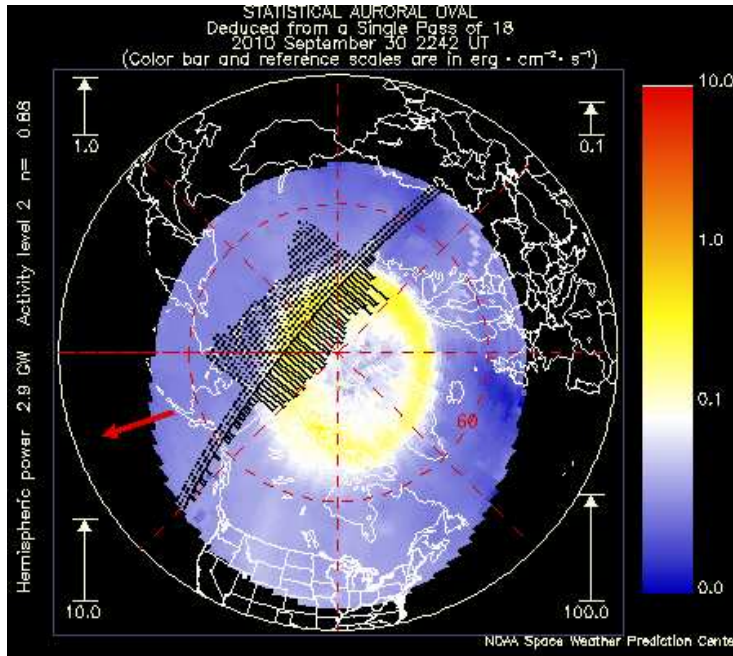
Figure 2.9 - Hemispheric power estimated in a statistical auroral oval in the northern hemisphere obtained by NOAA-POES. Red arrow points toward the noon meridian.

2.5   Events selection

Magnetic storms were selected for the year of 1998. From a total of six events, three of them have long recovery phase duration, more than two days, and are named LRP. The three left events correspond to magnetic storms containing short interval of recovery phase, less than two days, and are so-called SRP. This time limit (two days) was obtained from HILDCAA definition (TSURUTANI; GONZALEZ, 1987).

The selected events shown below are described in details in Chapter 3:

a) Event 1 - SRP - January 6 to 8, 1998;

b) Event 2 - SRP - June 14 to 15, 1998;

c) Event 3 - SRP - June 25 to 27, 1998;

d) Event 4 - LRP- April 23 to 30, 1998;

e) Event 5 - LRP - July 22 to 26, 1998;

f) Event 6 - LRP - August 26 to September 3rd, 1998.

3 EVENTS CHARACTERISTICS

In this work, the events were selected according to the recovery phase duration within magnetic storms. Longtime recovering during storms are associated with HILDCAA phenomena occurrence (TSURUTANI; GONZALEZ, 1987). The six selected events are then primarily organized in two groups. One gathers magnetic storms which are characterized by short recovery phases and named SRP events. The other one assembles events presenting long recovery phase feature, wich are labeled by LRP events. The characteristics of the events divided in SRP and LRP are displayed in table 3.1.

Table 3.1 - *Characteristics of the events*

Event	Date	Recovery phase	Dst minimum	Activity level
SRP events				
1	January 6-8, 1998	1.25 days	-77 nT	moderate
2	June 14-15, 1998	1.08 days	-55 nT	moderate
3	June 25-27, 1998	1.50 days	-101 nT	moderate/intense
LRP events				
4	April 23-30, 1998	6.13 days	-69 nT	moderate
5	July 22-29, 1998	5.00 days	-48 nT	weak
6	Agust 26-September 3rd, 1998	7.17 days	-158 nT	intense

All the events are selected within 1998, since the dayglow is estimated only for the same year. Events 4 and 5 are also classified as HILDCAAs by Guarnieri (2006), since they satisfy all the criteria imposed by Tsurutani e Gonzalez (1987).

Figures 3.1 to 3.6 display the low (Dst, SYM-H and ASY-H) and high latitude (AE, AL and AU) geomagnetic indices for each event. Dst is an hourly measurement of the magnetic field horizontal component variation at low latitudes and is an indicator of the ring current intensity (SUGIURA, 1964). SYM-H represents the magnitude of the uniform field parallel to the dipole axis generated by the symmetric ring current. ASY-H is obtained by subtracting the symmetric component from each disturbance field (IYEMORI, 1990). AE index is also computed from variations in the magnetic field horizontal component measured by stations located in the Northern auroral zone (KAMIDE; ROSTOKER, 2004). Actually, AE index is defined by the difference between AU and AL indices which, in turn, are associated to the westward and eastward auroral electrojets (ROSTOKER, 1972; DAVIS; SUGIURA, 1966). These geomagnetic indices are available on WDC (World Data

Center) for Geomagnetism, at Kyoto University (KYOTO, 2010).

Event 1 occurs within the time interval of January, 6 to 8, 1998. Figure 3.1 displays AE, AL and AU indices in the first column, and Dst, SYM-H and ASY-H in the second column. Three lines seen in Figure indicate the main and recovery phase duration. According to Dst index, the main phase of a magnetic storm starts with the maximum Dst value, at 6.63 doy (days of year in UT) (6, 15:07:12 UT), and ends at the minimum Dst time value, which is 7.21 doy (7, 05:02:24 UT), resulting in a duration interval of 0.58 day. Recovery phase covers the interval between minimum and maximum Dst values, extending from 7.21 to 8.46 doy (8, 11:02:24 UT). This phase lasts 1.25 days. Such event is labeled as SRP type due to its recovery phase duration time.

Figure 3.1 - Geomagnetic indices for the event occurred on January 6-8, 1998, SRP (Event 1). AE, AL and AU indices are displayed in the first column. Dst, SYM-H and ASY-H are located in the second column.

Dst reaches the minimum at -77 nT which indicates the beginning of the recovery phase. According to Gonzalez et al. (1994) definition, this magnetic storm is considered moderate. Dst profile presents a smooth behavior, although fluctuations can be observed in

32

SYM-H and ASY-H indices. As such indices present finer resolution than Dst, that indicates the presence of fluctuations of the order SYM-H and ASY-H data resolution. AE index shows an initial peak at about 1,150 nT which lasts about 3.5 hours. Then, the profile follows to high values until Dst minimum and starts to decrease continuously up to 7.75 doy (7, 18:00:00 UT). AE index is already within calm conditions while Dst is still recovering to pre-storm values.

Figure 3.2 - Geomagnetic indices for the event occurred on June 14-16, 1998, SRP (Event 2). AE, AL and AU indices are displayed in the first column. Dst, SYM-H and ASY-H are located in the second column.

Event 2 is also classified as SRP (Figure 3.2). Magnetic storm time interval corresponds to June 14-16, 1998. Main phase starts at 165.17 (165, 04:04:48 UT) and ends at 165.46 doy (165, 11:02:24 UT), which gives a duration interval of 0.29 days. Recovery phase covers a time period of 1.08 days, extending from 165.46 to 166.54 doy (166, 12:57:36 UT).

This magnetic storm is classified as moderate since minimum Dst value is -55 nT. AE peaks at 1000 nT at the beginning of main phase. AE values start decreasing towards

main-recovery phase transition where it turns to grow. At about 165.6 doy (165, 14:24:00), it diminishes rapidly to lower values, less than 200 nT. AE augments again after 166.2 doy, simultaneously with some decays in the Dst index.
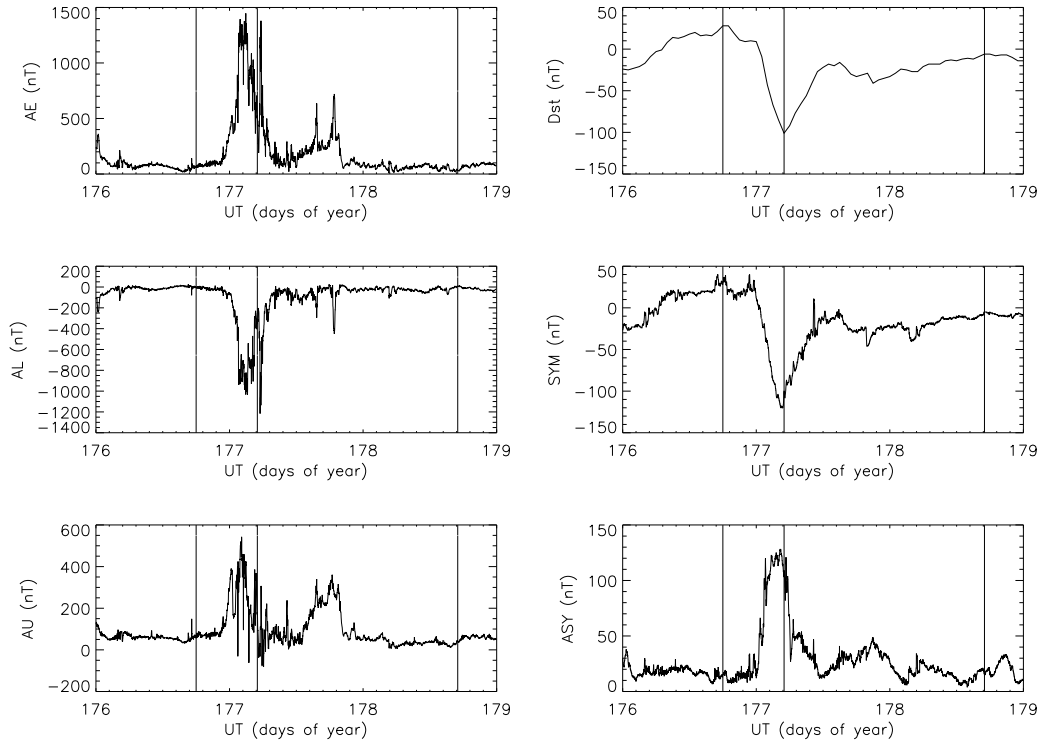
Figure 3.3 - Geomagnetic indices for the event occurred on June 25-27, 1998, SRP (Event 3). AE, AL and AU indices are displayed in the first column. Dst, SYM-H and ASY-H are located in the second column.

Event 3 is a SRP phenomenon occurring within June 25-27,1998 (Figure 3.3). Magnetic storm main phase lasts 0.46 day, from 176.75 (176, 18:00:00 UT) to 177.21 doy (177, 05:02:24 UT). Recovery phase time interval takes 1.5 days, extending from 177.21 to 178.71 doy (178, 17:02:24 UT).

Dst reaches the minimum at -101 nT which falls in a transition boundary between moderate and intense magnetic storms. AE peaks at about 1,400 nT with some delay comparing to the main phase start but following the abrupt Dst behavior.

Differently from previous cases, Event 4 is labeled as LRP and occurs within April 23-30, 1998 (Figure 3.4). Main phase time interval is 0.5 day and extends from 113.83 to
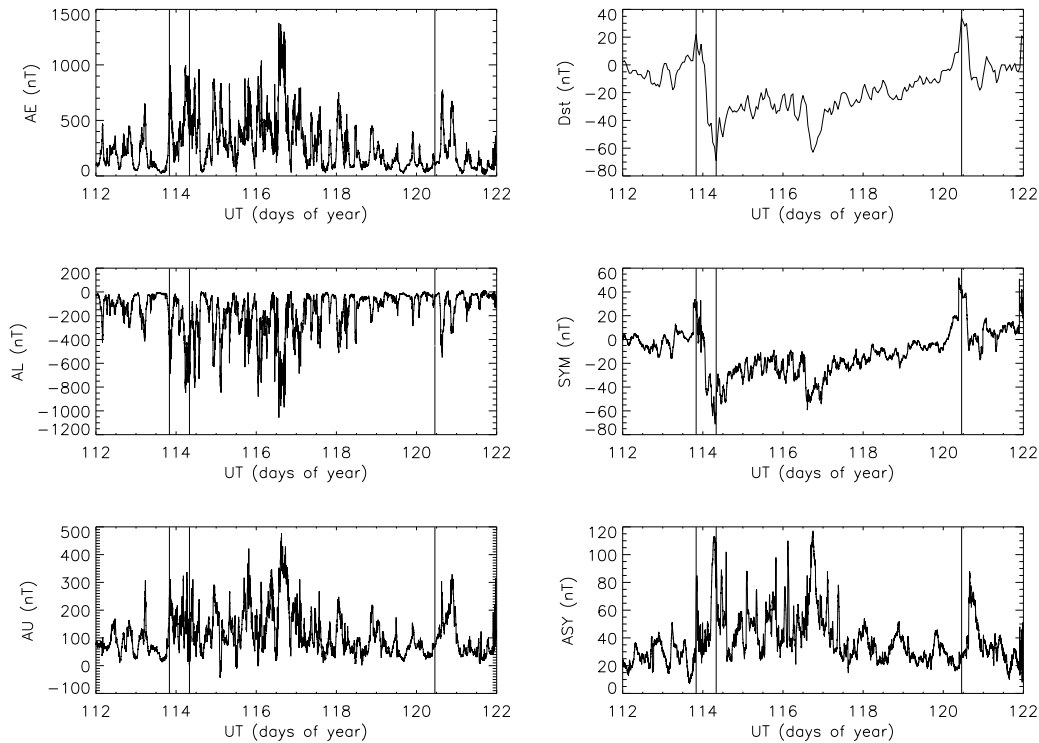
Figure 3.4 - Geomagnetic indices for the event occurred on April 23-30, 1998, LRP (Event 4). AE, AL and AU indices are displayed in the first column. Dst, SYM-H and ASY-H are located in the second column.

114.33 doy (113, 19:55:12 to 114, 07:55:12 UT) while recovery phase takes 6.13 days, from 114.33 to 120.46 doy (114, 07:55:12 to 120,11:02:24 UT).

In this case, Dst index peaks at -69 nT which brings this magnetic storm to moderate status. Both AE and Dst present a much more fluctuating profile in LRP than in SRP events. AE peaks around 1,400 nT which is coincident with an abrupt decay in the Dst index. During all the recovery phase, AE index exhibits high intensity and variability. Quiet values are reached at the end of the phase.

Event 5 occurs on July, 22 to 29, and it is also classified as LRP (Figure 3.5). Main phase lasts 1 day, covering the range of 203.67 (203, 16:04:48 UT) to 204.67 doy (204, 16:04:48 UT). Recovery phase comprehends 204.67 to 209.67 doy (209, 16:04:48 UT) time interval which gives a 5 day duration.

According to geomagnetic indices in Figure 3.5, Dst peaks at -48 nT and the magnetic storm is classified as weak. AE index is observed as intense exhibiting a peak at 1,400 nT
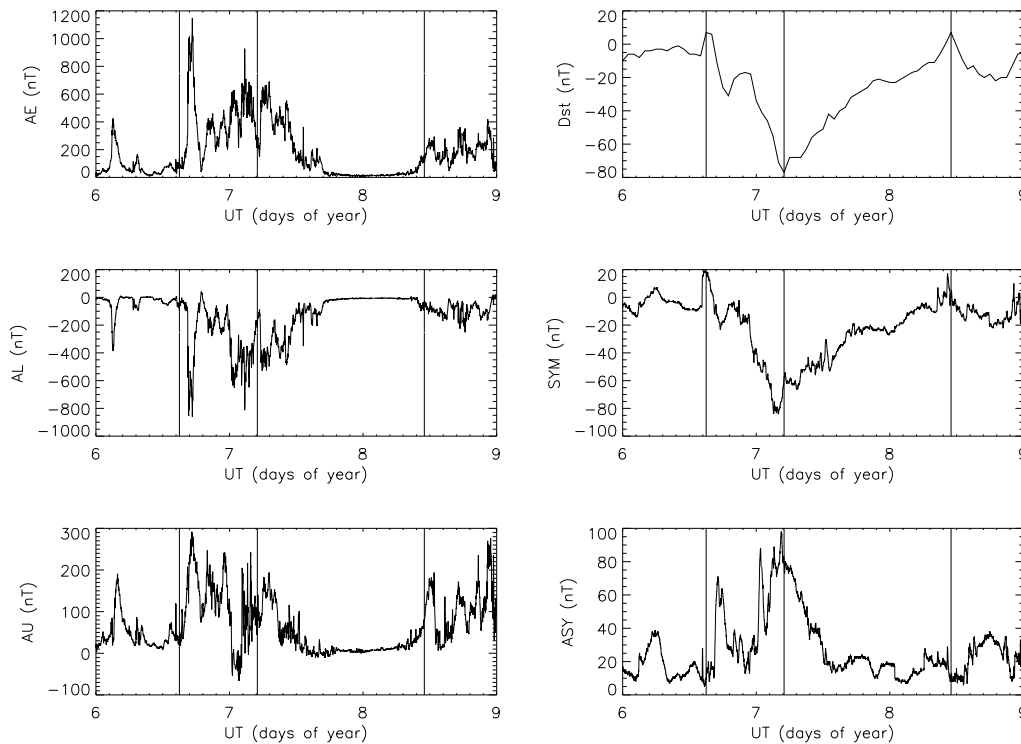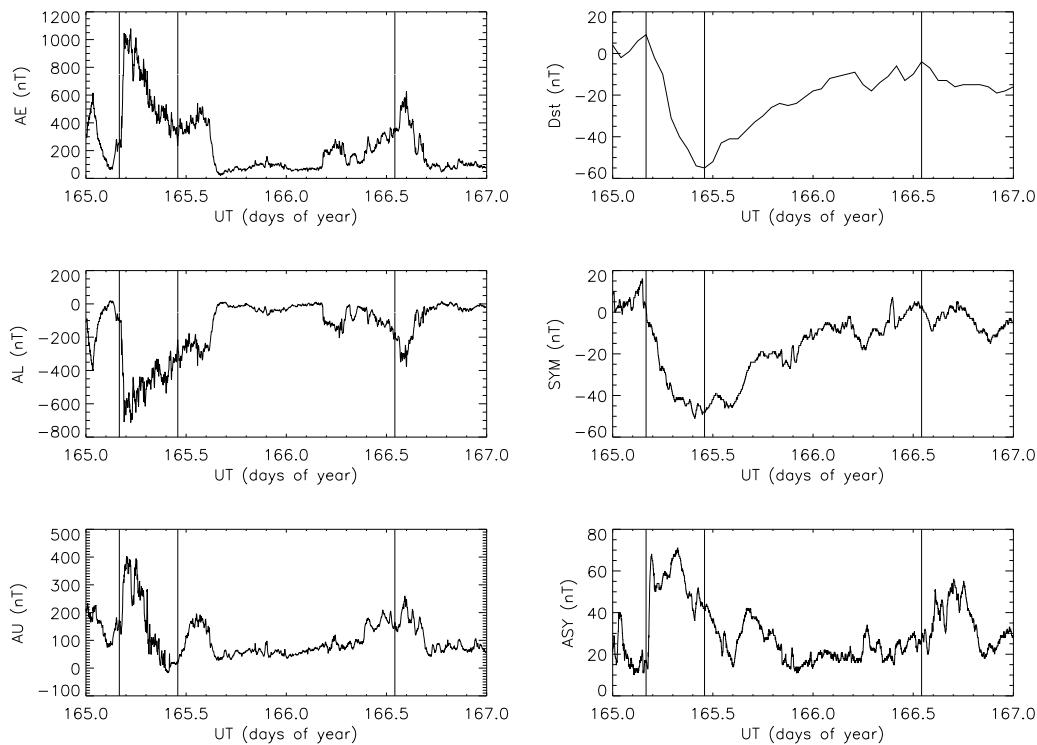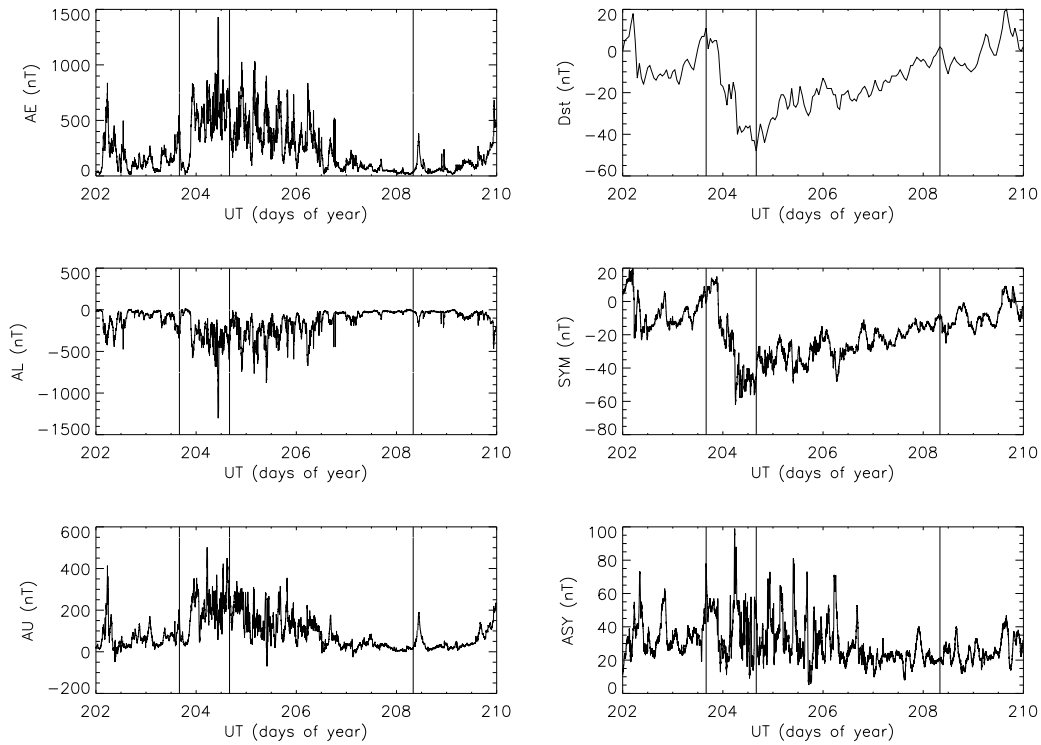
Figure 3.5 - Geomagnetic indices for the event occurred on July 22-29, 1998, LRP (Event 5). AE, AL and AU indices are displayed in the first column. Dst, SYM-H and ASY-H are located in the second column.

and falls to low values for more than one day interval, before the end of the storm.

Finally, Event 6, also a LRP storm type, extends from August 26 to September 3rd, 1998 (Figure 3.6). Main phase lasts 1.04 days, within the interval of 238.38 (238, 09:07:12 UT) to 239.42 doy (239, 10:04:48 UT), while recovery phase takes 7.17 days, from 239.42 doy (239, 10:04:48 UT) to 246.58 (246, 13:55:12 UT).

Dst reaches the minimum at -158 nT. Hence, this magnetic storm is within intense definition. AE peaks at about 1,800 nT and present the same fluctuating behavior as previous LRP events.

A sequence of UVI images with dayglow removed and LOS correction applied for Events 2 and 4 are presented in Figures 3.7 and 3.8 as examples of SRP and LRP phenomena, respectively. UVI images permit to follow the spatial evolution of the auroral activity, in this case, during magnetic storms.

36
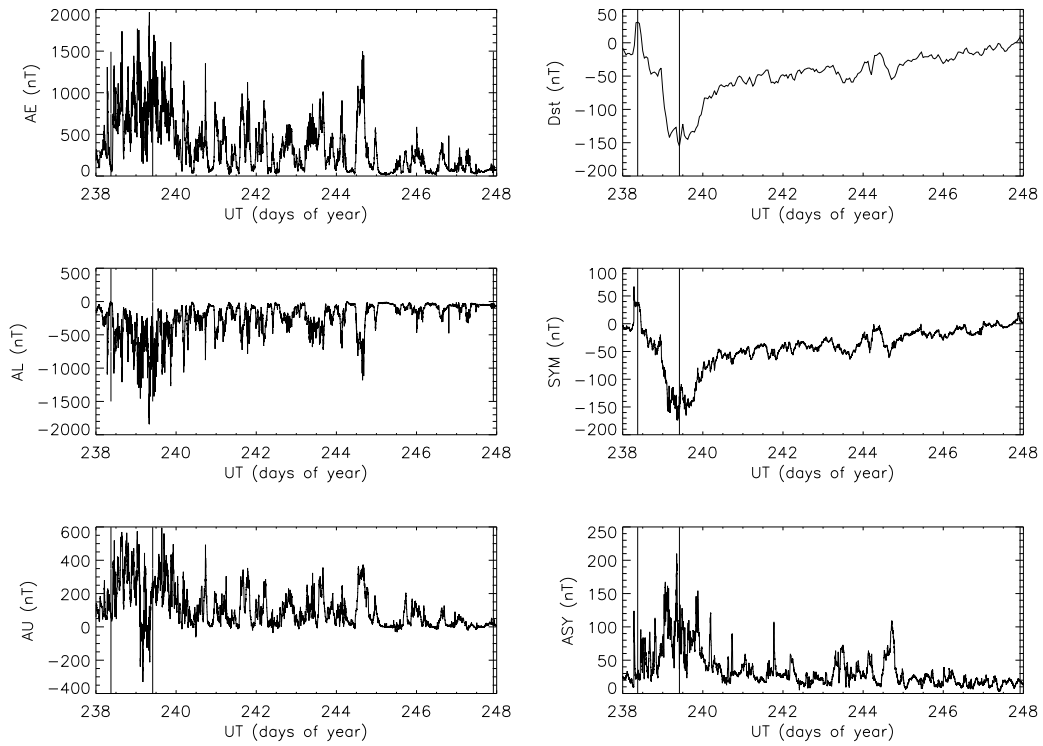
Figure 3.6 - Geomagnetic indices for the event occurred on August 26 to September 3rd, 1998, LRP (Event 6). AE, AL and AU indices are displayed in the first column. Dst, SYM and ASY are located in the second column.

(a) Main phase   (b) Main phase

(c) Recovery phase   (d) Recovery phase

(e) Recovery phase   (f) Recovery phase

(g) Recovery phase   (h) Recovery phase
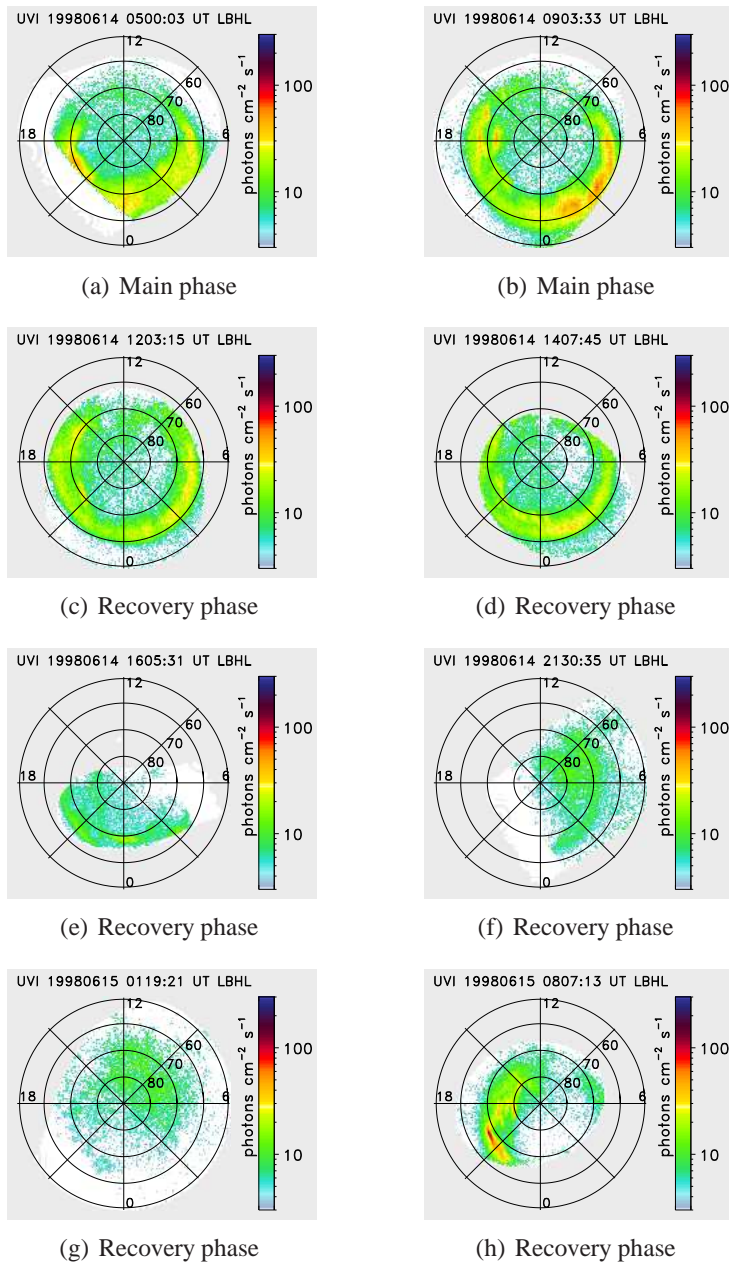
Figure 3.7 - UVI images during magnetic storm. June 14-15, 1998, SRP (Event 2).
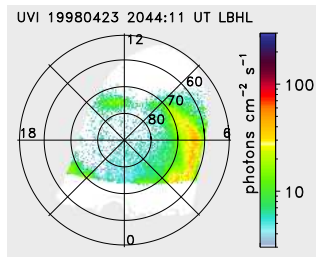
(a) Main phase
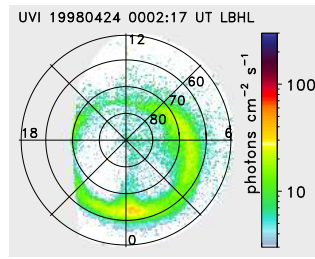
(b) Main phase
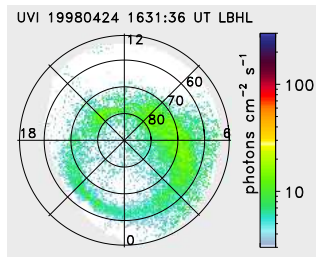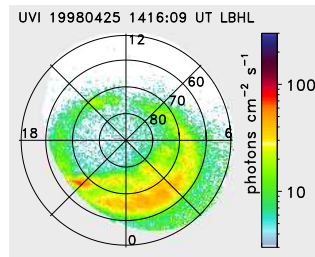
(c) Recovery phase
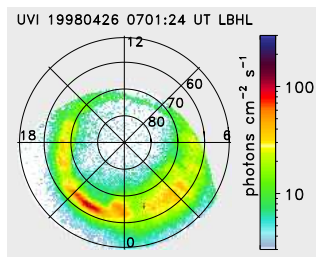
(d) Recovery phase
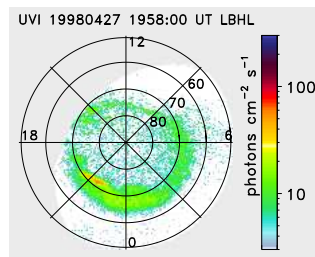
(e) Recovery phase
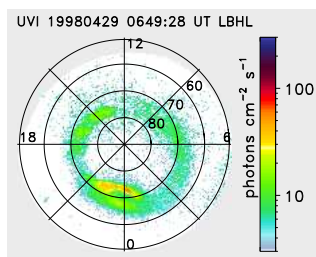
(f) Recovery phase
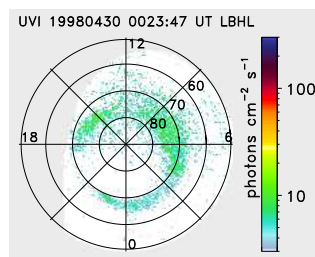
(g) Recovery phase

(h) Recovery phase

Figure 3.8 - UVI images during magnetic storm. April 23-30, 1998, LRP (Event 4).

4 RESULTS: AURORAL ENERGY INPUT

Auroral energy input in the polar region can be derived from UVI images by applying correction methods. Besides all the satellite position and calibration improvements, dayglow estimate method is an important and essential tool to obtain auroral energy. Such procedure allows us to estimate the dayglow energy and remove it from the UVI images resulting in an auroral energy evaluation. Hence, auroral energy can be computed for phenomena of interest in order to obtain clues about unknown physical processes and mechanisms.

Electron precipitating energy is obtained from UVI images during the selected magnetic storms. Global and local energy estimates are used to evaluate the energy input intensity and the differences between SRP and LRP events. These results are shown in Section 4.1. An important task is to investigate how polar precipitation affects the equatorial and auroral current systems. Section 4.2 brings this discussion.

Besides UVI energy estimate method, there are other manners of evaluating auroral precipitation energy. Hemispheric power is estimated from observations of particles influx by NOAA POES extrapolated for the entire auroral region by statistical models. Auroral energy deposition can also be calculated from geomagnetic indices such as AL and AE, which reasonably reflect changes in the precipitation patterns. Linear and nonlinear empirical relations are used to obtain electron precipitation energy. All these methods are discussed and compared in Section 4.3.

4.1 UVI Auroral Energy input estimate

Auroral observations can provide important information on the dynamics of solar wind-magnetospheric-ionospheric interactions. This is possible due to the fact that aurora brightness can be related to the energy input into the atmosphere.

Auroral emission intensity within LBH range is directly proportional to the energy flux injected by particle precipitation into the atmosphere. The LBH emission is attenuated in the atmosphere since shorter LBH (LBHs) wavelengths still lie in the range of the O_2 absorption. Hence, LBH long (LBHl) emissions are more indicated to compute energy input in the auroral region. Even taking care about the ideal wavelength emission, there is still solar contribution (dayglow) present in the UVI images. For this reason, a dayglow estimate method was developed in this work. This tool made possible the dayglow energy removal from each UVI image of the Northern hemisphere. Therefore, auroral

energy could be calculated in UVI images through LBH long emissions with no solar contribution.

Figures 4.1 and 4.2 display energy flux for SRP and LRP events, respectively. Vertical lines seen in Figures indicate main and recovery phase duration. Energy flux is calculated over the area within the UVI field of view corresponding to each time (Universal Time - UT). As already mentioned, the Polar spacecraft takes about 18 hours to complete a 9.0 by 1.8 R_E orbit. In this case, auroral oval is covered globally only for distances greater than about 6 R_E, which means roughly nine hours, assuming that the equatorward auroral oval boundary is near 60° ML (magnetic latitude). In order to minimize area variation influence on the energy estimate, data corresponding to auroral area values greater than 60% of the total auroral region is not considered. Total area is assumed to cover from 50 to 90° ML. Lack of data is represented by blanks on the plot.

Energy flux computed from the available data shows that LRP events are more energetic than SRP. Energy flux peaks at around 2 $ergs/cm^2/s$ in Figure 4.1 and about 3 $ergs/cm^2/s$ in Figure 4.2. Moreover, LRP energy flux is found to be highly variable when compared to SRP phenomena. Particle precipitation energy seems to peak around Dst minimum during all the cases where available data allow an analysis.

Even though auroral region area accounted for the energy flux estimate may not change significantly, some trace of the area variability can be within the energy evaluation. For this reason, energy flux was computed for each invariable area of 10° ML and 3h LT (Local time) extending from 50° to 90° ML. The energy estimated in the sectors was based in the restricted data used previously for the total energy calculation which auroral area values should be greater than 60% of the total theoretical auroral region. Figures 4.3 to 4.5 and Figures 4.6 to 4.8 show energy flux computed for each sector (10° ML and 3h LT area) during June 14-16, 1998 (Event 2), a SRP event, and April 23-30, 1998 (Event 4), a LRP phenomenon, respectively. There is a large lack of data for 50° to 60° ML range and it is not displayed here. Sector energy flux for the other events are shown in Appendix A.

The energy flux variability can still be observed in Figures 4.3 to 4.5 and Figures 4.6 to 4.8, even though the area used in the calculation is constant. LRP events exhibit higher variable energy flux when compared to SRP events, which confirms our previous findings.
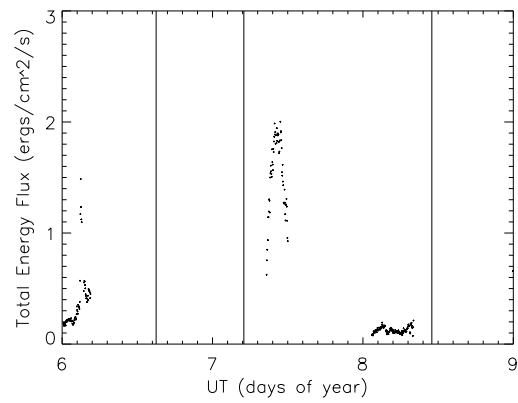
(a) January 6-8, 1998, SRP (Event 1).
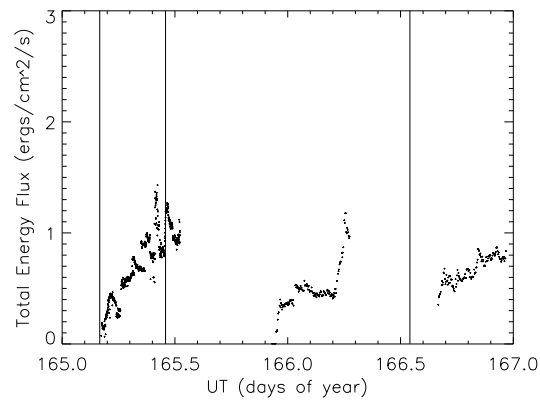
(b) June 14-16, 1998, SRP (Event 2).
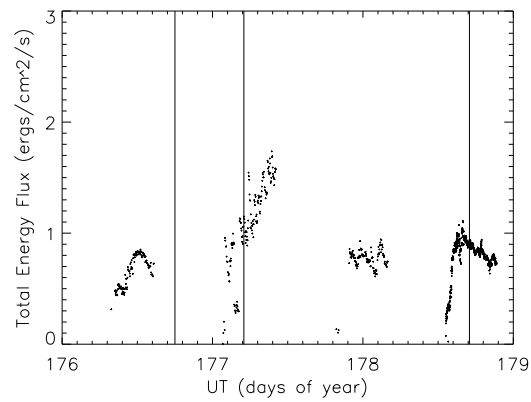
(c) June 25-27, 1998, SRP (Event 3).

Figure 4.1 - Energy flux computed over each UVI image for all the polar region from 50° to 90° during SRP events. Vertical lines indicate main and recovery phase duration.
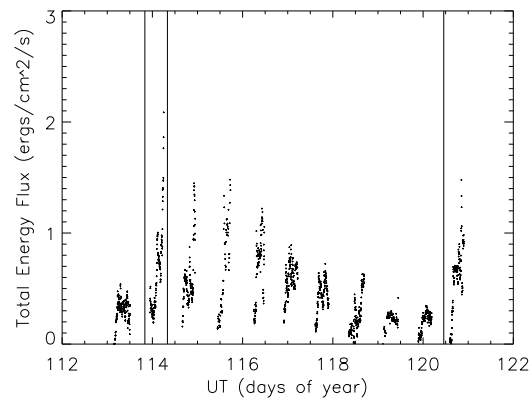
(a) April 23-30, 1998, LRP (Event 2).
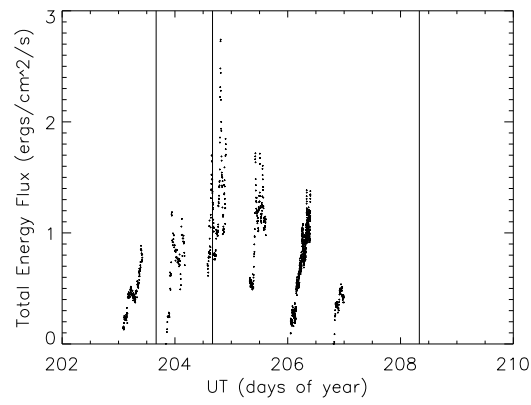
(b) July 22-29, 1998, LRP (Event 5).
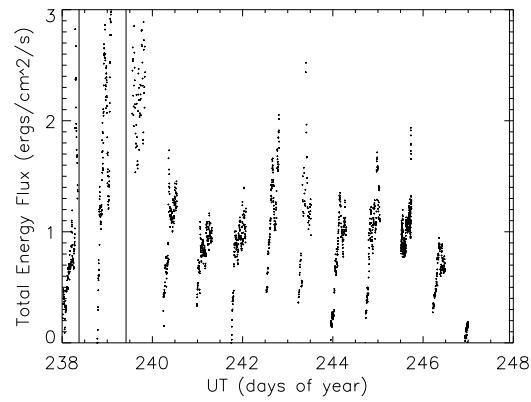
(c) August 26-September 3rd, 1998, LRP (Event 6).

Figure 4.2 - Energy flux computed over each UVI image for all the polar region from 50° to 90° during LRP events. Vertical lines indicate main and recovery phase duration.
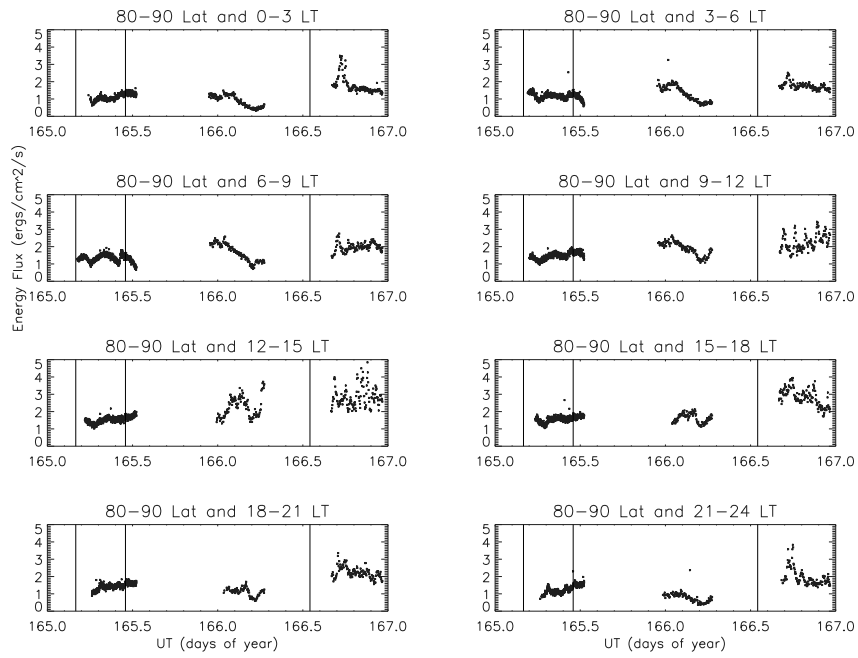
Figure 4.3 - Energy flux computed from 80 to 90° magnetic latitude for each 3h LT. June 14-16, 1998, SRP (Event 2).
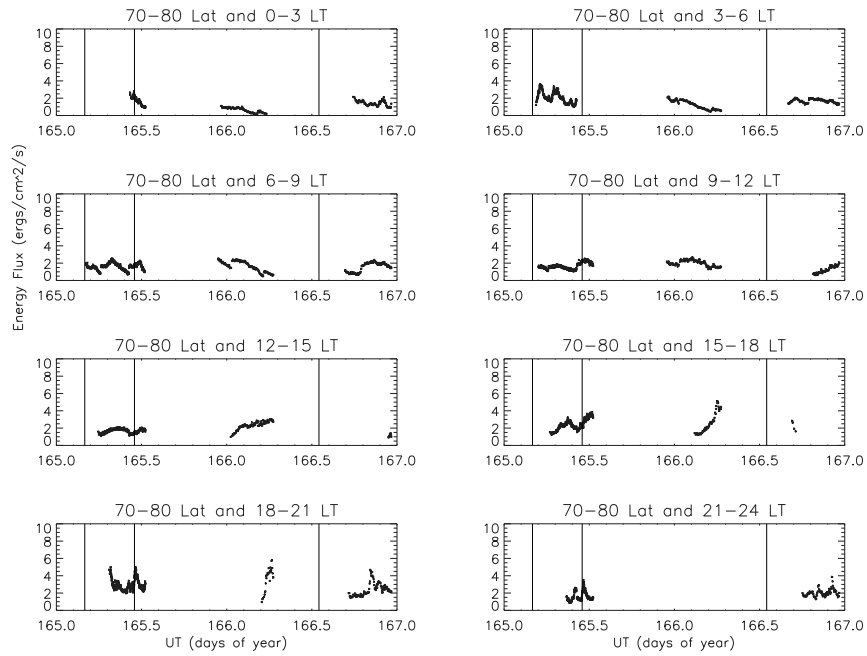
Figure 4.4 - Energy flux computed from 70 to 80° magnetic latitude for each 3h LT. June 14-16, 1998, SRP (Event 2).
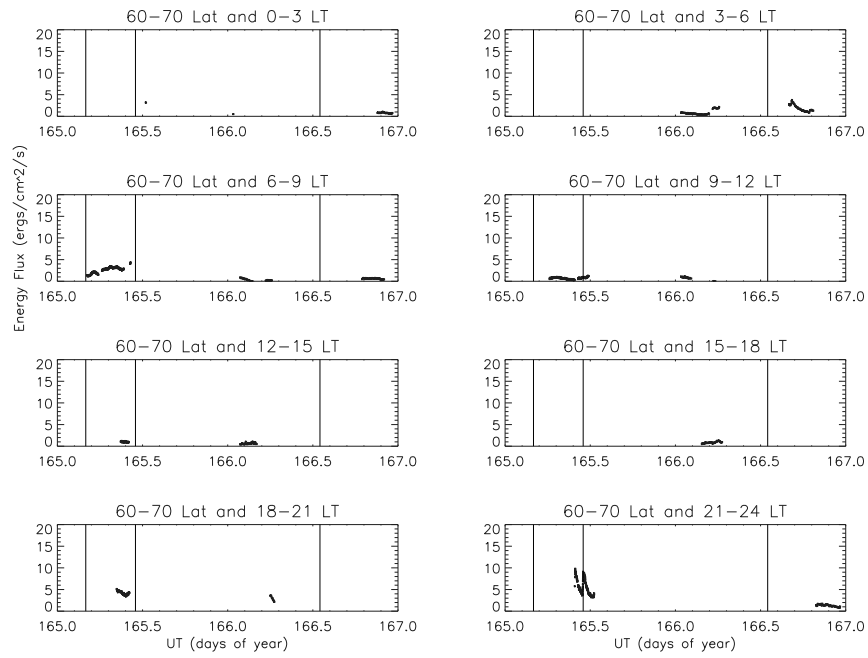
Figure 4.5 - Energy flux computed from 60 to 70° magnetic latitude for each 3h LT. June 14-16, 1998, SRP (Event 2).
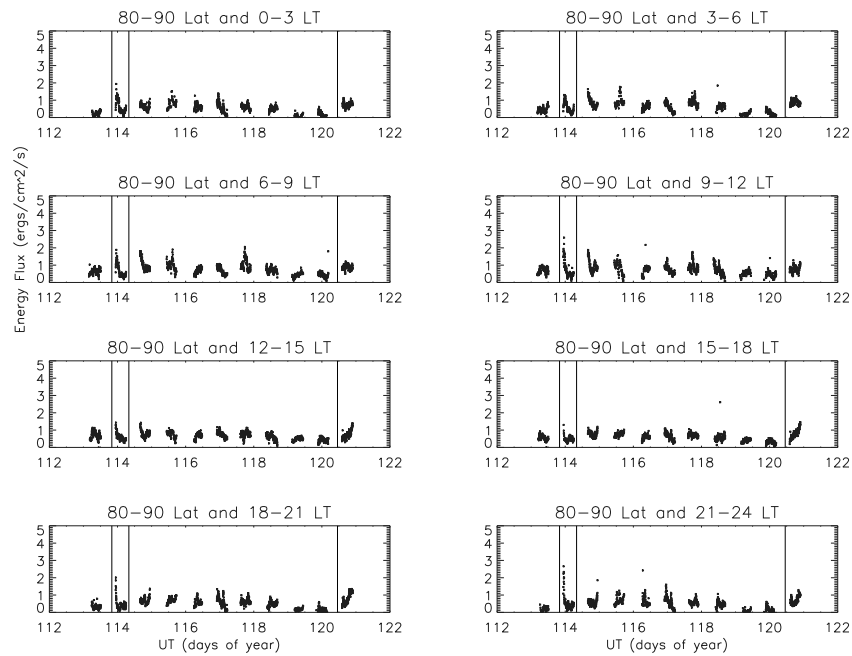
Figure 4.6 - Energy flux computed from 80 to 90° magnetic latitude for each 3h LT. April 23-30, 1998, LRP (Event 4).
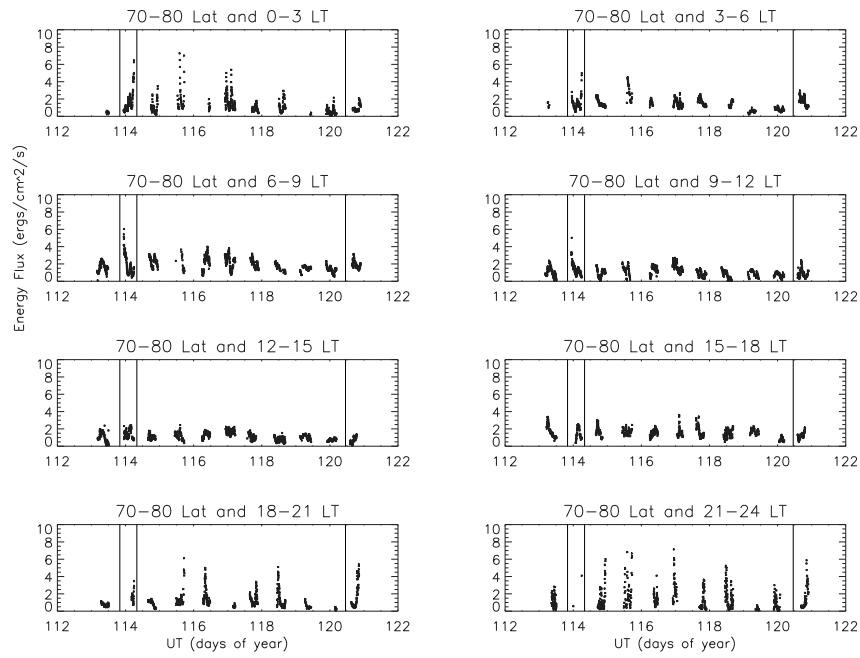
Figure 4.7 - Energy flux computed from 70 to 80° magnetic latitude for each 3h LT. April 23-30, 1998, LRP (Event 4).
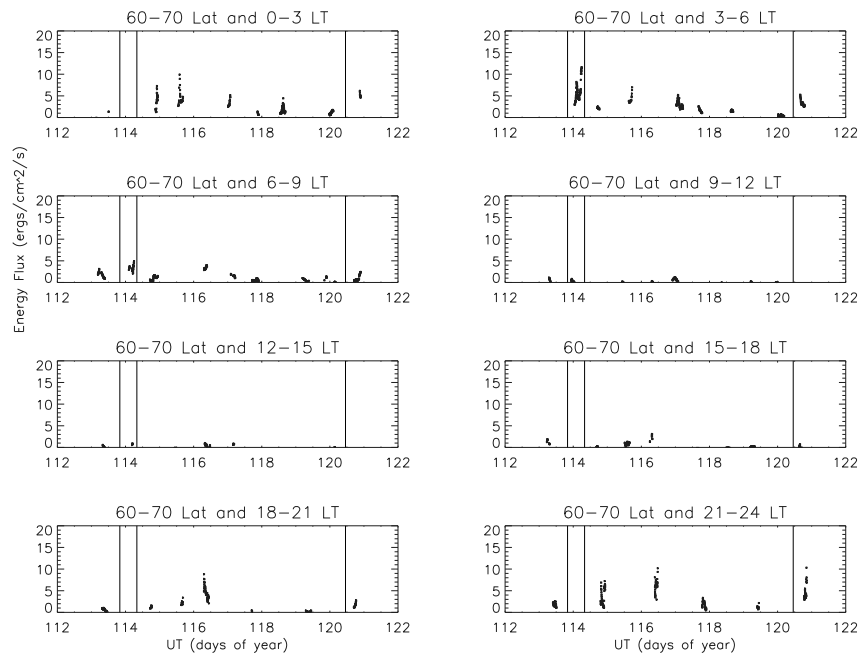
Figure 4.8 - Energy flux computed from 60 to 70° magnetic latitude for each 3h LT. April 23-30, 1998, LRP (Event 4).

The midnight region is an active region in the auroral zone. Figures 4.9 and 4.10 show the energy flux computed for all the polar region (black) and for a region around midnight (red) for SRP and LRP phenomena, respectively. The midnight area was considered to extend from 21 to 3 LT and from $50°$ to $90°$ ML. Usually, the midnight energy flux presents similar behavior to that computed for the total auroral area. Again, energy flux presents more variability for LRP than SRP events. The midnight area is kept constant on the energy flux computation which garantees that the energy flux variability is not due to the area influence.
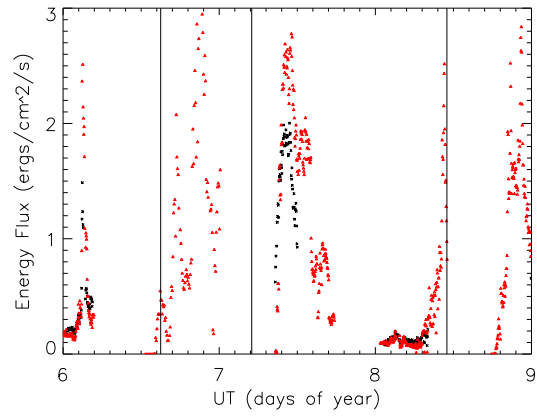
(a) Event 1
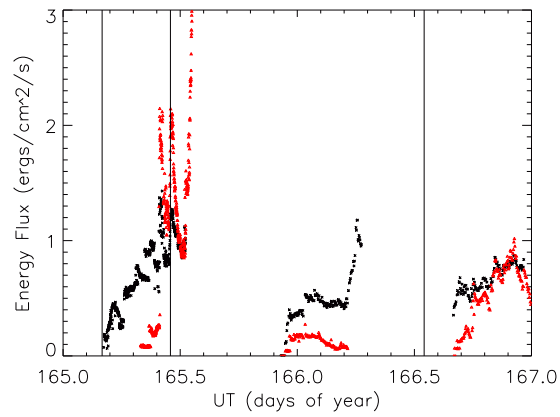
(b) Event 2
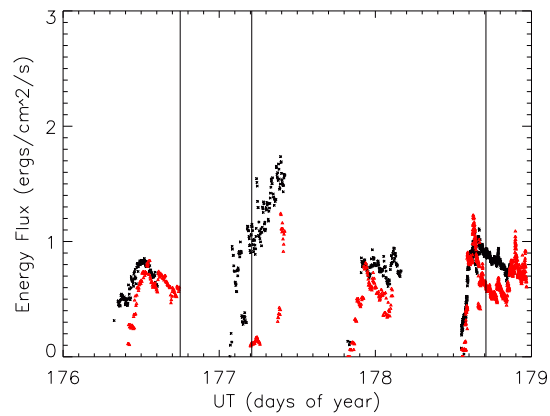
(c) Event 3

Figure 4.9 - Black x's indicate the energy flux computed over all the polar region. Red triangles represent energy flux computed over the region close do midnight (from 21 to 3 LT and from 50° to 90° ML). SRP events.

49
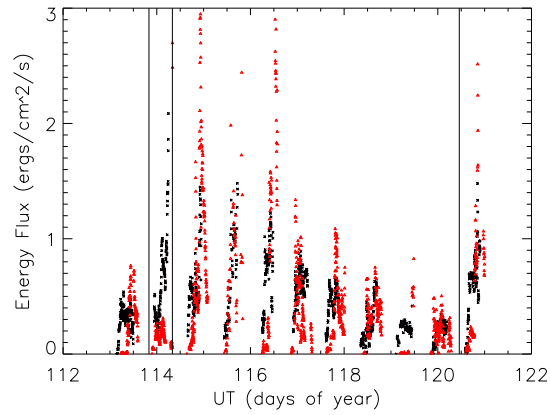
(a) Event 4
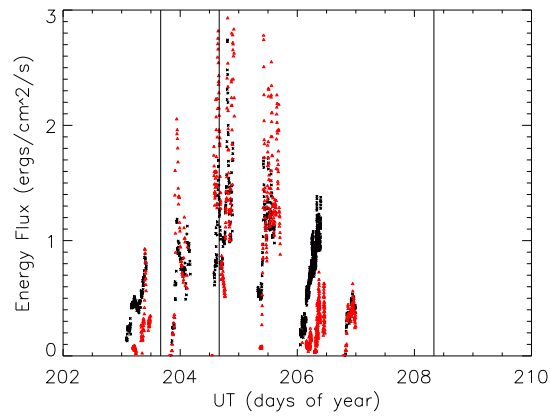
(b) Event 5
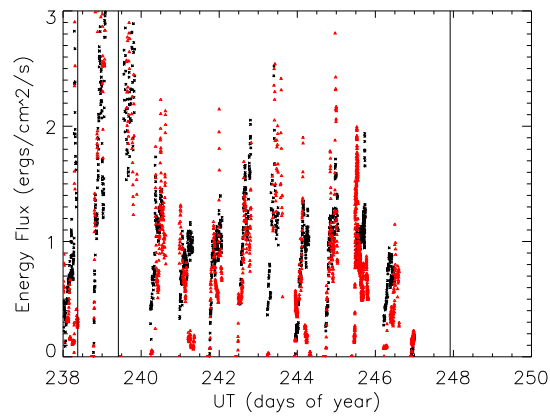
(c) Event 6

Figure 4.10 - Black x's indicate the energy flux computed over all the polar region. Red triangles represent energy flux computed over the region close do midnight (from 21 to 3 LT and from 50° to 90° ML). LRP events.

Besides studying the energy flux behavior with time, it is also worth looking at the intensities during the phases of a magnetic storm. Figures 4.11 and 4.12 display energy flux versus LT sector number for each $10°$ ML during main and recovery phase for a SRP (Event 2) and LRP (Event 4) magnetic storm, respectively. The data used here also corresponds to auroral area values greater than 60% of the total theoretical auroral region. Results for the other events are presented in the Appendix B. Sector number refers to 3h LT intervals starting at midnight (0 LT). Then, sectors 1, 2, 7 and 8 are located in the nightside while 3 to 6 sector numbers refer to the dayside. Although we present here only the results for Events 2 and 4, all the events are described below.

Event 1 (SRP) presents higher values at sectors 7 and 8, peaking at about 3 $ergs/cm^2/s$, for $80°$ to $90°$ ML range for all LT during recovery phase. There is no data for main phase in this event. High activity takes place in the $70°$ to $80°$ ML range from 15 to 24 LT during recovery time, with energy flux peaking at 10.0 $ergs/cm^2/s$. High nightside activity for $60°$ to $70°$ ML, reaching 16 $ergs/cm^2/s$ close to midnight, can be observed.

Event 2 (SRP) also exhibits low values peaking at 2.5 $ergs/cm^2/s$, for $80°$ to $90°$ ML during main phase (Figure 4.11). It is noticeable a localized high activity reaching 6.0 $ergs/cm^2/s$, from 15 to 24 LT in the $70°$ to $80°$ region, during recovery phase. In the $60°$ to $70°$ ML interval, energy flux is high in the nightside, reaching 10 $ergs/cm^2/s$ for main phase and 9.3 $ergs/cm^2/s$ during recovery time.

Event 3 (SRP) shows low values (less than 2.3 $ergs/cm^2/s$) for $80°$ to $90°$ ML during main phase. High activity is seen near dusk during recovery stage in this latitude range, peaking at 5.0 $ergs/cm^2/s$. High energy flux intensities are found within recovery time from 15 to 24 LT for $70°$ to $80°$ (peaks at 9 $ergs/cm^2/s$). Energy flux reaches 9 $ergs/cm^2/s$ in the $60°$ to $70°$ ML range during recovery period.

Event 4 (LRP) presents energy flux values less than 2.5 $ergs/cm^2/s$ for the whole storm in the $80°$ to $90°$ ML range. In relation to $70°$ untill $80°$ ML region, higher auroral activity is concentrated from 0 to 9 LT during main stage (peaking at 6.5 $ergs/cm^2/s$). In the recovery time, high values are found in the nightside (reaching 8 $ergs/cm^2/s$), and the energy flux behavior shows a symmetric feature in the plot. The $60°$ to $70°$ region during recovery phase also present such symmetry (higher energy flux values peaking at 11.5 $ergs/cm^2/s$ in the nightside and lower in the dayside). This characteristic indicates that the auroral energy flux intensities are distributed over all the polar region, despite of the dayside magnitudes are smaller.

51

Event 5 (LRP) shows energy flux peaking at about 3 $ergs/cm^2/s$ and 5 $ergs/cm^2/s$ in the 80° to 90° ML interval during main and recovery phases, respectively. Within 70° to 80° ML region, energy flux reaches 7.5 $ergs/cm^2/s$ and 11 $ergs/cm^2/s$ in the main and recovery stages. Higher activity is also observed in the nightside in this latitude range.

Event 6 (LRP) present energy flux peaking around 5 $ergs/cm^2/s$ within 80° to 90° ML region during the magnetic storm. Energy flux is observed more intense in the nightside, peaking at 12.5 $ergs/cm^2/s$ during main phase and at 11 $ergs/cm^2/s$) in the recovery process, in the range of 70° to 80° ML. Energy flux peaks at 11 $ergs/cm^2/s$ and 12 $ergs/cm^2/s$ during main and recovery times from 60° to 70° ML. The activity is observed mostly in the nightside.

For all the events, it is possible to observe that sector numbers 6 to 8 (15 to 24 LT) near dusk present larger energy flux values mostly in the 70° to 80° ML range. This is an indicator that the duskside is a very active region for magnetic storms in general. LRP seems to be a more energetic process though such difference does not look considerable. Otherwise, a large quantity of energy can be deposited during a LRP magnetic storm since it is a longtime phenomenon.
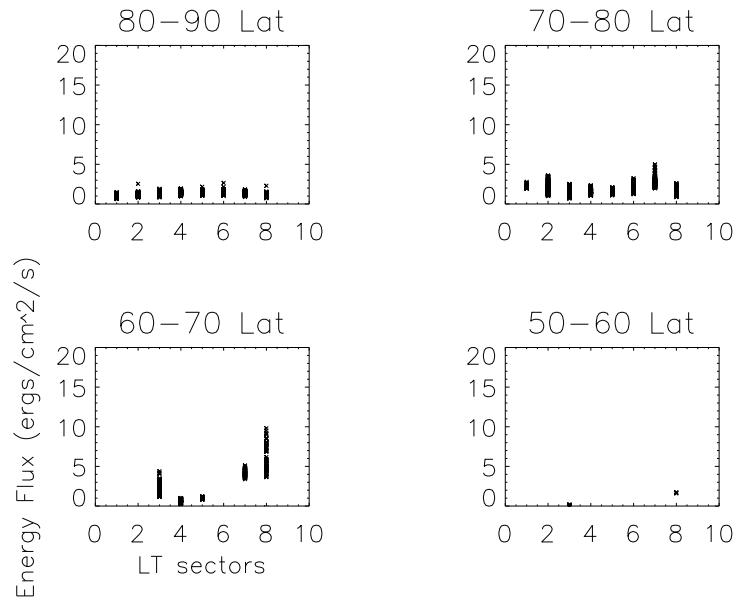
(a) Main phase
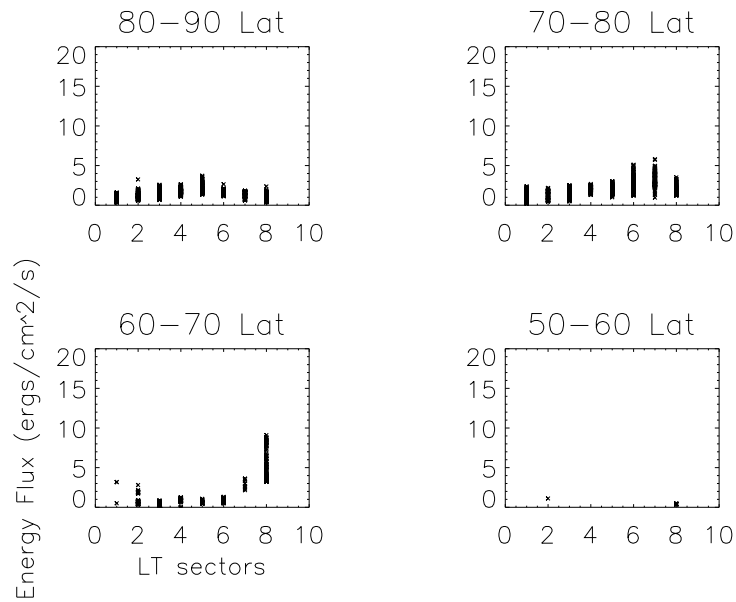
(b) Recovery phase

Figure 4.11 - Energy flux versus LT sector number for each 10° ML. Sector number refers to 3h LT intervals starting at midnight (0 LT). Main and recovery phases are displayed in panels (a) and (b). SRP (Event 2)
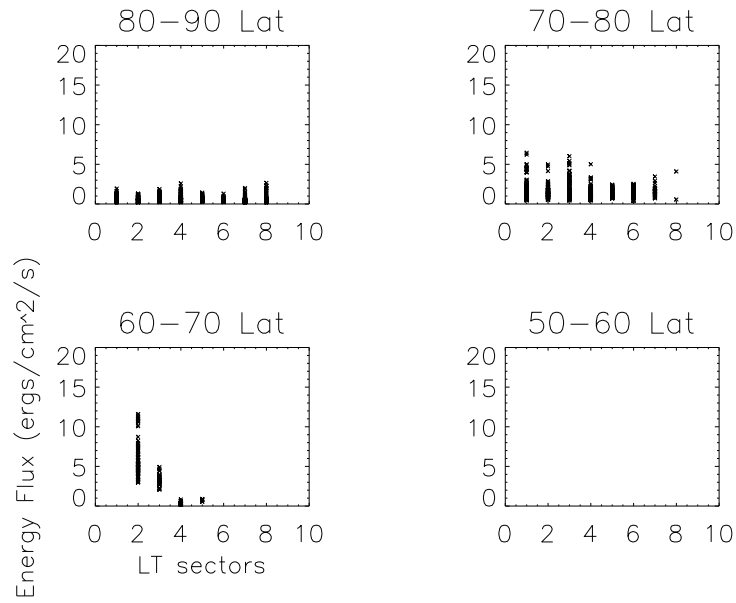
(a) Main phase
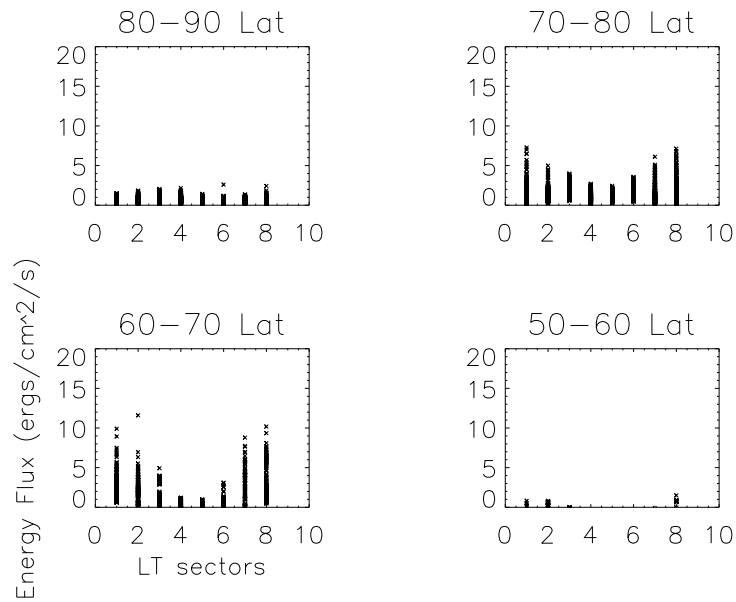
(b) Recovery phase

Figure 4.12 - Energy flux versus LT sector number for each 10° ML. Sector number refers to 3h LT intervals starting at midnight (0 LT). Main and recovery phases are displayed in panels (a) and (b). LRP (Event 4)

4.2 Relation between UVI auroral power and geomagnetic indices

Fluctuations in the magnetic field are addressed to external souces of the Earth (JACOBS, 1987). The evolution and intensity of such magnetic variations can be monitored by geomagnetic indices. This important tool yields information on the geomagnetic activity level as well as about the magnetospheric processes and mechanisms.

Geomagnetic indices can be compared to other physical parameters in order to obtain clues about the solar wind-magnetosphere interaction. Particle precipitation in the auroral region during magnetic storms have a questionable source. Thus, the auroral power input can be compared to geomagnetic indices, which, in turn, are related to global measurements of the processes occurring in the magnetosphere.

Correlation coefficient is a direct measurement of how two data set (X,Y) vary jointly and is defined by:

$$r = \frac{covariance\ of\ X\ and\ Y}{(standard\ deviation\ of\ X)(standard\ deviation\ of\ Y)}. \tag{4.1}$$

In this work, correlation between precipitating power input and geomagnetic indices was calculated during main and recovery phases for the six studied events. Electron precipitation influence has been investigated on the low and high latitude current systems. Table 4.1 and 4.2 bring the correlation coefficients between power and geomagnetic indices for main and recovery phases. The correlation could not be computed during main phase of Event 1 due to the lack of data.

In order to complement the correlation estimate, precipitating power versus high and low latitude geomagnetic indices during main and recovery phases are displayed in Figures 4.13 to 4.18. Auroral indices as AE, AL and AE are shown in the first column while Dst, SYM-H and ASY-H named equatorial indices are found in the second column.

Table 4.1 - *Correlation between auroral power input and geomagnetic indices for the main phase of the events.*

Events	AE	AL	AU	Dst	SYM	ASY
2 (SRP)	-0.79	0.58	-0.85	-0.91	-0.87	-0.15
3 (SRP)	-0.31	0.45	0.09	-0.28	-0.28	0.12
4 (LRP)	0.88	-0.9	0.04	-0.82	-0.87	0.84
5 (LRP)	0.61	-0.6	0.34	-0.62	-0.61	0.1
6 (LRP)	0.39	-0.41	0.05	-0.13	-0.08	0.17

Table 4.2 - *Correlation between auroral power input and geomagnetic indices for the recovery phase of the events.*

Events	AE	AL	AU	Dst	SYM	ASY
1 (SRP)	0.94	-0.93	0.80	-0.92	-0.92	0.85
2 (SRP)	0.79	-0.86	-0.03	-0.79	-0.84	0.90
3 (SRP)	0.5	-0.47	0.33	-0.67	-0.59	0.66
4 (LRP)	0.58	-0.48	0.6	-0.61	-0.53	0.61
5 (LRP)	0.3	-0.19	0.37	-0.58	-0.67	-0.06
6 (LRP)	0.49	-0.43	0.47	-0.54	-0.61	0.47

Power-index relations for the recovery phase of the Event 1 (SRP) are shown in Figure 4.13. There was not enough data for the main phase. Clearly, two groups are identified in the plots, one at lower power and index values and the other one for higher values. The slight power (less than 10 GW) is found to be associated with low magnetic activity around 8 doy UT. Precipitating power is well correlated with all the indices as observed through the correlation coefficients obtained in table 4.2 although that is not obvious from the plots. Precipitating electrons seem to be linearly associated with the total ring current and the auroral eletroject enhancements which suggests that the magnetic storm is a consequence of global processes.

Event 2 (SRP) is displayed in Figure 4.14. There is a low energy group of less than 10 GW in the main phase, which does not behave as the majority data. During main phase, only ASY-H index does not present good correlation to auroral power, which means that the asymmetric ring current is not clearly associated with the auroral electron precipitation in this event stage. The fact that AE, AU and AL indices are in good agreement with power

Figure 4.13 - Auroral power input versus geomagnetic indices. AE, AL and AE are displayed in the first column while Dst, SYM-H and ASY-H are found in the second column. Recovery phase (Event 1-SRP).

suggest precipitating electrons strongly influence the auroral electrojets. In the recovery phase, all indices present good correlation coefficient with exception of the AU index. The relation of AE, AL and ASY-H indices and power can be easily seen in the plots. Thus, precipitating electrons may be associated with the westward eletroject and somehow with the ring current increase.

During the main phase of the Event 3 (SRP), there is no clear relation between precipitating power and geomagnetic indices as observed in Figure 4.15 and confirmed by the computed correlation coefficients. Apparently, it is noticed a high energy data group in the recovery stage, greater than 40 GW, for AE, AL and SYM-H, which does not change as much as the indices increase. Such data seems to be located near main-recovery phase transition which suggests that the energy input is not associated with the indices close to high activity peak (near Dst minimum) or maybe the magnetic field variation is caused by another source but electron precipitation. Table 4.2 shows a bad correlation coefficient for AU index. It is believed that the correlation coefficients for AE, AL and SYM-H would be higher if that group data was neglected. Anyway, it is agreed that electron precipitation may not affect eastward electrojet in this case.

Power input is observed as well related to the geomagnetic indices, except AU index,

during the main phase of the Event 4 (LRP), as shown in Figure 4.16 and by the correlation coefficients. Hence, electron energy input does not affect linearly the eastward electrojet. In the recovery phase, besides the data looks spread in energy range along the indices, it is possible to observe good relations for all geomagnetic indices. This indicates that the particle precipitation in this case is a consequence of a global phenomenon which may contribute to the long recovery phase duration.

During Event 5 (LRP), displayed in Figure 4.17, only AE index is easily seen to be related linearly with power input though the correlation coefficients indicate that only AU and ASY-H are clearly not related to the precipitating energy. This way, the westward eletroject and symmetric ring curren enhancement may be associated with electron precipitation. For the recovery time, SYM-H index suggests that the symmetric ring current increases at the same pace as particle precipitation energy. This fact is an indicator that the long recovery phase can be associated with a ring current enhancement or to the same energy source.

Figure 4.18 brings magnetic storm Event 6. During main phase there is no clear relation between energy input and the indices. In the recovery phase, AE and AL may have a good agreement with precipitating power though it is not obvious. Correlation coefficient is higher for SYM-H which suggests that the symmetric current increase may be related to electron precipitating in the auroral region.

All the magnetic storms seem to be linearly related to the ring current enhancement during recovery phase, some of them with only the symmetric part. Most of the recovery stages are also associated with both electrojet increases and sometimes only to the westward system, but never to the eastward component. Correlation coefficients are low for Event 6, but looking at Figure 4.18, non-correlation between AE/AL and auroral power is not clear.
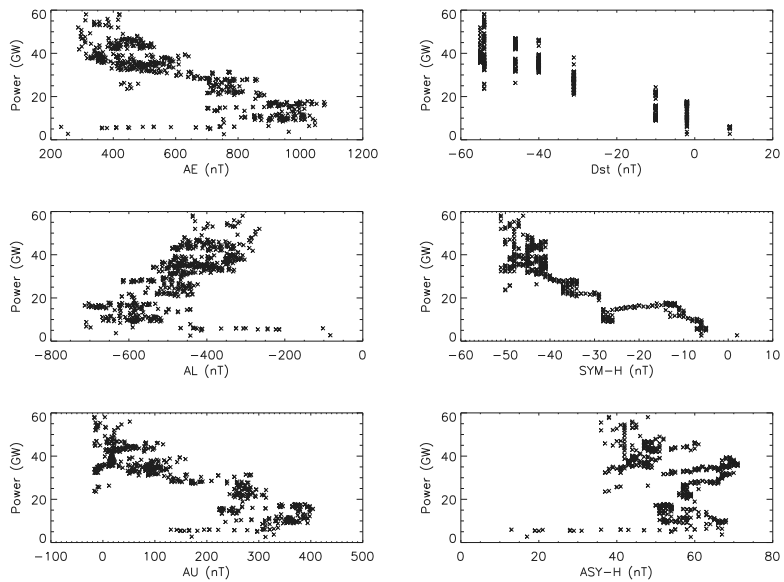
(a) Main phase
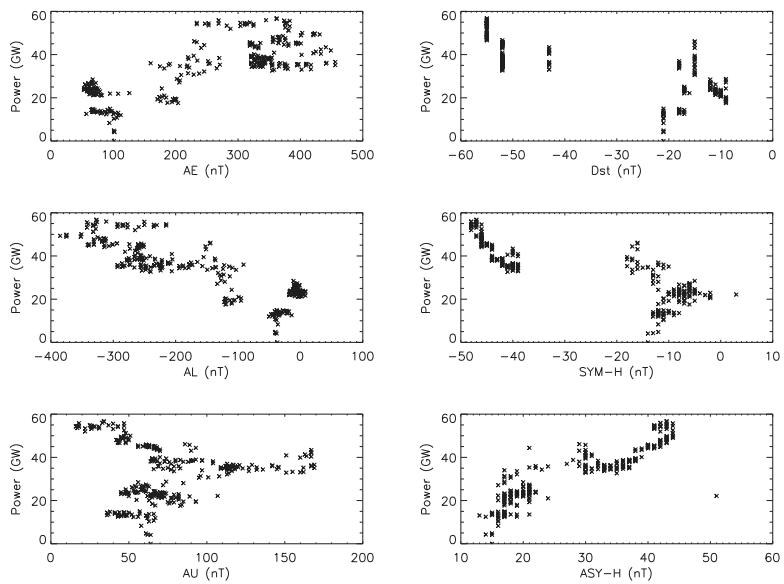
(b) Recovery phase

Figure 4.14 - Auroral power input versus geomagnetic indices. AE, AL and AE are displayed in the first column while Dst, SYM-H and ASY-H are found in the second column. (Event 2-SRP)
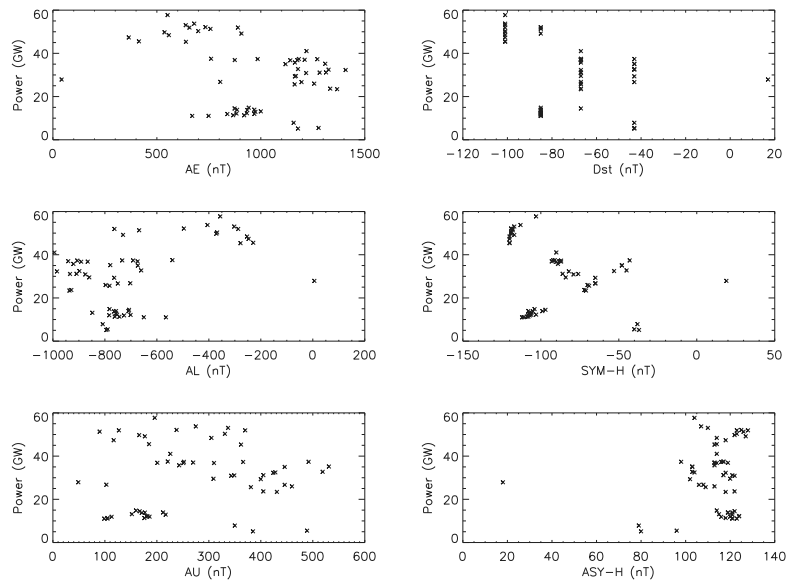
(a) Main phase
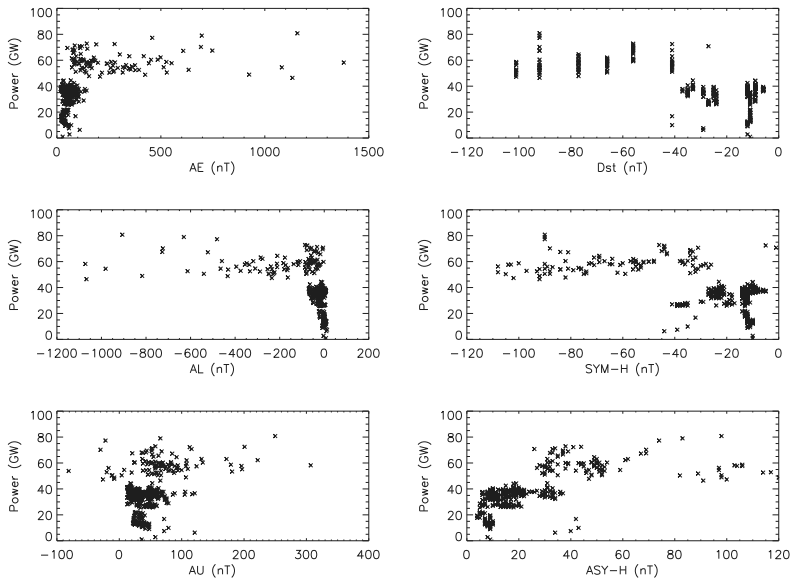
(b) Recovery phase

Figure 4.15 - Auroral power input versus geomagnetic indices. AE, AL and AE are displayed in the first column while Dst, SYM-H and ASY-H are found in the second column. (Event 3-SRP)
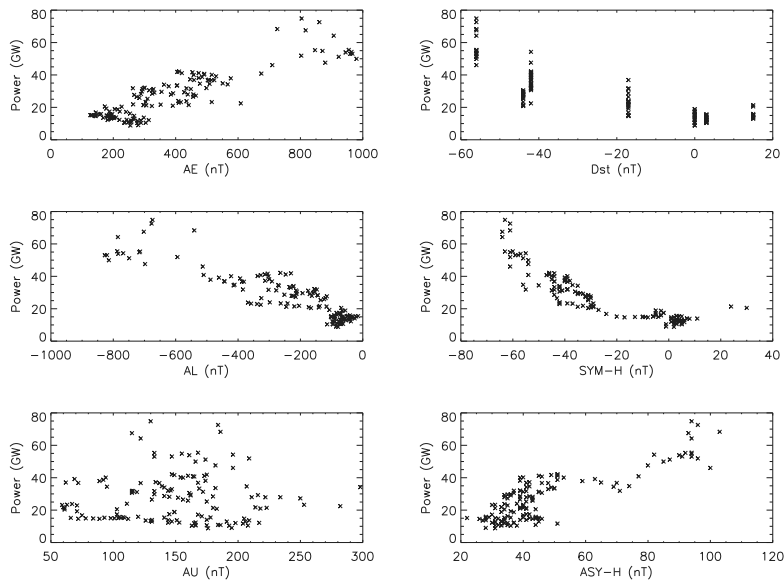
(a) Main phase
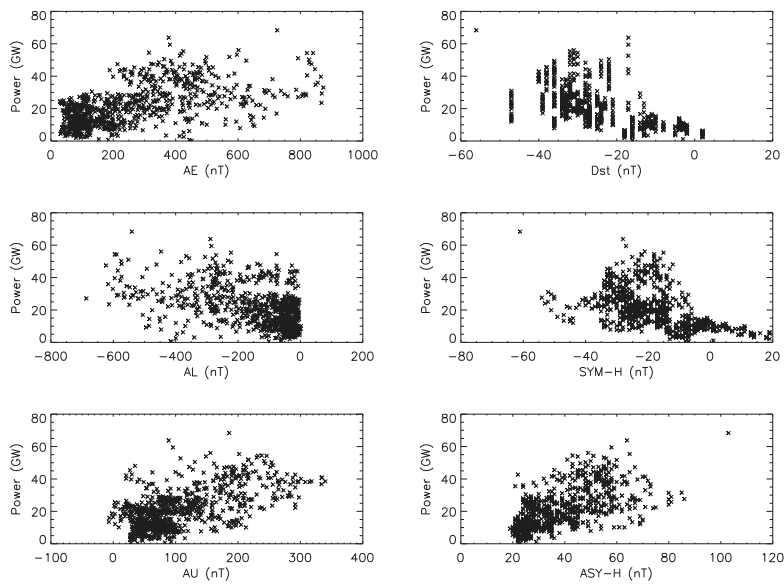
(b) Recovery phase

Figure 4.16 - Auroral power input versus geomagnetic indices. AE, AL and AE are displayed in the first column while Dst, SYM-H and ASY-H are found in the second column. (Event 4-LRP)
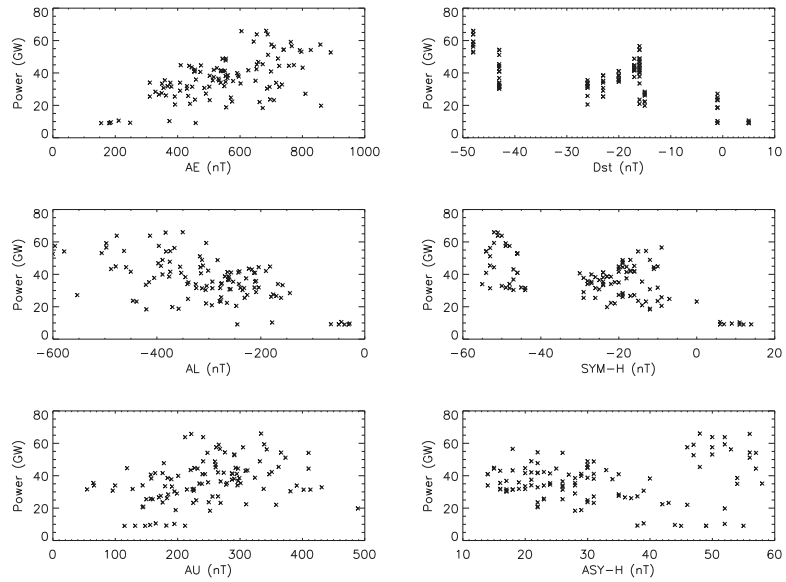
(a) Main phase
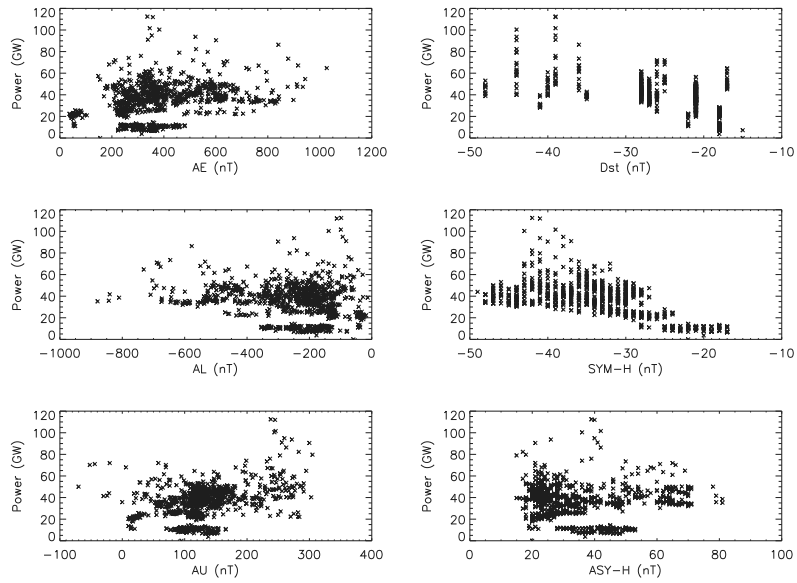
(b) Recovery phase

Figure 4.17 - Auroral power input versus geomagnetic indices. AE, AL and AE are displayed in the first column while Dst, SYM-H and ASY-H are found in the second column. (Event 5-LRP)
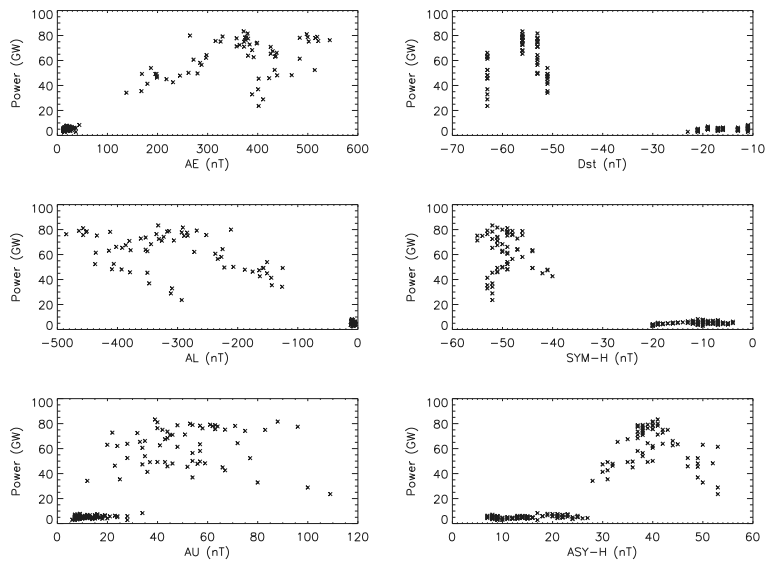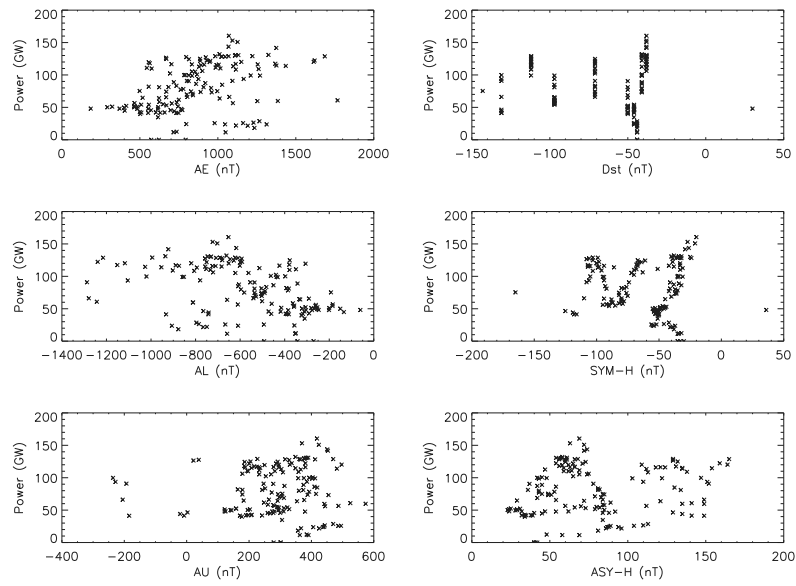
(a) Main phase
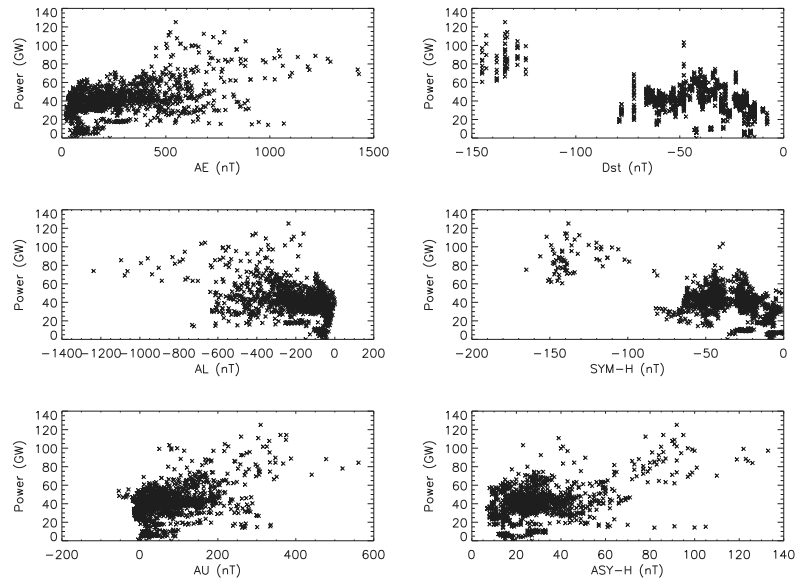
(b) Recovery phase

Figure 4.18 - Auroral power input versus geomagnetic indices. AE, AL and AE are displayed in the first column while Dst, SYM-H and ASY-H are found in the second column. (Event 6-LRP)

4.3 Empirical auroral power from geomagnetic indices and Hemispheric Power

In the past, there was no way to monitor directly precipitation energy in function of time. Energy dissipation had to be derived empirically from ground-based measurements, particularly from geomagnetic indices. Akasofu (1981) expected that precipitating particle power U_A would vary in harmony with AE index and proposed simple linear relationships between both:

$$U_A(erg\ s^{-1}) = 10^8 \times AE(\gamma), \tag{4.2}$$

where γ is an unit of magnetic field and is equal to 1 nT.

Particle injection energy is believed to be related to the heigh-integrated Hall conductivity ((AHN et al., 1983) and references therein). Most of the particle precipitation contribution comes from near ionization density profile peak, around 90 km to 130 km. It is also conceived that electrons below 125 km are the main source of heigh-integrated Hall conductivity. North-south component of magnetic disturbance field is associated with the heigh-integrated Hall conductivity, and then, particle energy input can also be related to it. Ahn et al. (1983) compared the calculated injected energy and auroral geomagnetic indices and obtained empirical linear relations given by:

$$U_A(W) = 0.6 \times 10^8 \times AE(nT), \tag{4.3}$$

$$U_A(W) = 0.8 \times 10^8 \times AL(nT). \tag{4.4}$$

Ostgaard et al. (2002) claims we should not expect a linear relation between electron energy deposition and geomagnetic indices. They obtained that this relation has to be described by a nonlinear relation, under assumptions that the AE index is due to ionospheric Hall currents and the polar cap potential slightly saturates for large AE values. They calculated precipitating particle energy from UVI and X-ray emissions for five isolated substorms. The strong and weak correlation with AL and AU, respectively, suggest

that U_A and Hall conductance increase are related to the westward electrojet but not to the eastward system. They found that a nonlinear relation between the auroral indices, selected only from well located stations, and the precipitating power fits better to the data as follows:

$$U_A(GW) = 4.6AE^{1/2}(nT) - 23, \tag{4.5}$$

$$U_A(GW) = 4.4AL^{1/2}(nT) - 7.6, \tag{4.6}$$

where the constants -23 GW and -7.6 GW indicate that there are still currents flowing when there is no precipitation.

Nowadays, precipitation energy input can be estimated also from instruments on board satellites, and not only from geomagnetic indices. Besides the UVI energy estimate developed in this work, energy deposition is monitored by NOAA POES Hemispheric Power as well (EMERY et al., 2006; EMERY et al., 2008). The power deposited in the polar regions by energetic particles is estimated during spacecraft transits over the poles. Power flux observations obtained during a single pass of the satellite over a polar region (which takes about 25 minutes) are used to estimate the total power deposited in an entire polar region by these auroral particles.

Energy deposition by auroral precipitation can then be estimated by ground and space-based instruments. A comparison between those methods is important mainly with respect to the comprehension of processes dominating the auroral eletrojects. Figures 4.19 to 4.24 bring auroral precipitating power calculated from the geomagnetic indices AE (blue crosses) and AL (black triangles), estimated by UVI images (red x's), and the hemispheric power (green squares) for all the events. Power input derived from linear empirical relations given by Equations 4.3 and 4.4 are shown in panel (a). The estimated power from nonlinear method described by Equations 4.5 and 4.6 is displayed in panel (b).

During Event 1 (SRP), as presented in Figure 4.19, nonlinear relation derived from AL seems to fit better to UVI estimate (Figure 4.19(a)). In this case, the linear evaluation underestimates our UVI power input calculation (Figure 4.19(b)). Hemispheric power sometimes overestimates power from all other methods.

Deposition power for Event 2 (SRP) is displayed in Figure 4.20. During main phase, neither linear nor nonlinear power from geomagnetic indices have similar behavior to

UVI input power. Nonlinear estimate seems to be closer to UVI power values since linear aproximation underestimates it.

During Event 3 (SRP), power from UVI looks shifted to that from empirical methods as observed in Figure 4.21. Deposition power is better estimated by linear relations in the main phase while nonlinear fits reasonably in the recovery phase though none really describes the UVI power input.

Precipitating electron power from UVI images behaves similarly to that obtained by linear functions in Event 4 (LRP), as seen in Figure 4.22. Nonlinear method seems to overestimate power quantity, even compared to Hemispheric power, which sometimes is above real values. It is important to notice that the high variability on the electron injection energy observed previously in the UVI method in this case is also seen in the empirical form outcome.

Linear method also fits better in the Event 5 (LRP) which is displayed in Figure 4.23. As previous case, nonlinear function seems to overestimate the power input. Following previous LRP behavior, Event 6 is better described by linear methods, as seen in Figure 4.24. Again, nonlinear functions derive power values much higher than that from our UVI method.

Looking only into the recovery phase of the events and choosing for linear or nonlinear methods, precipitation power derived from UVI aproximates more to that obtained by nonlinear functions during SRP phenomena. The opposite is observed in the LRP magnetic storms group, where UVI power fits better to linear method results.
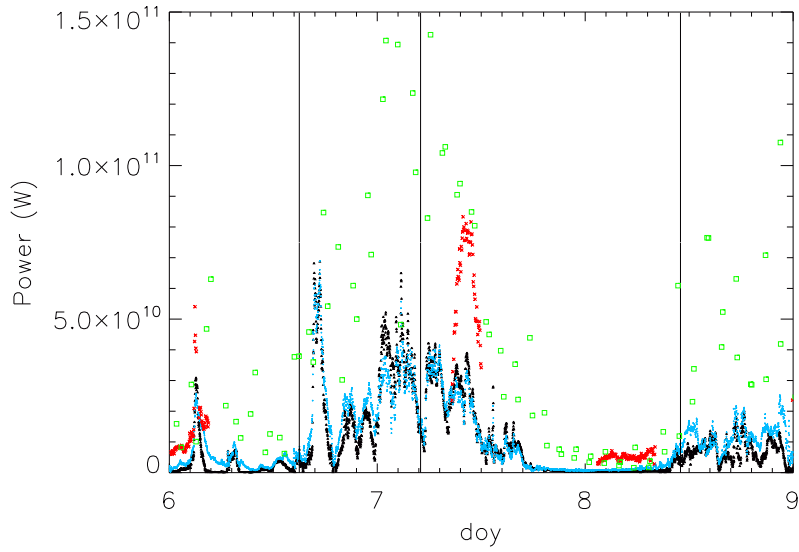
(a) Linear empirical method
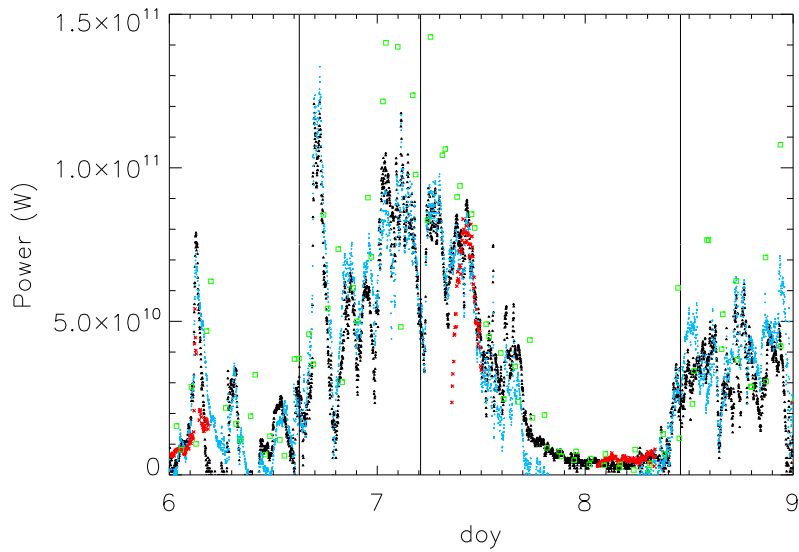
(b) Nonlinear empirical method

Figure 4.19 - Auroral precipitating power (Watts) derived from different measurements. Black triangles and blue crosses represent power derived from AL and AE index, respectively. Red x's refer to the power computed from UVI images. Green squares designate Hemispheric Power. Event 1-SRP
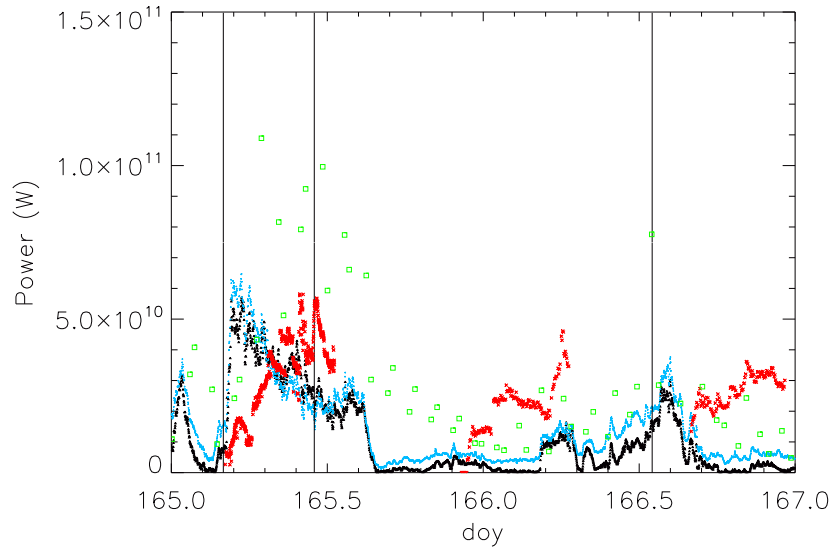
(a) Linear empirical method
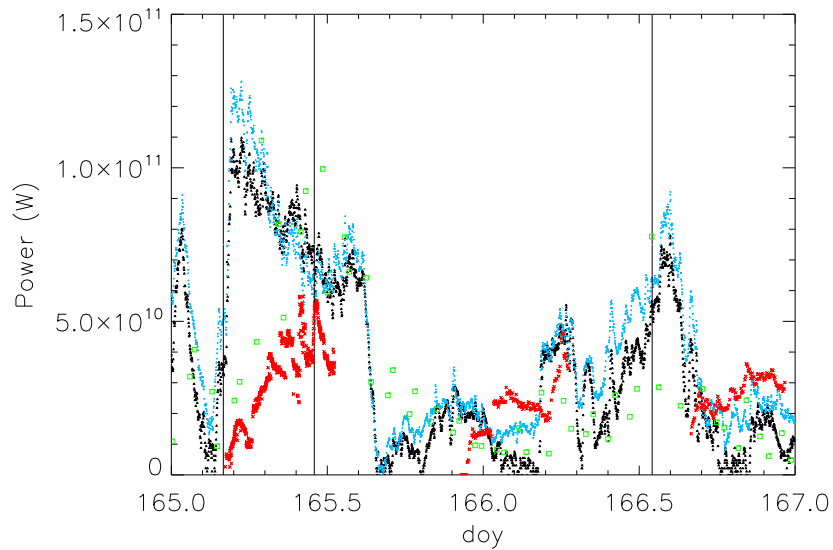
(b) Nonlinear empirical method

Figure 4.20 - Auroral precipitating power (Watts) derived from different measurements. Black triangles and blue crosses represent power derived from AL and AE index, respectively. Red x's refer power computed from UVI images. Green squares designate Hemispheric Power. Event 2-SRP
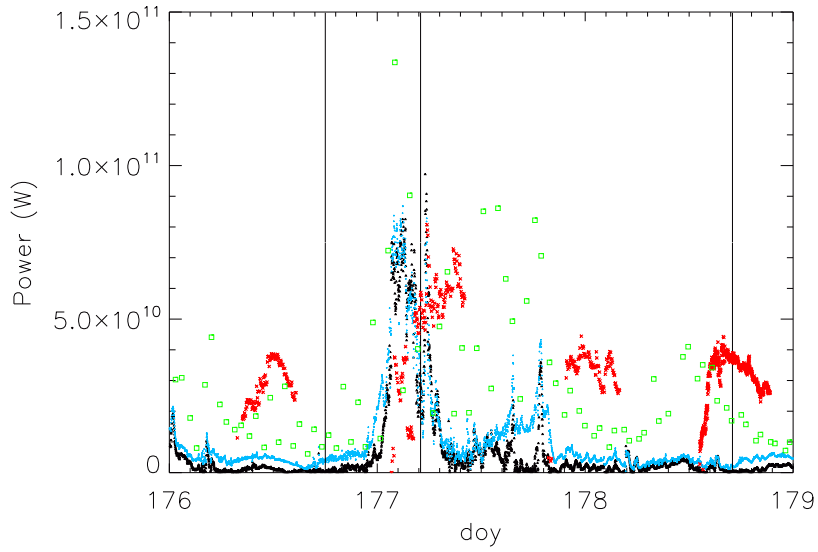
(a) Linear empirical method
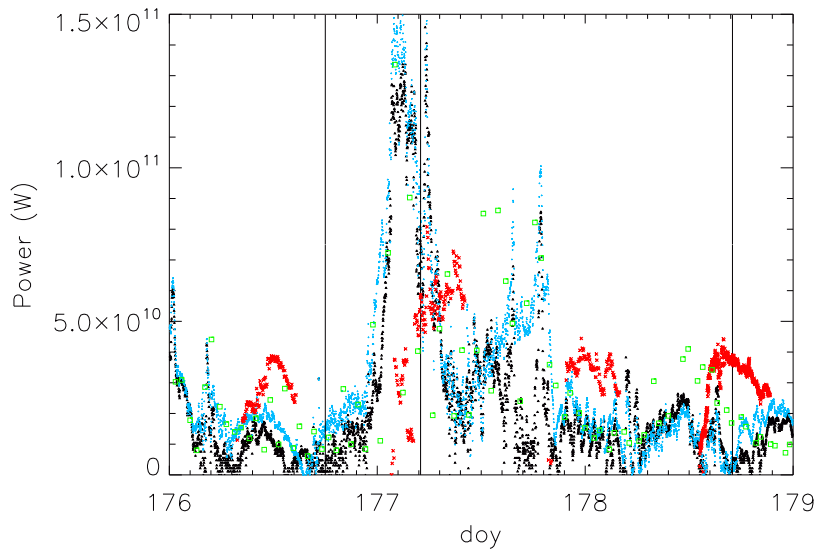
(b) Nonlinear empirical method

Figure 4.21 - Auroral precipitating power (Watts) derived from different measurements. Black triangles and blue crosses represent power derived from AL and AE index, respectively. Red x's refer power computed from UVI images. Green squares designate Hemispheric Power. Event 3-SRP
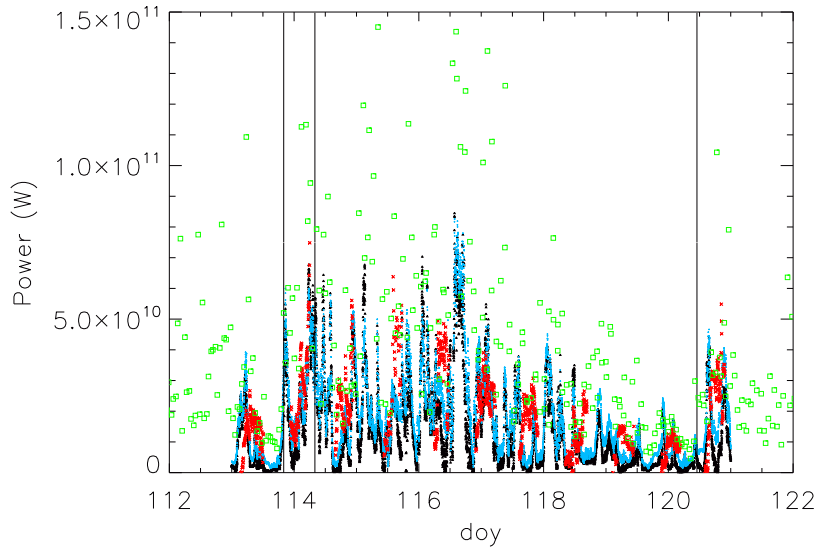
(a) Linear empirical method
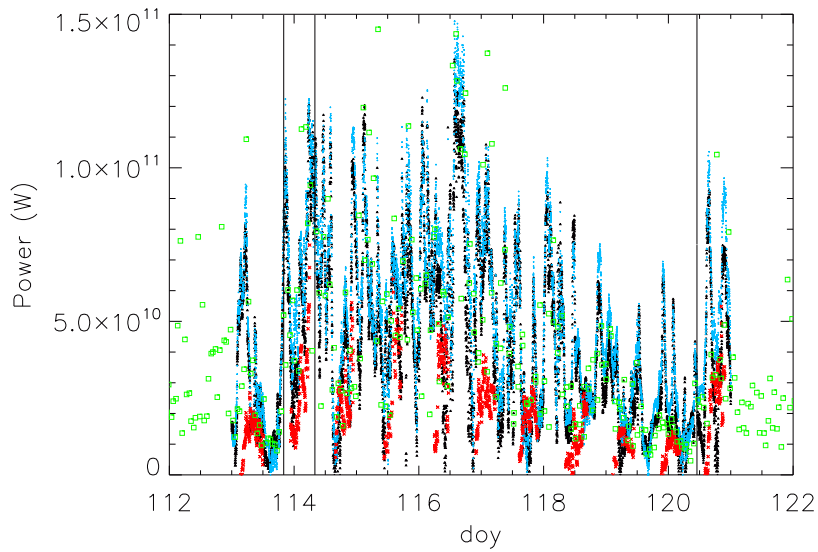
(b) Nonlinear empirical method

Figure 4.22 - Auroral precipitating power (Watts) derived from different measurements. Black triangles and blue crosses represent power derived from AL and AE index, respectively. Red x's refer power computed from UVI images. Green squares designate Hemispheric Power. Event 4-LRP
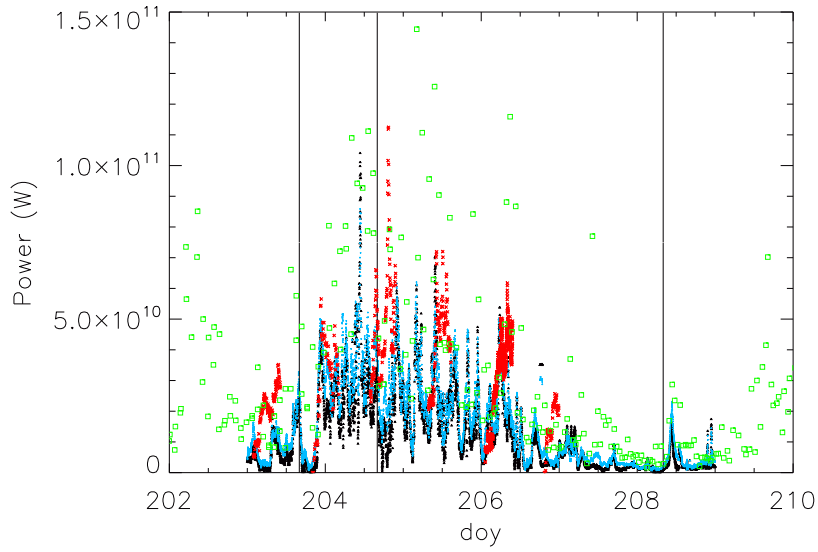
(a) Linear empirical method
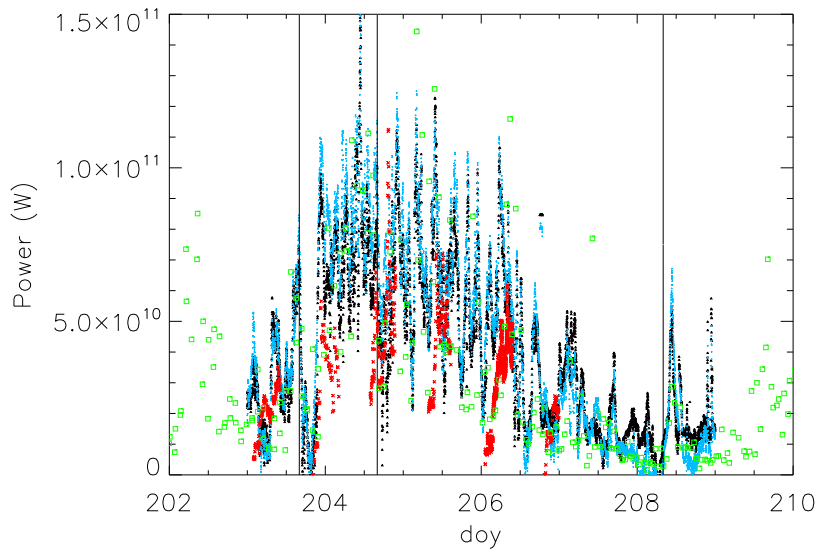
(b) Nonlinear empirical method

Figure 4.23 - Auroral precipitating power (Watts) derived from different measurements. Black triangles and blue crosses represent power derived from AL and AE index, respectively. Red x's refer power computed from UVI images. Green squares designate Hemispheric Power. Event 5-LRP
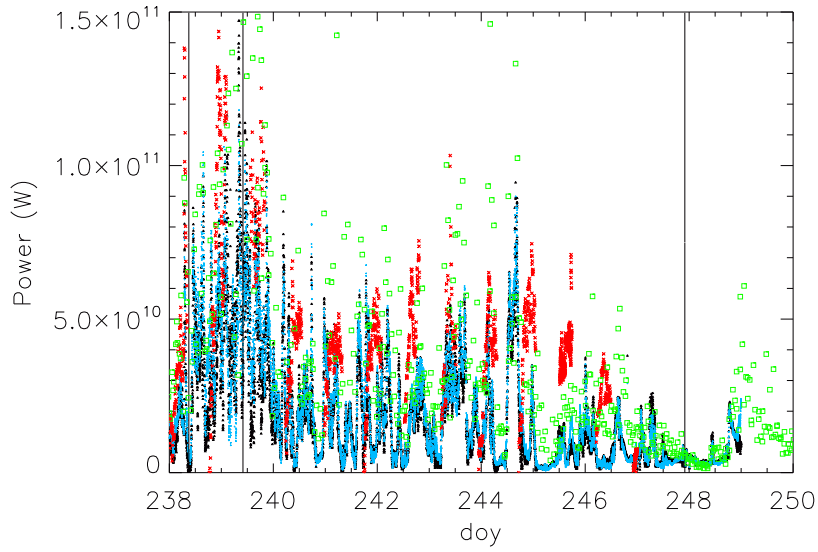
(a) Linear empirical method
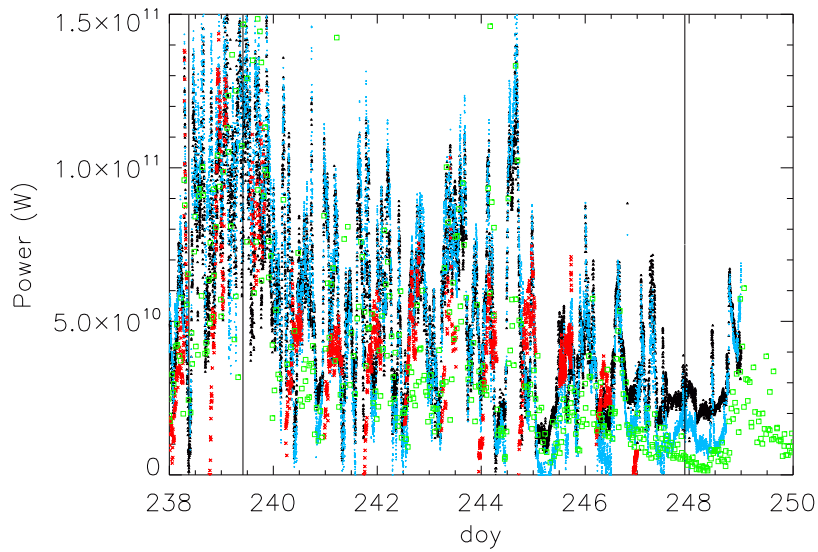
(b) Nonlinear empirical method

Figure 4.24 - Auroral precipitating power (Watts) derived from different measurements. Black triangles and blue crosses represent power derived from AL and AE index, respectively. Red x's refer power computed from UVI images. Green squares designate Hemispheric Power. Event 6-LRP

5 RESULTS: AURORA SPATIAL FEATURES

Aurora viewed from space by a global imager appears as diffuse, continuous, luminous bands that surround both geomagnetic poles at ionospheric altitudes (FREY, 2007). An oval-shaped band around the polar regions is atributed to the strong asymmetry in the location of the aurora on the dayside and nightside (KIVELSON; RUSSEL, 1995). The upward field-aligned current regions are found to be coincident with the ovals, where electrons flow into the ionosphere. Hence, the location and shape of the aurora yield information on the spatial evolution of electron precipitation.

UVI images provide spatial and temporal behavior of the aurora, and subsequently, of the auroral precipitation. It was possible to calculate energy flux, in function of Local Time (LT) and Universal Time (UT) for each $10°$ latitude and 3 hours UT sector, from UVI images. Figures 5.1 to 5.6 bring energy flux for $50°$ to $90°$ region, divided in panels for each $10°$ latitude range, for all the six selected magnetic storms. Coordinate system used is magnetic, since the auroral oval is displayed around magnetic dipole axes. First two vertical lines refer to main phase while last two lines correspond to recovery phase interval. Color bar refers to log scale energy flux. White color regions are related to absence of data. Only regions where the area is completely covered by the UVI field of view are considered, and for this reason, there is almost no data for some latitude ranges.

Figure 5.1 corresponds to Event 1 (SRP). Energy flux during main phase is intense for the nightside, extending from $60°$ to $90°$ latitude. Also, high energy flux values are noticed in the first part of the recovery phase (around time value of 7.5 doy) from 18 to 24 LT and for $60°$ to $90°$ latitude range. There is still some magnetic activity in the recovery phase final portion although the intensity is weaker.

Energy flux during Event 2 (SRP) is displayed in Figure 5.2. According to the available data, energy flux is more intense close to midnight for $60°$ to $70°$, around 18 LT for $70°$ to $80°$ and about midday for $80°$ to $90°$, during the recovery phase. For this magnetic storm, a sequence of UVI images with dayglow removed and LOS correction applied is also presented in Figure 3.7. During main period, the oval is very intense. Auroral activity decreases in the recovery phase, when becomes intense again corresponding to Dst and AE peaks.

Figure 5.3 corresponds to Event 3 (SRP). The same characteristics as previous event are noticed, that is, energy flux is more intense close to midnight for $60°$ to $70°$, around 18

73

LT for 70° to 80° and about midday for 80° to 90°, during the recovery phase.

Event 4 is shown in Figures 5.4 and 3.8. Magnetic activity is seen over all MLT. This is also observed in UVI images even when the recovery phase is getting ended, which is not noticed during SRP phenomena.

Aurora looks to be spread all over the oval during Events 5 (Figure 5.4) and 6 (Figure 5.6) as well. The region near dusk seems to present higher energy flux values in the 70° to 80° interval.

In summary, our results suggest the electron precipitation seems to occur over all the oval for LRP events. On the other hand, SRP magnetic storms do not present such characteristics, but show strong magnetic activity near dusk. A deep investigation about this topic has not been performed during this work besides the intense and uncountable UVI image handlings.
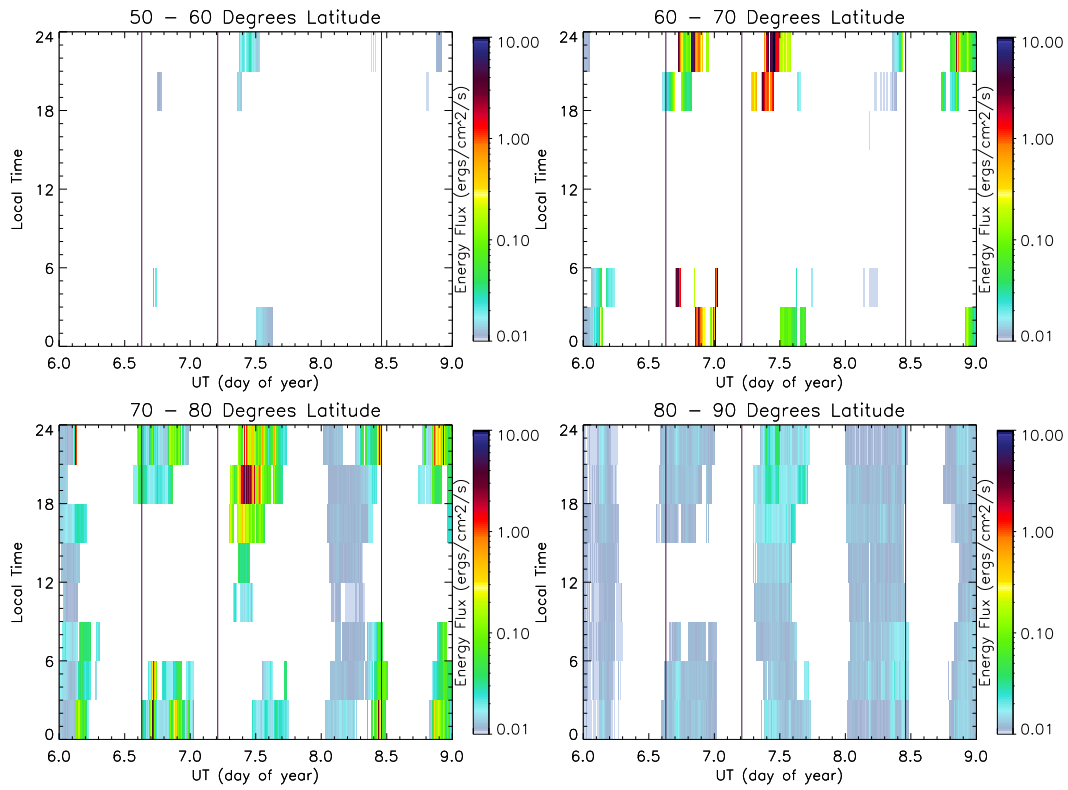
Figure 5.1 - Log scale energy flux ($ergs/scm^2/s$) in function of Local Time (LT) and Universal Time (UT) for each $10°$ latitude interval covering $50°$ to $90°$ region. January 6-8, 1998, SRP (Event 1).
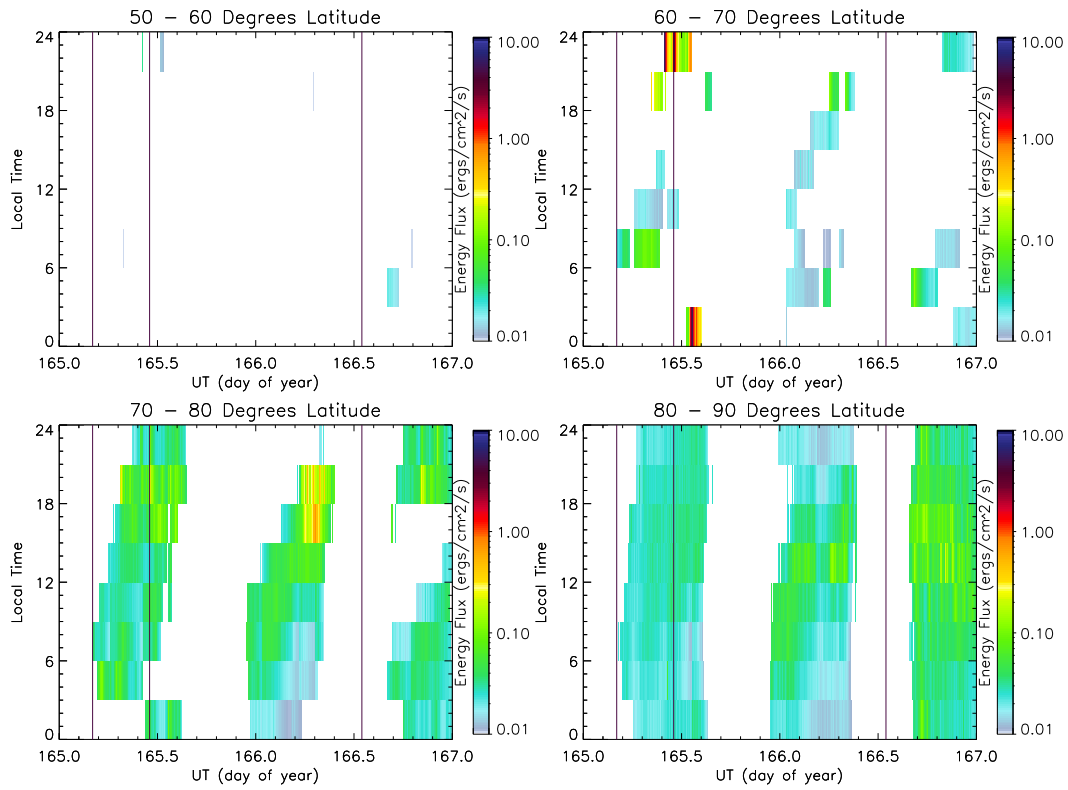
Figure 5.2 - Log scale energy flux in function of Local Time (LT) and Universal Time (UT) for each 10° latitude interval covering 50° to 90° region. June 14-16, 1998, SRP (Event 2).
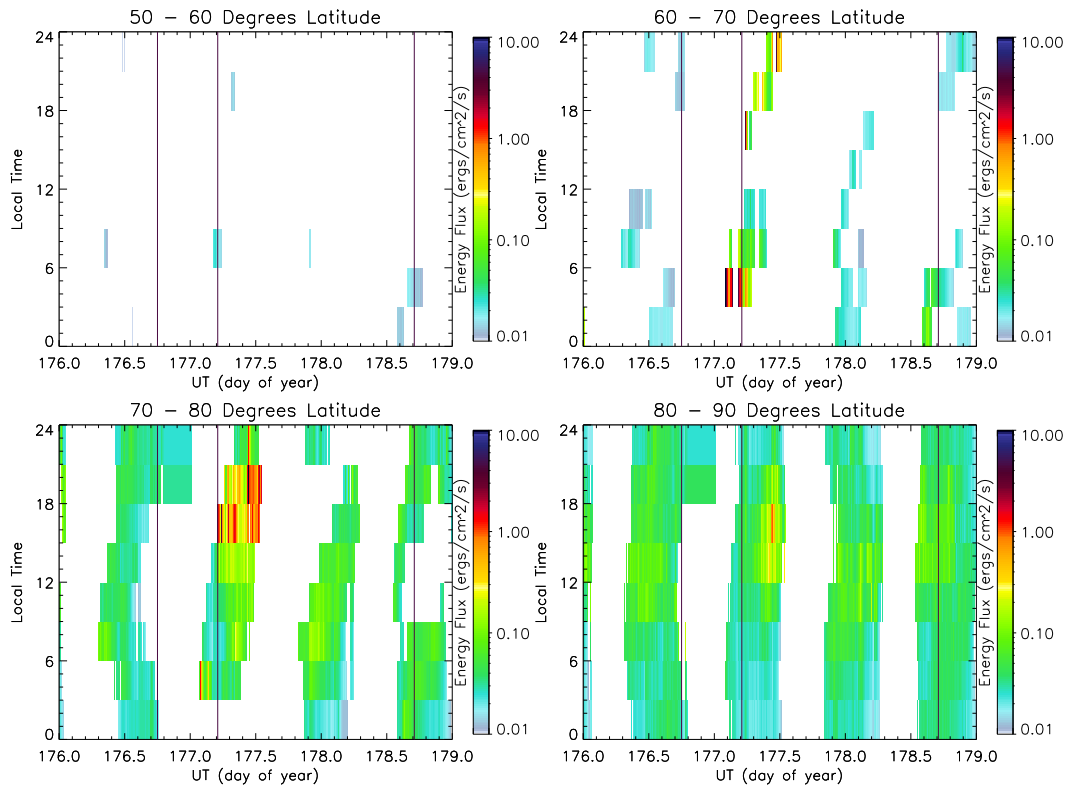
Figure 5.3 - Log scale energy flux in function of Local Time (LT) and Universal Time (UT) for each 10° latitude interval covering 50° to 90° region. June 25-27, 1998, SRP (Event 3).
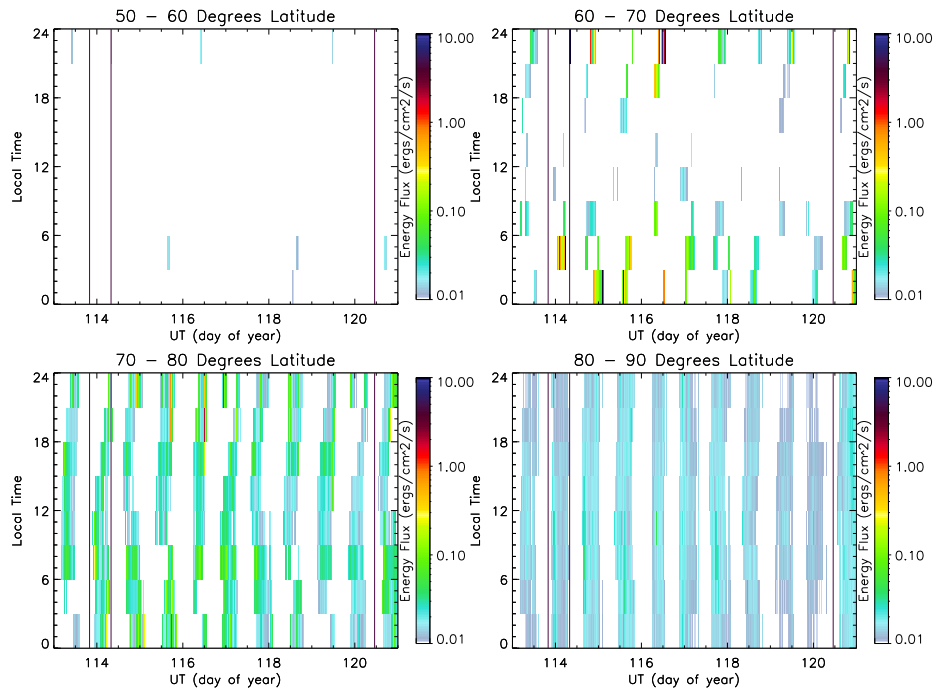
Figure 5.4 - Log scale energy flux in function of Local Time (LT) and Universal Time (UT) for each 10° latitude interval covering 50° to 90° region. April 23-30, 1998, LRP (Event 4).
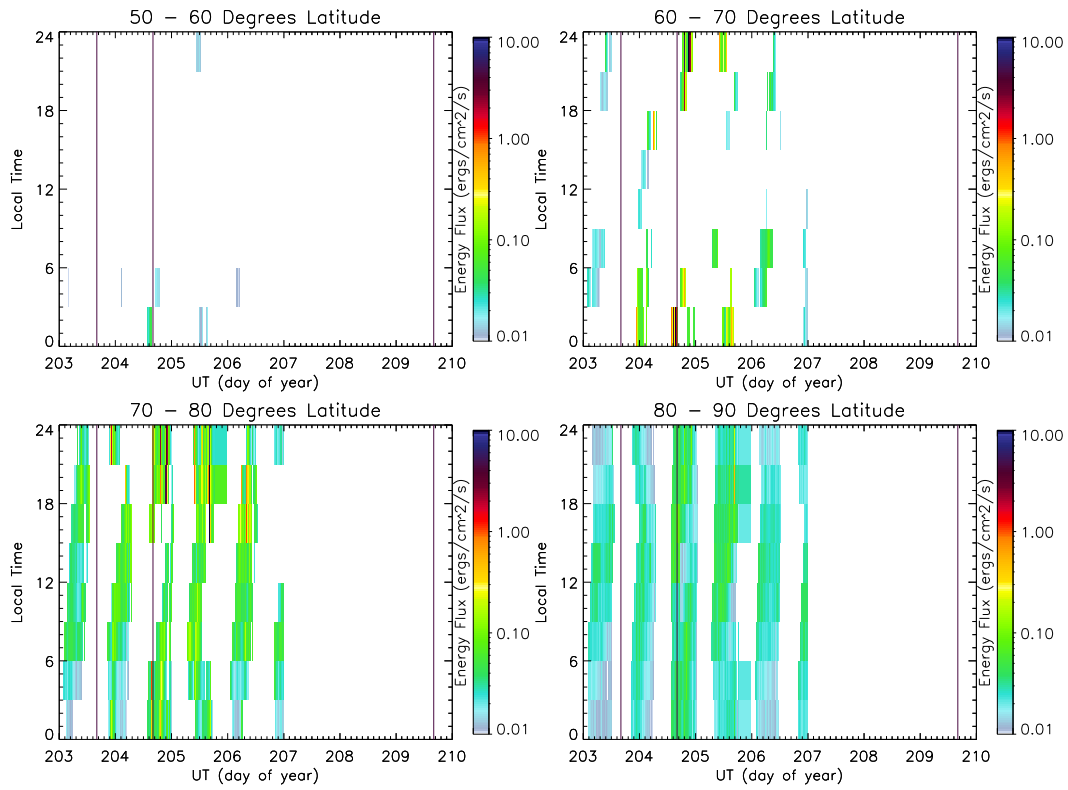
Figure 5.5 - Log scale energy flux in function of Local Time (LT) and Universal Time (UT) for each 10° latitude interval covering 50° to 90° region. July 22-29, 1998, LRP (Event 5).
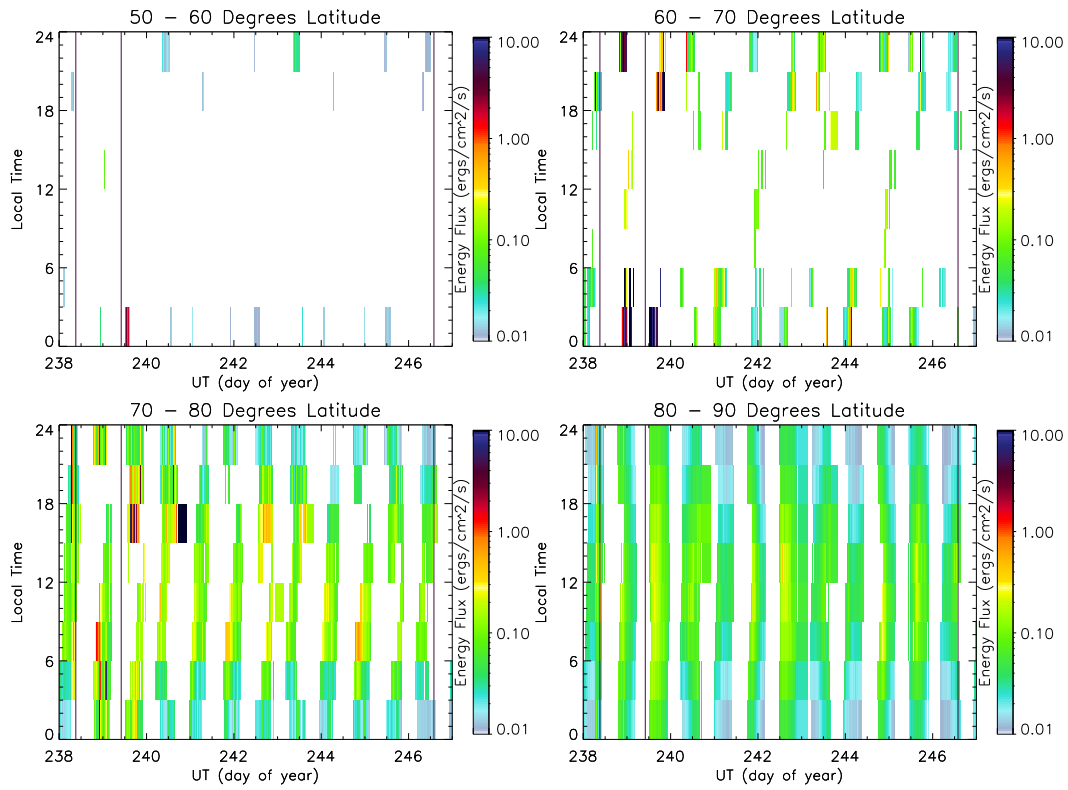
Figure 5.6 - Log scale energy flux in function of Local Time (LT) and Universal Time (UT) for each 10° latitude interval covering 50° to 90° region. August 26 to September 3rd, 1998, LRP, (Event 6).

6 RESULTS: INFLUENCE OF THE SOLAR WIND

Solar wind strongly influences magnetospheric dynamics although the processes and mechanisms still remain unknown. Empirical relations also yield information on the energy input from solar wind-magnetosphere coupling which is responsible by the energy dissipated in the ring current, joule heating and auroral precipitation. Energy estimate is based on solar wind parameters considered important on the magnetosphere dynamics. UVI electron precipitating and solar wind input energy are then compared in Section 6.1, in order to investigate the role of the solar wind on the auroral activity.

Solar wind conditions have been investigated during the events in Section 6.2. The intention here is to verify if there is a relation between auroral precipitation behavior during SRP and LRP events and the solar wind characteristics.

6.1 Solar wind power input

Energy deposition by electron precipitation derived from auroral emissions through UVI images and from empirical functions based on geomagnetic indices has been shown in this work so far. In doing this, energy transfer processes between particle injection and the magnetospheric current systems could be investigated.

Besides studying the energy transfer mechanisms inside the magnetosphere, it is essencial to look at the major process driving the different magnetospheric phenomena. The coupling between solar wind and earth magnetic field is believed to be responsible for the large amount of injected energy into the magnetosphere. This solar wind energy input is then mostly converted into particle precipitation in the auroral region, Joule heating and ring current enhancement ((AKASOFU, 1981; OSTGAARD et al., 2002)).

At present, there is no direct observational measurements of the energy transfer from the solar wind to the magnetosphere. Even questions like exactly how and where such transfer occurs remain unanswered. Thus, solar wind parameters have been largely used as an attempt to obtain energy estimate available for the magnetospheric dynamics (GONZALEZ, 1990).

Akasofu (1981) introduced the ε parameter which is the energy input quantity in the solar wind responsible for the energy transfer to the magnetosphere (PERREAULT; AKASOFU, 1978). Such parameter depends on the solar wind speed v, the IMF intensity B, the clock angle θ (angle defined between y and z IMF component in the GSM coordinate system)

and the effective cross-sectional area l_0^2, and is defined in SI units by:

$$\varepsilon(W) = \frac{4\pi}{\mu_0} v B^2 sin^4(\theta/2) l_0^2. \tag{6.1}$$

The ε parameter is basicaly derived from the Poynting's theorem (KOSKINEN; TANSKA-NEN, 2002). The factor $\frac{4\pi}{\mu_0} v B^2$ corresponds to 4π times the Poynting vector magnitude calculated from upstream solar wind quantities and assuming that the magnetic field is perpendicular to velocity. The electric field $\mathbf{E}$ is given by vB, from the assumption that the conductivity approaches infinity, which is valid for space plasmas. The energy per unit of area per unit of time is described by the Poynting vector as follows:

$$\mathbf{S} = \frac{1}{\mu_0}(\mathbf{E} \times \mathbf{B}). \tag{6.2}$$

The parameter l_0^2 in Equation 6.1 is atributed to the effective cross-sectional area of the energy transfer (AKASOFU, 1981). Koskinen e Tanskanen (2002) claim that such factor with physical dimension of length is used for numerically scaling ε, in order to correspond to the dissipated energy inside the magnetosphere and to satisfy the physical dimension of power. Anyway, l_0 is assumed to not strongly depend on solar wind quantities and is estimated as $7R_E$, which corresponds to the magnetopause distance.

The strong dependence of ε on the clock-angle is addressed to the IMF north-south component influence on the energy transfer obtained empirically. The factor $sin^4(\theta/2)$ varies from 1 to 0 as the angle changes from $180°$ to $0°$ which yields larger amount of energy input to southward IMF values. In fact, it is believed that the magnetosphere is open under south IMF component conditions and the energy transfer between solar wind and magnetosphere is more intense. The clock-angle θ is defined as (AKASOFU, 1981):

$$
\begin{aligned}
\theta &= tan^{-1}(|B_y| / |B_z|) & for B_z > 0, \\
\theta &= 180 - tan^{-1}(|B_y| / |B_z|) & for B_z < 0.
\end{aligned} \tag{6.3}
$$

Figures 6.1 to 6.5 bring the solar wind input power computed from Equation 6.1 in black color and the electron precipitation power derived from UVI images in red for the studied magnetic storms. Solar wind data was obtained by ACE spacecraft. There is a lack of data during Event 1.
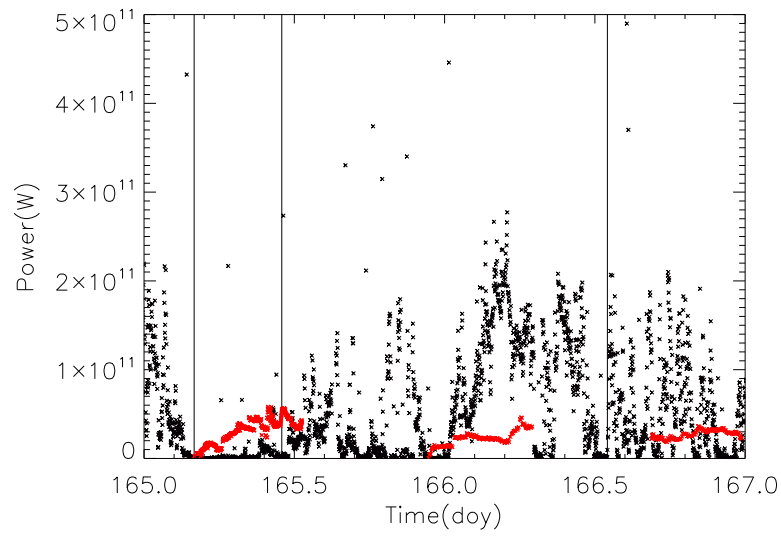
Figure 6.1 - Solar wind power input in black color and UVI electron precipitation power in red (Event 2-SRP).
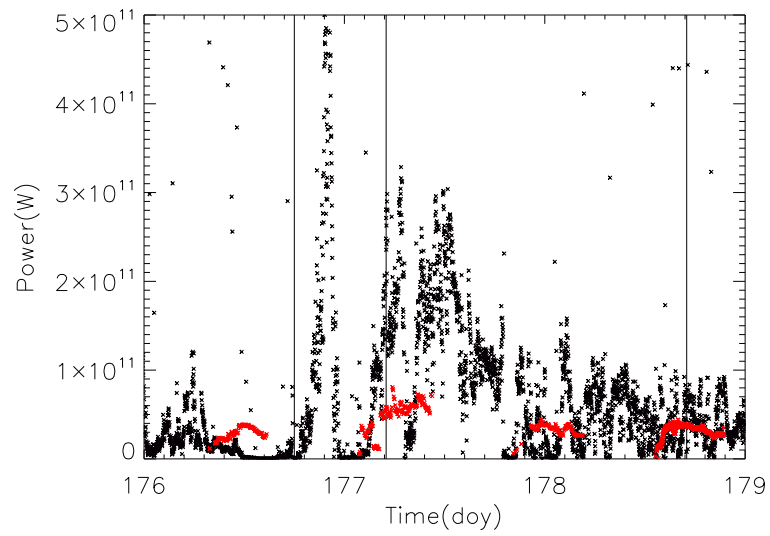
Figure 6.2 - Solar wind power input in black color and UVI electron precipitation power in red (Event 3-SRP).
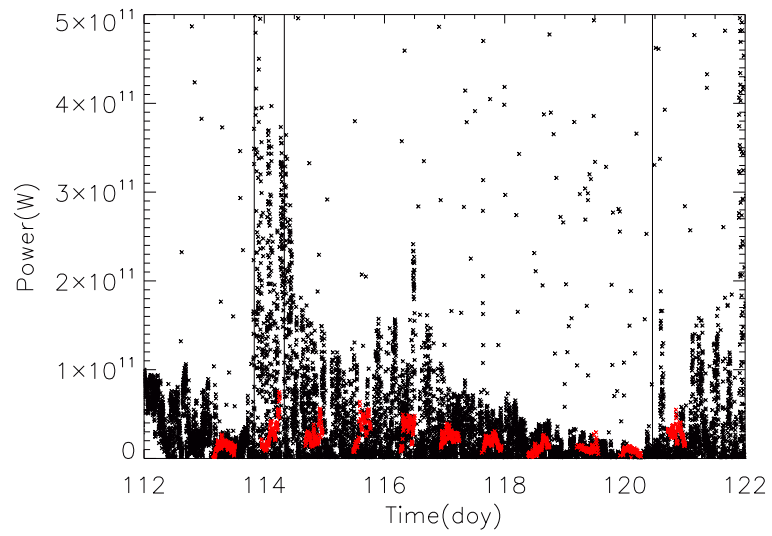
Figure 6.3 - Solar wind power input in black color and UVI electron precipitation power in red (Event 4-LRP).
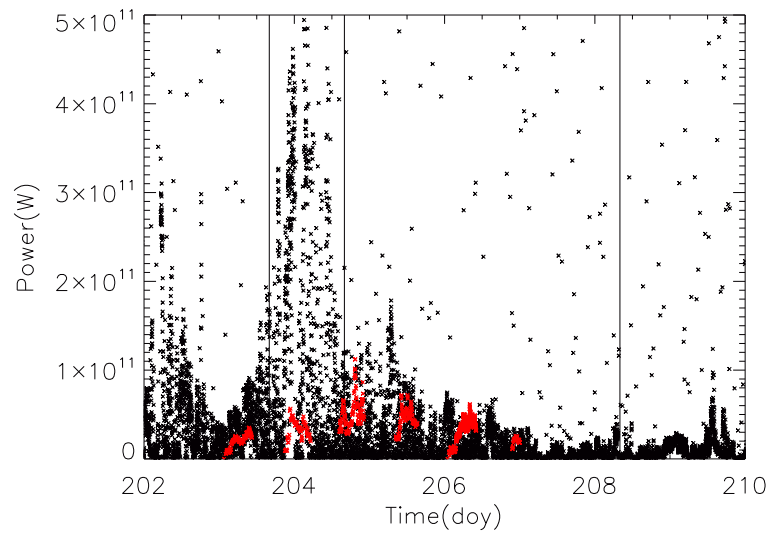
Figure 6.4 - Solar wind power input in black color and UVI electron precipitation power in red (Event 5-LRP).
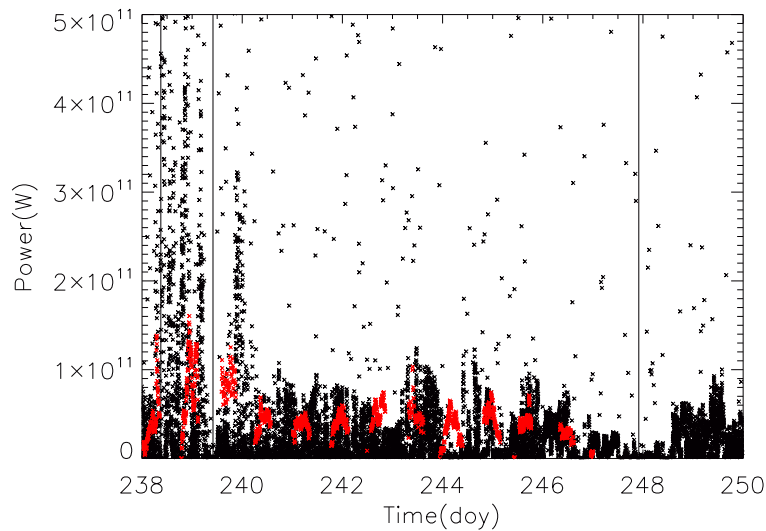
Figure 6.5 - Solar wind power input in black color and UVI electron precipitation power in red (Event 6-LRP).

SRP events are displayed in Figures 6.1 and 6.2. Apparently, there is no similar behavior between the solar wind coupling parameter and the electron precipitation in the polar region.

LRP featured magnetic storms are shown in Figures 6.3 to 6.5. The same standard fluctuation is seen in the solar wind input and precipitating deposition power quantities. Moreover, solar wind input reaches a maximum during main phase and the energy spikes are decreasing in intensity as the recovery phase comes to an end.

Akasofu (1981) claims that if the magnetosphere is assumed to initially store solar wind energy and afterwards converts the stored energy into substorm or magnetic storm energy, a simple relationship between ε and the dissipated energy would certainly not be simple. This system is so-called unloading system. On the other hand, if ε parameter correlates well, for instance, with the precipitating power, the magnetosphere would not be an unloading but a driven system. According to this, SRP magnetic storms could be an effect of an unloading system. However, this should be deeply investigated before come up as a statement. During LRP events, electron precipitation energy seems to follow quite well the energy input ε which can be an indicator of a driven system presence.

According to Tsurutani e Gonzalez (1987), HILDCAA events, characterized essencially by high and long-term auroral activity, are related to Alfvén waves, which present fluctu-

ating magnetic field. Southward turnings of the IMF would trigger reconnection processes in the magnetotail and would inject burst particles into the magnetosphere. Actually, solar wind input as well as the UVI precipitation energy show a pretty bursty feature. This also agrees with Akasofu (1981) work, since there would be no longtime energy store in progress.

The solar wind input energy, if deeply understood, could be a manner of monitoring energy deposition in the magnetosphere by a satellite located in front of the magnetosphere, in the upstream solar wind. This way, the coupling energy amount during a magnetic storm could be predicted before the event reaches the magnetosphere and, therefore, it would become possible to monitor continuously the space wheather.

6.2 What is going on in the solar wind?

Solar activity vary systematically over a period of 11 years and is measured by sunspot number amount (BURLAGA, 1995; EDDY et al., 1976). Sunspots are seen as dark regions due to the lower temperature compared to the surrounding photosphere. This is caused by the convection inhibition associated with the intense magnetic field. Solar active regions are related to coronal mass ejection (CME) which is the injection of coronal material into the solar wind and it is believed to emanate from the opening of magnetic-field structures in the Sun. CMEs can be followed by solar flares, defined as a sudden brightening of a small solar region seen in X-rays and emission lines. Coronal holes are open magnetic field line structures which are the origin of high-speed streams. A corotating interaction region (CIR) is formed by fast-slow solar wind intersection. Moreover, shocks are observed as descontinuities in the space properties, such as density, temperature and velocity, which changes abuptly. All those magnetic structures present in the interplanetary space added to solar activity variation affects the Earth's magnetosphere (KIVELSON; RUSSEL, 1995).

A study about electron deposition energy in the auroral region and its relation with the magnetospheric current systems as well as with the solar wind-magnetosphere coupling energy have been performed in this work. Continuing our search on the comprehension of magnetic storms characterized by long timescale recovery phases, it is interesting to investigate the solar wind parameters in the upstream side during the events.

Figures 6.6 to 6.10 bring solar wind parameters for the selected magnetic storms time interval. Magnetic field components B_x, B_y and B_z, and magnitude B are displayed in the first panel. Proton density and velocity components, v_x, v_y and v_z are shown in the second one. Coordinate system used is GSM. There is a lack of data for Event 1 time interval from ACE spacecraft.

Solar conditions for Event 2 (SRP) are shown in Figure 6.6. At about 164.8 doy, a structure with high density, reaching a maximum of 30 cm^{-3}, is detected. The magnetic storm starts around 0.4 day (9.6 hours) after that. In this case, B_z presents south-turnings during main phase, with a maximum value of -10 nT, and v_x only is increased by 14%, to -400 km/s. At the recovery phase, there is a slight density enhancement from 10 to 15 cm^{-3} and B_z comes to northward direction. At 166.2 doy, there is a B_z southward turning which coincides with auroral activity start seen in the AE index and falls in the Dst. AE seems to reflect pretty well the Bz profile.

During Event 3 (SRP), displayed in Figure 6.7, B_z turns to south at 176.9 doy after suddenly increased positively at around 176.65 doy. Magnetic storm main phase initiates at 176.75 doy. During this stage, magnetic field magnitude peaks at 18 nT and z-component at -15 nT. At 177.2 doy, B_z return to positive values which is coeherent with the recovery phase start. Around 177.6 doy, AE increases, Dst goes down and B_z gets small negative values. Density is seen as fluctuating and reaches 40 cm^{-3}, and v_x is always below 500 km/s.

Event 4 (LRP) presents high variable magnetic and velocity components as observed in Figure 6.8. Before 114 doy, there is a high density spike peaking at 70 cm^{-3}, B reaches 20 nT and the fluctuating feature begins. The recovery phase seems to initiate simultaneously with the density decrease and at the end of the higher amplitude fluctuating B_z. The peaks in Dst and AE indices observed at about 116.5 doy coincide with a spike in density and a longer interval of southward magnetic field. Sun-earth line speed peakes at 450 km/s.

As previously, Event 5 (LRP) is characterized by fluctuating behavior in magnetic field and velocity (Figure 6.9). Around 203.5 doy, density goes up to 20 cm^{-3}, B reaches 16 nT and B_z presents large amplitude disturbance (from -15 to 10 nT). Main phase starts at 203.67 doy. After 204 doy, x-component velocity increases to over 700 km/s. Recovery phase begins at 204.67 doy when velocity and magnetic field are found fluctuating and v_x is high.

Finally, Figure 6.10 brings solar parameters for Event 6 (LRP). Again, this LRP event is associated with disturbed magnetic field and velocity. A structure is observed after 238 doy when density peaks at 17 cm^{-3}, v_x reaches 850 km/s, B goes up to 20 nT and B_z fluctuates within negative values for longtime interval, until 240 doy. Main and recovery phase begins respectively at 238.4 and 239.4 doy. Magnetic field seems to go northward simultaneously with recovery phase stage initiation. There is a fast recovery feature up to 240 doy coincident with B_z rapid increase. Next, a slow recovery is observed when B_z fluctuates around zero. A major peak is noticed in Dst and AE indices, after 244 doy, at the same time as density gets high and B_z remains within negative values for a while.

The main differences between LRP and SRP are found in the disturbing magnetic field and velocity profile. B_z south-turnings are observed to be associated to Dst and AE peaks, which suggests particle injection into the magnetosphere. Magnetic storms with short recovery time are seen to be related to B_z maintenance at negative values for some hours, around 8 hours. During main phase, LRP events are characterized by large amplitude

fluctuating B_z around zero or even in negative values, as when it was sustained for more than one day in event 6. Fluctuation features in magnetic field and velocity are observed during longtime recovery phases.

According to Echer et al. (2005), the solar wind conditions for all the events refer to characteristics of a shock, except the Event 5, which is identified as a CIR.

Our results are in agreement with those found by Tsurutani e Gonzalez (1987), which says that Alfvén waves are responsible by HILDCAA phenomena. In fact, magnetic storms with long recovery phase are observed to be associated with magnetic field and velocity perturbation which can be an indicator of Alfvén waves presence. However, future work should be done in order to confirm our expectations.
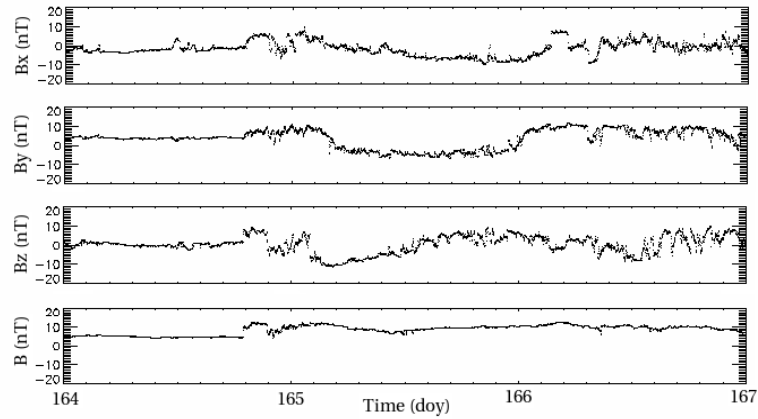
(a) Magnetic field components B_x, B_y and B_z, and magnitude B.
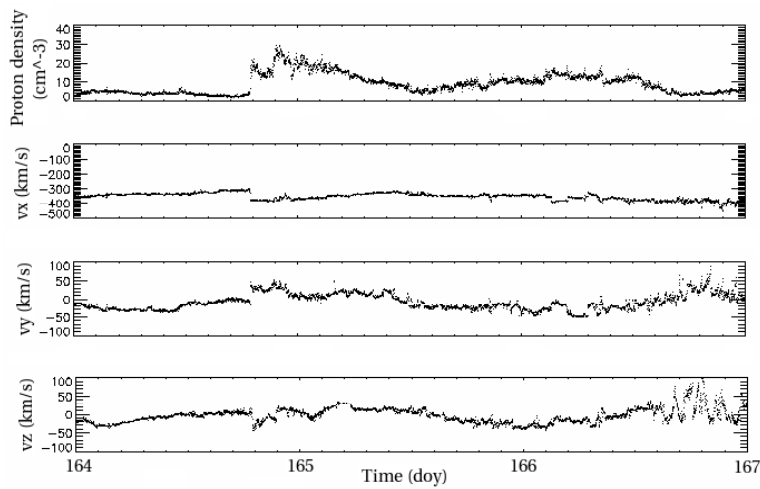
(b) Proton density and velocity components, v_x, v_y and v_z.

Figure 6.6 - Solar wind parameters measured by ACE. June 14-16, 1998, SRP (Event 2).
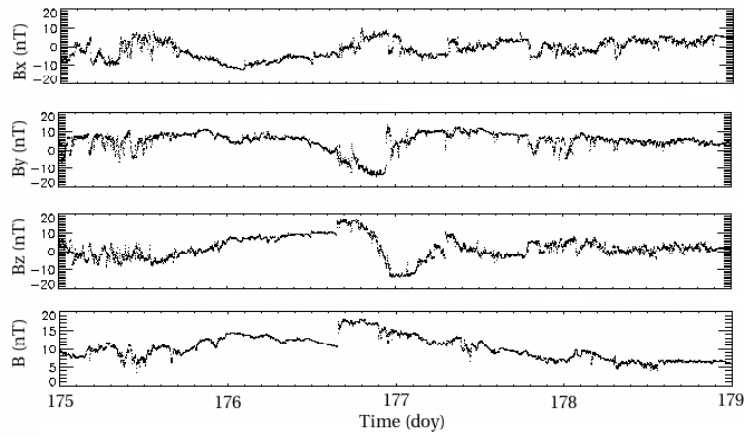
(a) Magnetic field components B_x, B_y and B_z, and magnitude B.
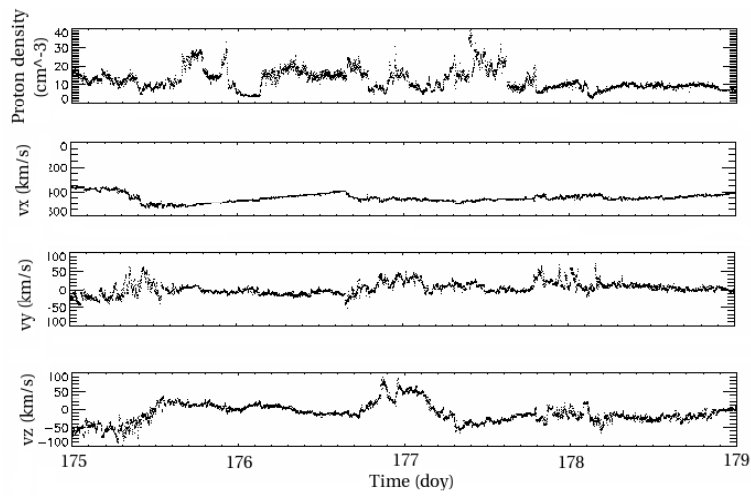
(b) Proton density and velocity components, v_x, v_y and v_z.

Figure 6.7 - Solar wind parameters measured by ACE. June 25-27, 1998, SRP (Event 3).
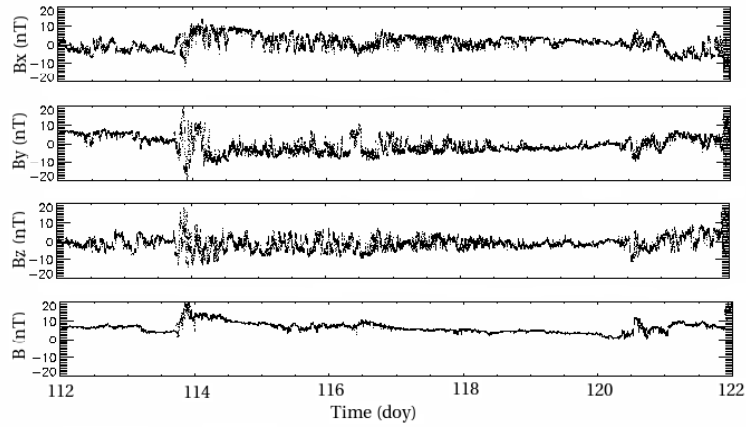
92

(a) Magnetic field components B_x, B_y and B_z, and magnitude B.
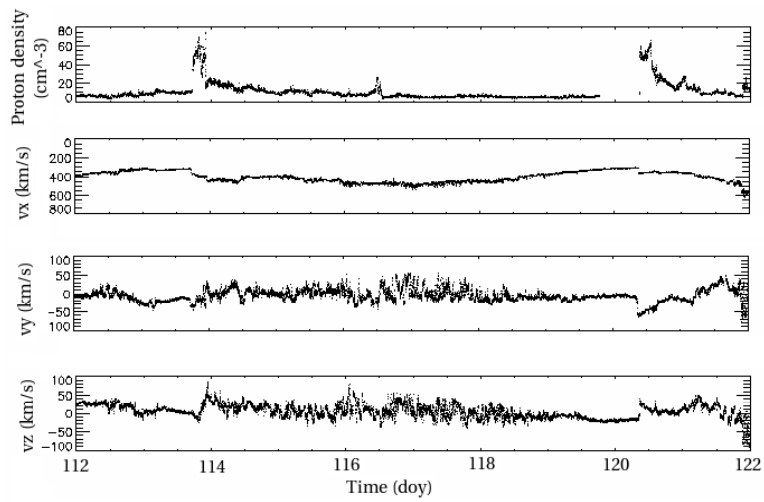
(b) Proton density and velocity components, v_x, v_y and v_z.

Figure 6.8 - Solar wind parameters measured by ACE. April 23-30, 1998, LRP (Event 4).
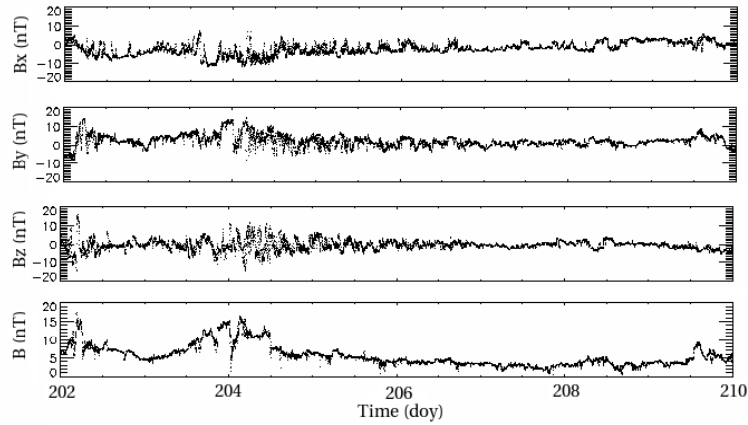
(a) Magnetic field components B_x, B_y and B_z, and magnitude B.
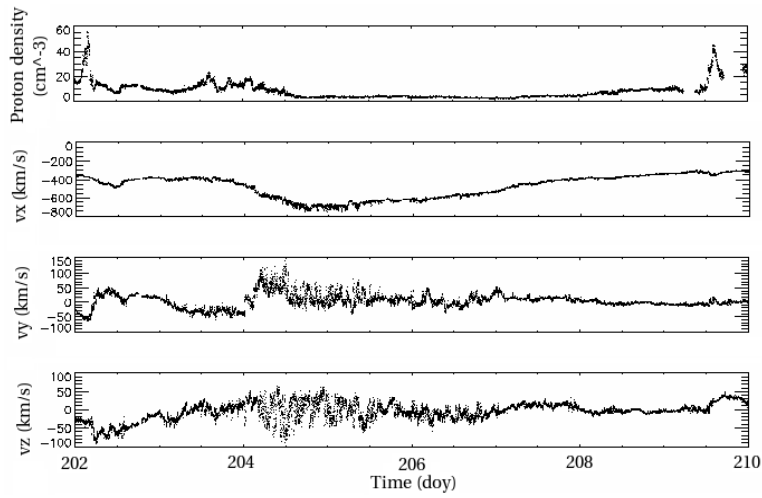
(b) Proton density and velocity components, v_x, v_y and v_z.

Figure 6.9 - Solar wind parameters measured by ACE. July 22-29, 1998, LRP (Event 5).
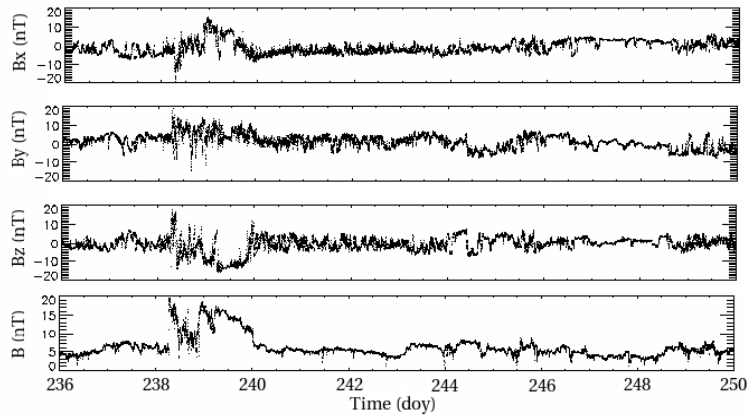
(a) Magnetic field components B_x, B_y and B_z, and magnitude B.
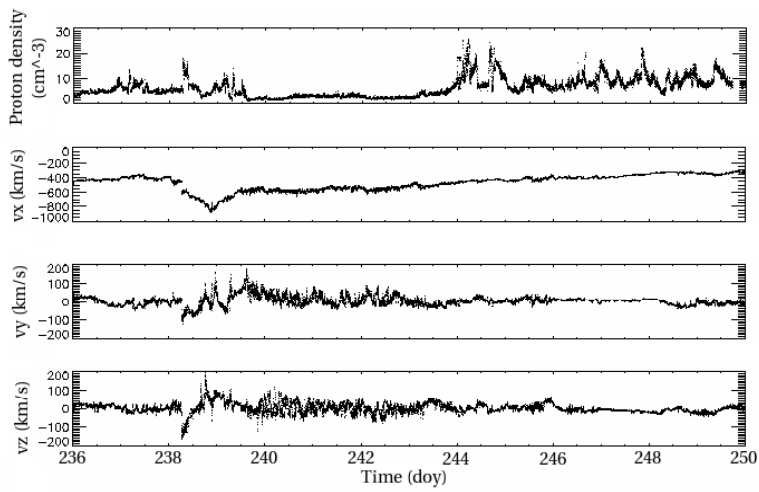
(b) Proton density and velocity components, v_x, v_y and v_z.

Figure 6.10 - Solar wind parameters measured by ACE. August 26 to September 03, 1998, LRP (Event 6).

7 CONCLUSIONS

Our daily activities are highly dependent on space-based technological systems and, for this reason, it has become essential to continuously monitor the space weather. The definition of Space Wheater has been settled as the conditions in the Sun and solar wind, magnetosphere, ionosphere and thermosphere, which can influence performance and reliability in ground or space-based technological equipments and also affects human health and life (BAKER, 1998; SISCOE, 2000; GOMBOSI et al., 2004; ECHER et al., 2005; SCHWENN, 2006; PULKKINEN, 2007).

The energy transfer mechanisms present in the solar wind-magnetosphere coupling and inside the magnetosphere have then also become an important issue. Particle precipitating energy investigation in the auroral region is a manner of trying to comprehend both transfer processes. In this work, precipitation energy influx could be calculated from auroral emissions within LBH long wavelength range measured by UVI instrument on board Polar spacecraft. One advantage of studying the aurora as a monitor of the near-Earth processes is that the size of the auroral oval differs in scale from the magnetosphere region by perhaps a factor of 10^6 (KIVELSON; RUSSEL, 1995).

The interaction between solar wind and magnetosphere is related to many magnetospheric phenomena such as magnetic storms, substorms and a more recent type so-called HILD-CAAs (High intensity long duration continuous AE activity). Some magnetic storm events present peculiar long recovery phase features (more than two days) and have been associated with HILDCAAs (TSURUTANI; GONZALEZ, 1987). In fact, all known processes for ring current decay, as charge exchange, Coulomb collisions, convection, wave-particle interactions, have time scales of hours to fraction of days (KOZYRA et al., 1997; KOZYRA et al., 2002).

In this work, it has been perfomed an investigation on the differences between magnetic storms with long (HILDCAA) and short recovery phases in terms of energy input. The six selected events have been organized into two groups, magnetic storms with short recovery phases (less than two days) named SRP events, and with long recovery phase features (more than two days) labeled as LRP events.

Auroral energy deposition has been derived from UVI images by applying adjustment methods such as spacecraft line of sight (LOS) correction and dayglow removal. The dayglow estimate method developed in this work evaluates dayglow energy which permits

to calculate auroral influx energy by removing known dayglow quantity from UVI images.

Electron precipitating energy flux computed for all the auroral region shows LRP events are more energetic and highly variable than SRP. Energy was calculated only for area values greater than 60% of the total auroral region considered as 50° to 90° ML. As UVI field of view varies significantly during the Polar orbit there may be still some area influence on the results. For this reason, energy flux was also estimated for sectors of a constant 10° ML and 3h LT area. Such results support those obtained for the total auroral region. The midnight region, considered here as 21 to 3 MLT, is observed as an active region presenting more variability for LRP than SRP events as well.

UVI data also shows, through energy flux versus local time sectors for each 10° ML, that near dusk region present large energy flux values mostly in the 70° to 80° ML range, indicating that the duskside is a very active region for magnetic storms in general. LRP seems to be a more energetic process although such difference does not look considerable. Energy flux versus UT and MLT together with UVI auroral images show strong magnetic activity near dusk mainly for SRP magnetic storms. Electron precipitation has been noticed to occur over all the oval for LRP events. Eventually, a deep investigation should be done in this case in order to permit more clear conclusions about the precipitation energy spatial behavior during LRP events.

Searching for effects of the auroral precipitation on the magnetospheric current systems, UVI energy flux has been compared to equatorial (Dst, SYM-H and ASY-H) and auroral (AE, AL and AU) geomagnetic indices. All the magnetic storms seem to be linearly related to the ring current enhancement during recovery phase, some of them with only the symmetric part. Most of the recovery stages are also associated with both electrojet increases and sometimes only to the westward system, but never to the eastward component.

Besides UVI energy estimate method, other manners of evaluating auroral precipitation energy have been used in this work. Hemispheric power is estimated from observations of particles influx by NOAA-POES extrapolated for the entire auroral region by statistical models. Linear (AHN et al., 1983) and nonlinear (OSTGAARD et al., 2002) empirical relations based on AE and AL indices, which are observed to reflect pretty well changes in the precipitating energy patterns, have also been used to obtain electron precipitation energy. During LRP magnetic storms, UVI power fits better to linear method results. This suggests that electron precipitation enhancement affects directly the auroral eletrojects,

especifically the westward system. On the other hand, SRP precipitation energy estimates are closer to nonlinear method although sometimes that is not very clear. Nonlinear empirical relations suppose AE saturates for high magnetic activities which might be happening during SRP events.

Solar wind strongly influences magnetospheric dynamics although physical processes and mechanisms still remain unknown. Empirical relations (AKASOFU, 1981) also yield information on the energy input resulted from solar wind-magnetosphere coupling which is mostly responsible by the energy dissipated in the ring current, joule heating and auroral precipitation. This energy estimate is based on solar wind parameters considered important on the magnetosphere dynamics. UVI electron precipitation and solar wind input energy have been then compared in order to investigate the role of the solar wind on the auroral activity. Apparently, there is no similar behavior between the solar wind coupling parameter and the electron precipitation in the polar region during SRP magnetic storms. The same standard of fluctuations is seen for LRP events in the solar wind input and precipitating deposition power quantities. Moreover, solar wind input reaches a maximum during main phase and the energy spikes are decreasing in intensity as the recovery phase comes to an end.

Akasofu (1981) claims that if the magnetosphere is assumed to initially store solar wind energy and afterwards converts the stored energy into substorm or magnetic storm energy, a relationship between ε and the dissipated energy would certainly not be simple. This system is so-called unloading system. On the other hand, if ε parameter correlates well, for instance, with the precipitating power, the magnetosphere would not be an unloading but a driven system. According to this, SRP magnetic storms could be an effect of an unloading system. During LRP events, electron precipitation energy seems to follow quite well the energy input ε which can be an indicator of a driven system presence.

According to Tsurutani e Gonzalez (1987), HILDCAA events, characterized essentially by high and long-term auroral activity, are related to Alfvén waves, which present fluctuating magnetic field. Southward turnings of the IMF would trigger reconnection processes in the magnetotail and would inject burst particles into the magnetosphere. Actually, solar wind input as well as the UVI precipitation energy show a pretty bursty feature. This also agrees with Akasofu (1981) work, since there would be no longtime energy store in progress.

Finally, upstream solar wind conditions have been investigated during all the events to

99

verify if there is a relationship between auroral precipitation behavior during SRP and LRP events and the solar wind characteristics. The main difference between LRP and SRP are found in the disturbing magnetic field and velocity profile. B_z south-turnings are observed to be associated with Dst and AE peaks, which suggests particle injection into the magnetosphere. Magnetic storms with short recovery time are seen to be related to B_z maintenance at negative values for some hours, around 8 hours. During main phase, LRP magnetic storms are characterized by large amplitude fluctuating B_z around zero or even in negative values, as when it was sustained for more than one day in Event 6. Within all cases, z-component magnetic fields reached negative values larger than 10 nT. The LRP events seem to be associated with fluctuations in magnetic field and velocity profiles although two of them are also related to high-speed streams.

Our results are in agreement with those found by Tsurutani e Gonzalez (1987), which says that Alfvén waves are responsible by HILDCAA phenomena. In fact, magnetic storms with long recovery phase are observed to be associated with magnetic field and velocity perturbation which is an indicator of Alfvén waves presence. Tsurutani et al. (1995) also conjecture that HILDCAA would be associated with large amplitude IMF fluctuations in corotating interactions regions (CIR), and consequently, this phenomenon would be related to fast-speed streams. However, our results show that high speed does not seem an essential parameter for LRP magnetic storms ocurrence but magnetic and velocity fluctuations would play an important role in this topic.

Besides all the work performed here, there are many questions still unanswered. The aurora during LRP events seems to be related to fluctuating magnetic field and velocity. However, the coupling mechanism between solar wind and magnetosphere remains unkown. Eventually, we could investigate the magnetospheric dynamics during LRP phenomenon as well as its relation to Alfvén waves. Also, work could be done as an attempt to find out the significance and causes of duskside enhancement.

The comprehension of the energy tranfer mechanisms related to the magnetosphere and solar wind interaction as well as the processes within magnetospheric dynamics would permit space weather predictions. The solar wind input energy could be a manner of monitoring energy deposition in the magnetosphere by a satellite located in front of the magnetosphere, in the upstream solar wind. This way, the coupling energy amount during a magnetic storm could be predicted before the event reaches the magnetosphere and, therefore, it would become possible to monitor continuously the space weather. However, current space physics knowledge is not enough to achieve such accomplishment. This

work has been only a small step in this vast research field.

REFERENCES

AHN, B.; AKASOFU, S.; KAMIDE, Y. The joule heating production and the particle energy injection rate as a function of the geomagnetic indices AE and AL. **Journal of Geophysical Research**, v. 88, n. A8, p. 6275–6287, Aug. 1983. 64, 98

AKASOFU, S.-I. The development of the auroral substorm. **Planetary and Space Science**, v. 12, n. 4, p. 273–282, 1964. 3

_____. Energy coupling between the solar wind and the magnetosphere. **Space Science Reviews**, v. 28, n. 2, p. 121–190, Feb. 1981. 64, 81, 82, 86, 87, 99

ALVES, M.; ECHER, E.; GONZALEZ, W. Geoeffectiveness of corotating interaction regions as measured by Dst. **Journal of Geophysical Research**, v. 111, p. A07S05, May 2006. 5

BAKER, D. What is space weather? **Advances in Space Research**, v. 22, n. 1, p. 7–16, 1998. 97

BRITTNACHER, M.; FILLINGIM, M.; PARKS, G. Polar cap area and boundary motion during substorms. **Journal of Geophysical Research**, v. 104, n. A6, p. 12,251–12,262, June 1999. 9

BURLAGA, L. **Interplanetary magnetohydrodynamics**. [S.l.]: Oxford University Press, 1995. 1, 88

CHUA, D.; PARKS, G.; BRITTNACHER, M.; GERMANY, G.; SPANN, J. Auroral substorm timescales: Imf and seasonal variations. **Journal of Geophysical Research**, v. 109, p. A03207, March 2004. 9

CORONITI, F.; MCPHERRON, R.; PARKS, G. Concept of the magnetospheric substorms and its relation to electron precipitating and micropulsations. **Journal of Geophysical Research**, v. 73, n. 5, March 1968. 9

CRAVEN, J. D.; NICHOLAS, A. C.; FRANK, L. A.; STRICKLAND, D. J.; IMMEL, T. J. Variations in the fuv dayglow after intense auroral activity. **Geophysical Research Letters**, v. 21, n. 25, p. 2793–2796, Dec 1994. 12

DAVIS, T.; SUGIURA, M. Auroral electrojet activity index ae and its universal time variations. **Journal of Geophysical Research**, v. 71, n. 3, p. 785, 1966. 3, 31

ECHER, E.; GONZALEZ, W.; GUARNIERI, F.; LAGO, A. D.; VIEIRA, L. Introduction to space weather. **Advances in Space Research**, v. 35, p. 855–865, 2005. 90, 97

EDDY, J.; GILMAN, P.; TROTTER, D. Introduction to space weather. **Solar Physics**, v. 46, n. 1, p. 3–14, 1976. 88

EMERY, B. A.; COUMANS, V.; EVANS, D.; GERMANY, G. A.; GREER, M. S.; HOLEMAN, E.; KADINSKY-CADE, K.; RICH, F. J.; XU, W. Seasonal, kp, solar wind, and solar flux variations in long-term single pass satellite estimates of electron and ion auroral hemispheric power. **Journal of Geophysical Research**, 2008. 65

EMERY, B. A.; EVANS, D.; GREER, M. S.; HOLEMAN, E.; KADINSKY-CADE, K.; RICH, F. J.; XU, W. **The low energy auroral electron and ion hemispheric power after NOAA and DMSP Intersatellite Adjustments**: Ncar technical note. 2006. Available from: <http://cedarweb.hao.ucar.edu/>. Access in: fev. 2008. 29, 65

FILLINGIM, M.; PARKS, G.; CHEN, L.; BRITTNACHER, M.; GERMANY, G.; SPANN, J.; LARSON, D.; LIN, R. Coincident polar/uvi and wind observations of pseudobreakups. **Geophysical Research Letters**, v. 27, n. 9, p. 1,379–1,382, May 2000. 9

FILLINGIM, M.; PARKS, G.; CHEN, L.; MCCARTHY, M.; SPANN, J.; LIN, R. Comparison of plasma sheet dynamics during pseudobreakups and expansive aurorae. **Physics of plasmas**, v. 8, n. 4, p. 1,127–1,132, Apr. 2001. 9

FILLINGIM, M.; PARKS, G.; FREY, H.; IMMEL, T.; MENDE, S. High asymmetry of the afternoon electron aurora. **Geophysical Research Letters**, v. 32, p. L03113, Feb. 2005. 10

FREY, H. U. Localized aurora beyond the auroral oval. **Reviews of Geophysics**, v. 45, n. 1, p. RG1003, March 2007. 7, 73

GERMANY, G. A.; TORR, M. R.; RICHARDS, P. G.; TORR, D. G. The dependence of modeled OI 1356 and N_2 Lyman Birge Hopfield auroral emissions on the neutral atmosphere. **Journal of Geophysical Research**, v. 95, n. A6, p. 7725–7733, June 1990. xvi, 19, 20, 26

GERMANY, G. A.; TORR, M. R.; TORR, D. G.; RICHARDS, P. G. Use of FUV auroral emissions as diagnostic indicators. **Journal of Geophysical Research**, v. 99, n. A1, p. 383–388, Jan 1994. 19, 20

_____. Auroral observations from the polar ultraviolet imager (uvi). **AGU monograph**, 1998. 18, 19, 20, 21, 22, 23

GOMBOSI, T. I.; POWELL, K. G.; ZEEUN, D. L. de; CLAUER, C. R.; HANSEN, K. C.; MANCHESTER, W. B.; ROUSSEV, A. J. R. I. I.; SOKOLOV, I. V.; STOUT, Q. F.; TÓTH, G. Solution-adaptive magnetohydrodynamics for space plasmas:sun-to-earth simulations. **Journal Computing in Science and Engineering**, v. 6, p. 14–35, 2004. 97

GONZALEZ, W. A unified view of solar-wind magnetosphere coupling functions. **Planetary and Space Science**, v. 38, n. 5, p. 627–632, 1990. 81

GONZALEZ, W.; JOSELYN, J. A.; KAMIDE, Y.; KROEHL, H. W.; ROSTOKER, G.; TSURUTANI, B. T.; VASYLIUNAS, V. M. What is a geomagnetic storm? **Journal of Geophysical Research**, v. 99, n. A4, p. 5771–5792, 1994. 2, 3, 4, 5, 32

GUARNIERI, F. L. **Estudo da origem interplanetária e solar de eventos de atividade auroral contíua e de longa duracão**. (INPE-13604-TDI/1043). Tese de doutorado em Geofísica Espacial — Instituto Nacional de Pesquisas Espaciais (INPE), São José dos Campos, 2006. 31

IYEMORI, T. Storm-time magnetospheric currents inferred from mid-latitude magnetic field variations. **J. Geomag. Geoelectr.**, v. 42, p. 1,249–1,265, 1990. 31

JACOBS, J. A. **Geomagnetism**. London: Academic Press, 1987. 55

KAMIDE, Y.; BAUMJOHANN, W.; DAGLIS, I.; GONZALEZ, W.; GRANDE, M.; JOSELYN, J.; MCPHERRON, R.; PHILIPS, J.; REEVES, E.; ROSTOKER, G.; SHARMA, A.; SINGER, H.; TSURUTANI, B.; VASYLIUNAS, V. Current understanding of magnetic storms: storm-substorm relationships. **Journal of Geophysical Research**, v. 103, n. A8, p. 17705–17728, 1998. 3

KAMIDE, Y.; ROSTOKER, G. What is the physical meaning of the ae index? **Transactions American Geophysical Union**, v. 85, n. 19, p. 188, May 2004. 31

KEILING, A.; WYGANT, J.; CATELL, C.; TEMERIN, M.; MOZER, F.; KLETZING, C.; SCUDDER, J.; RUSSELL, C.; LOTKO, W.; STRELTSOV, A. Large alfvén wave power in the plasma sheet boundary layer during the expansion phase of substorms. **Geophysical Research Letters**, v. 27, n. 19, p. 3,169–3,172, Oct. 2000. 10

KEILING, A.; WYGANT, J.; CATELL, C.; PERIA, W.; PARKS, G.; TEMERIN, M.; MOZER, F.; RUSSELL, C.; KLETZING, C. Correlation of alfvén wave poyinting flux in the plasma sheet at 4-7 r_e with ionospheric energy flux. **Journal of Geophysical Research**, v. 107, n. A7, p. 1132, July 2002. 10

KIM, H.-J.; LEE, D.; LYONS, L. Are repetitive particle injections during high-speed solar wind streams classic substorms? **Journal of Geophysical Research**, v. 113, p. A08205, Aug 2008. 6

KIVELSON, M. G.; RUSSEL, C. T. **Introduction to space physics**. [S.l.]: Cambridge University Press, 1995. 1, 2, 7, 73, 88, 97

KOSKINEN, H. E.; TANSKANEN, E. I. Magnetospheric energy budget and epsilon parameter. **Journal of Geophysical Research**, v. 107, n. A11, p. 1415, Nov. 2002. 82

KOZYRA, J.; JORDANOVA, V.; HORNE, R.; THORNE, R. Modeling of the contribution of electromagnetic ion cyclotron (emic) waves to stormtime ring current erosion. In: TSURUTANI, B.; GONZALEZ, W.; KAMIDE, Y.; ARBALLO, J. (Ed.). **Magnetic storms**. Washington DC: American Geophysical Union Press, 1997. p. 187. 97

KOZYRA, J.; LIEMOHN, M.; CLAUER, C.; RIDLEY, A.; TOMSEN, M.; BOROVSKY, J.; ROEDER, J.; JORDANOVA, V.; GONZALEZ, W. Multistep dst development and ring current compositional changes during the 4-6 june 1991 magnetic storm. **Journal of Geophysical Research**, v. 107, n. A8, 2002. 97

KYOTO. **World Data Center for Geomagnetism**. 2010. Available from: <http://wdc.kugi.kyoto-u.ac.jp/>. Access in: 2010. 32

LEE, D.-Y.; LYONS, L.; KIM, K.; BAEK, K.-H. K. J.-H.; KIM, H.J.; WEYGAND, J.; MOON, Y.; CHO, K.-S.; PARK, Y.; HAN, W. Repetitive substorms caused by alfvénic waves of the interplanetary magnetic field during high-speed solar streams. **Journal of Geophysical Research**, v. 111, p. A12214, Dec 2006. 6

LUMMERZHEIM, D.; BRITTNACHER, M.; EVANS, D.; GERMANY, G.; PARKS, G.; REES, M.; SPAN, J. High time resolution study of the hemispheric power carried by electrons into the ionosphere during the may 19/20, 1996 auroral activity. **Geophysical Research Letters**, v. 24, n. 8, p. 987–990, April 1997. 8

MCPHERRON, R.; PARKS, G.; CORONITI, F.; WARD, S. Correlated magnetic micropulsations and electron precipitating occurring during auroral substorms. **Journal of Geophysical Research**, v. 73, n. 5, March 1968. 9

MCPHERRON, R. L. Magnetospherics substorms. **Reviews of Geophysics and Space Physics**, v. 17, n. 4, p. 657, Jun 1979. 3

MEIER, R. R. Ultraviolet spectroscopy and remot sensing of the upper atmosphere. **Space Science Reviews**, v. 58, n. 1, p. 1–185, 1991. 11, 12, 13

MEIER, R. R.; WARREN, H. P.; NICHOLAS, A. C.; BISHOP, J.; RUBA, J. D.; DROB, D. P.; LEAN, J. L.; PICONE, J. M.; MARISKA, J. T.; JOYCE, G.; JUDGE, D. L.; THONNARD, S. E.; DYMOND, K. F.; BUDZIEN, S. A. Ionospheric and dayglow responses to the radiative phase of the bastille day flare. **Geophysical Research Letters**, v. 29, n. 10, p. 1461, May 2002. 14

NASA. **International Solar Terrestrial Physics (ISTP)**. Access in: http://pwg.gsfc.nasa.gov/istp/admin/proinfo.html. 17

_____. **Polar spacecraft**. Access in: http://pwg.gsfc.nasa.gov/polar. 17

_____. **Ultraviolet Imager (UVI)**. Access in: http://tideuvira.nsstc.nasa.gov/uvi. 18

NOAA. **How the auroral activity patterns are created**. 2007. Available from: <http://www.swpc.noaa.gov/pmap/BackgroundInfo.html>. Access in: 2007. 29

OSTGAARD, N.; MENDE, S.; FREY, H.; SIGWARTH, J.; ASNES, A.; WEYGAND, J. Auroral conjugacy studies based on global imaging. **Journal of Atmospheric and Solar-terrestrial physics**, v. 69, p. 249–255, 2007. 10

OSTGAARD, N.; R.R.VONDRAK; J.W.GJERLOEV; G.GERMANY. A relation between the energy deposition by electron precipitation and geomagnetic indices during substorms. **Journal of Geophysical Research**, v. 107, n. A9, Sep. 2002. 64, 81, 98

OSTGAARD, N.; STADSNES, J.; BJORDAL, J.; G.GERMANY; R.R.VONDRAK; PARKS, G.; CUMMER, S.; CHENETTE, D.; PRONKO, J. Auroral electron distributions derived fom combined uv and x-rays emissions. **Journal of Geophysical Research**, v. 106, n. A11, p. 26,081–26,089, Nov. 2001. 8

PARKS, G.; BRITTNACHER, M.; CHUA, D.; FILLINGIM, M.; GERMANY, G.; SPANN, J. Behavior of the aurora during 10-12 may, 1999 when the solar wind nearly disappeared. **Geophysical Research Letters**, v. 27, n. 24, p. 4,033–4,036, Dec. 2000. 10

107

PARKS, G.; CHEN, L.; FILLINGIM, M.; LIN, R.; LARSON, D.; MCCARTHY, M. A new framework for studying the relationship of aurora and plasma sheet dynamics. **Journal of Atmospheric and Solar-terrestrial physics**, v. 64, p. 115–124, 2002. 9

PARKS, G.; CORONITI, F.; MCPHERRON, R.; ANDERSON, K. A relation between the energy deposition by electron precipitation and geomagnetic indices during substorms. **Journal of Geophysical Research**, v. 73, n. 5, March 1968. 9

PARKS, G. K. **Physics of space plasmas**. [S.l.]: Westview Press, 2004. 1

PERREAULT, P.; AKASOFU, S. Study of geomagnetic storms. **Geophysical Journal of the Royal Astronomical Society**, v. 54, n. 3, p. 547–573, 1978. 81

PULKKINEN, T. Space weather: Terrestrial perspective. **Living Review Solar Physics**, v. 4, n. 1, May 2007. Available from: <http://solarphysics.livingreviews.org/Articles/lrsp-2007-1/>. 97

ROSTOKER, G. Geomagnetic indices. **Reviews of Geophysics and Space Physics**, v. 10, n. 4, p. 935–950, Nov 1972. 3, 31

RUSSEL, C. T. Planetary Magnetospheres. **UCLA-IGPP Space Physics Tutorial**, v. 75, p. 93–105, 1991. 2

SCHWENN, R. Space weather: The solar perspective. **Living Review Solar Physics**, v. 3, n. 2, p. 1–72, 2006. 97

SHARMA, A.; BAKER, D.; GRANDE, M.; KAMIDE, Y.; LAKHINA, G.; MACPHERRON, R.; REEVES, G.; ROSTOKER, G.; VONDRAK, R.; ZELENYI, L. The storm-substorm relationship: current understanding and outlook. In: SHARMA, A. S.; KAMIDE, Y.; LAKHINA, G. S. (Ed.). **Disturbances in geospace: the storm-substorm relationship**. Washington D.C.: American Geophysical Union, 2003. p. 1–14. 3

SHARMA, A. S.; KAMIDE, Y.; LAKHINA, G. S. **Disturbances in geospace: the storm-substorm relationship**. [S.l.]: American Geophysical Union, 2003. 3, 6

SISCOE, G. The space-weather enterprise: past, present, and future. **Journal of Atmospheric and Solar-terrestrial physics**, v. 62, p. 1,223–1,232, 2000. 97

SORAAS, F.; AARSNES, K.; OKSAVIK, K.; SANDANGER, M.; EVANS, D.; GREER, M. Evidence for particle injection as the cause of dst reduction during hildcaa events. **Journal of Atmospheric and Solar-terrestrial physics**, v. 66, p. 177–186, 2004. 5

STORMER, C. **The polar aurora**. Oxford: Clarendon Press, 1955. 7

SUGIURA, M. Hourly values of equatorial dst for the igy. **Ann. Int. Geophys. Year**, v. 35, n. 9, 1964. 2, 31

TORR, M. R.; TORR, D. G.; ZUKIC, M.; JOHNSON, R. B.; AJELLO, J.; BANKS, P.; CLARK, K.; COLE, K.; KEFFER, C.; PARKS, G.; TSURUTANI, B.; SPANN, J. A far ultraviolet imager for the international solar terrestrial physics mission. **Planetary and Space Science**, v. 71, p. 329–383, 1995. 17, 18, 19

TSURUTANI, B. T.; GONZALEZ, W. D. The cause of high-intensity long duration ae activity (HILDCAAS): Interplanetary alfvén wave trains. **Planetary and Space Science**, v. 35, n. 4, p. 405–412, 1987. 3, 4, 15, 30, 31, 86, 90, 97, 99, 100

TSURUTANI, B. T.; GONZALEZ, W. D.; GONZALEZ, A. L.; TANG, F.; ARBALLO, J. K.; OKADA, M. Interplanetary origin of geomagnetic activity in the declining phase of the solar cycle. **Journal of Geophysical Research**, v. 100, n. A11, p. 21,717–21,733, Nov. 1995. 6

TSURUTANI, B. T.; GONZALEZ, W. D.; GONZALEZ, A. L.; GUARNIERI, F. L.; GROPALSWAMY, N.; GRANDE, M.; KAMIDE, Y.; KASAHARA, Y.; LU, G.; MANN, I.; MCPHERRON, R.; SORAAS, F.; VASYLIUNAS, V. Corotating solar wind streams and recurrent geomagnetic activity: a review. **Journal of Geophysical Research**, v. 11, n. A7, p. A07S01, Jun 2006. 5

TSURUTANI, B. T.; GONZALEZ, W. D.; GUARNIERI, F. L.; KAMIDE, Y.; ZHOU, X.; ARBALLO, J. K. Are high-intensity long-duration ae activity (hildcaa) events substorm expansion events? **Journal of Atmospheric and Solar-terrestrial physics**, v. 66, n. 2, p. 167–176, 2004. 4, 6

TSURUTANI, B. T.; GOULD, T.; GOLDSTEIN, B. E.; GONZALEZ, W. D.; SUGIURA, M. Interplanetary alfvén waves and auroral (substorm) activity: Imp-8. **Journal of Geophysical Research**, v. 95, p. 2241, 1990. 4

TSURUTANI, B. T.; HO, C. M.; ARBALLO, J. K.; GOLDSTEIN, B. E. Large amplitude imf flutuations in corotating interactions regions: Ulysses at midlatitudes and andre balogh. **Geophysical Research Letters**, v. 22, n. 23, p. 3397–3400, Dec. 1995. 5, 100

WYGANT, J.; KEILING, A.; CATTELL, C.; JOHNSON, M.; LYSAK, R.; TEMERIN, M.; MOZER, F.; KLETZING, C.; SCUDDER, J.; PETERSON, W.; RUSSELL, C.;

PARKS, G.; BRITTNACHER, M.; GERMANY, G.; SPANN, J. Polar spacecraft based comparisons of intense electric fields and poynting flux near and within the plasma sheet-tail lobe boundary to uvi images: An energy source of the aurora. **Journal of Geophysical Research**, v. 105, n. A8, p. 18,675–18,692, Aug. 2000. 10, 11

APPENDIX A - Sector energy flux versus UT

Figures A.1 to A.12 bring energy flux, calculated for each invariable sector area of $10°$ ML (Magnetic Latitude) and 3h LT (Local Time), versus UT (Universal Time) for events 1, 3, 5 and 6. Auroral region extends from $50°$ to $90°$ ML.
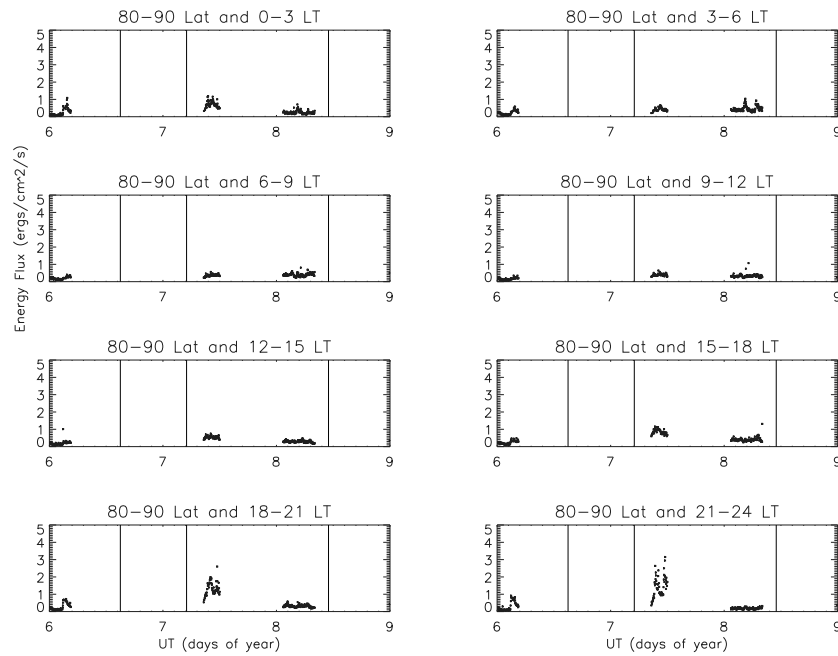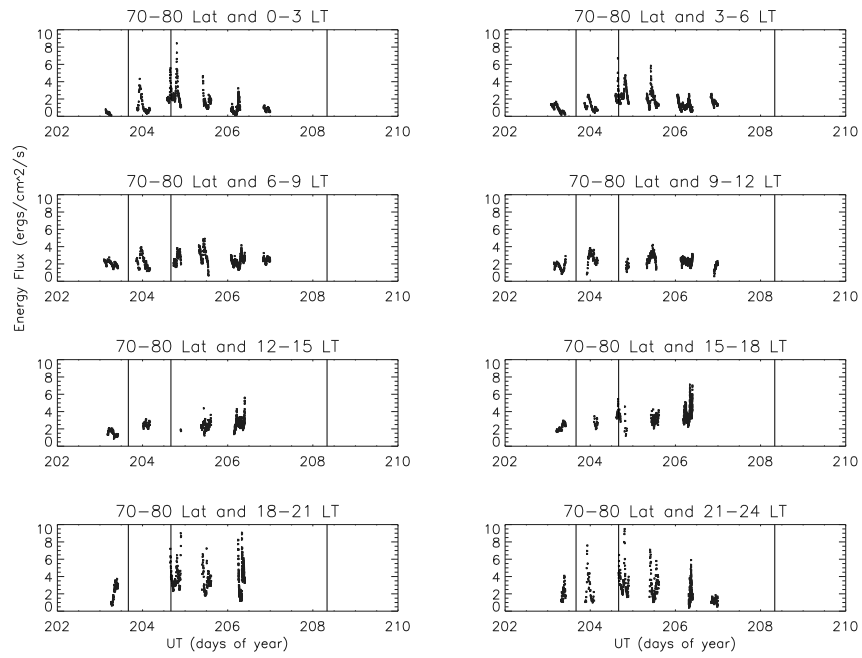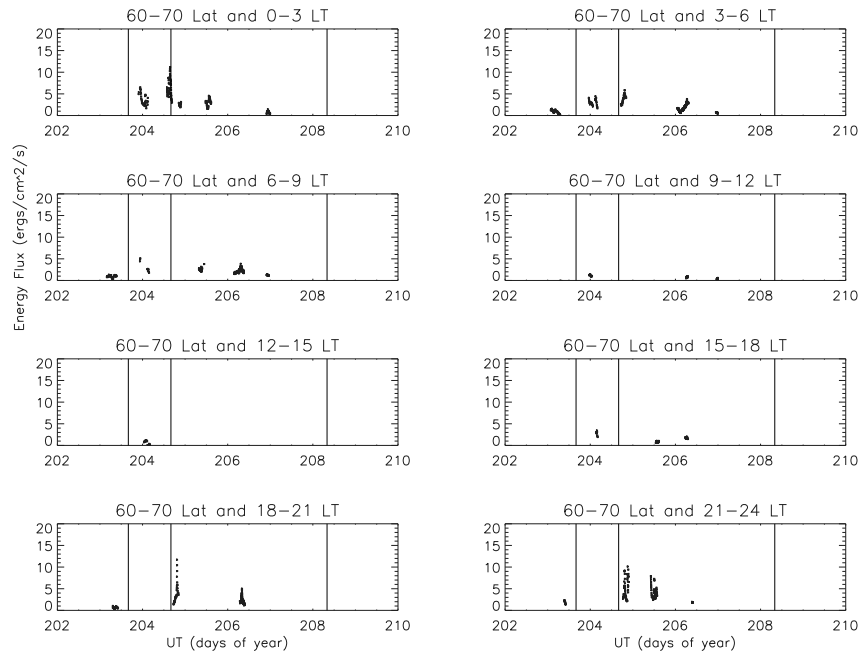

Figure A.1 - Energy flux computed from 80 to $90°$ magnetic latitude for each 3h LT. January 6-8, 1998, SRP (Event 1).
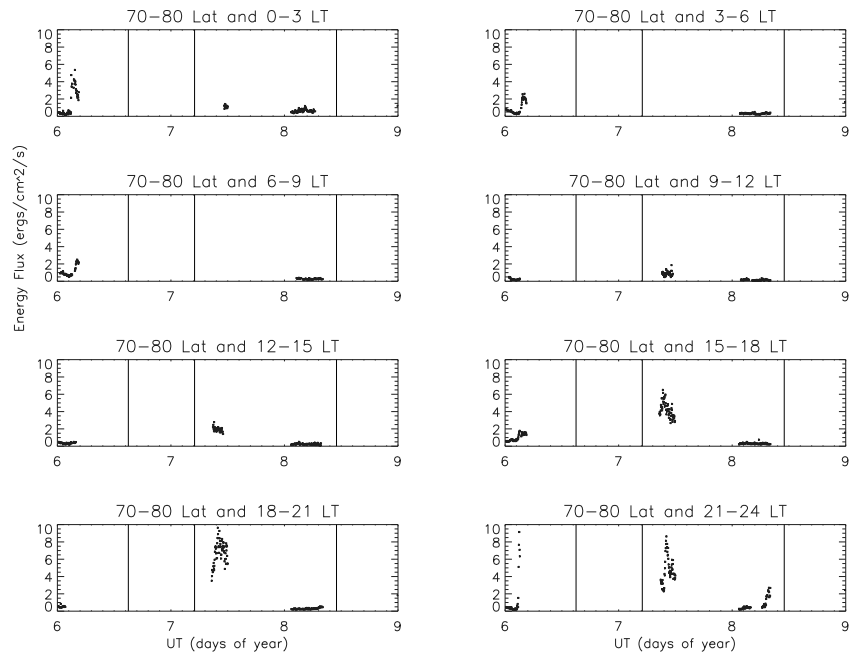
Figure A.2 - Energy flux computed from 70 to 80° magnetic latitude for each 3h LT. January 6-8, 1998, SRP (Event 1).
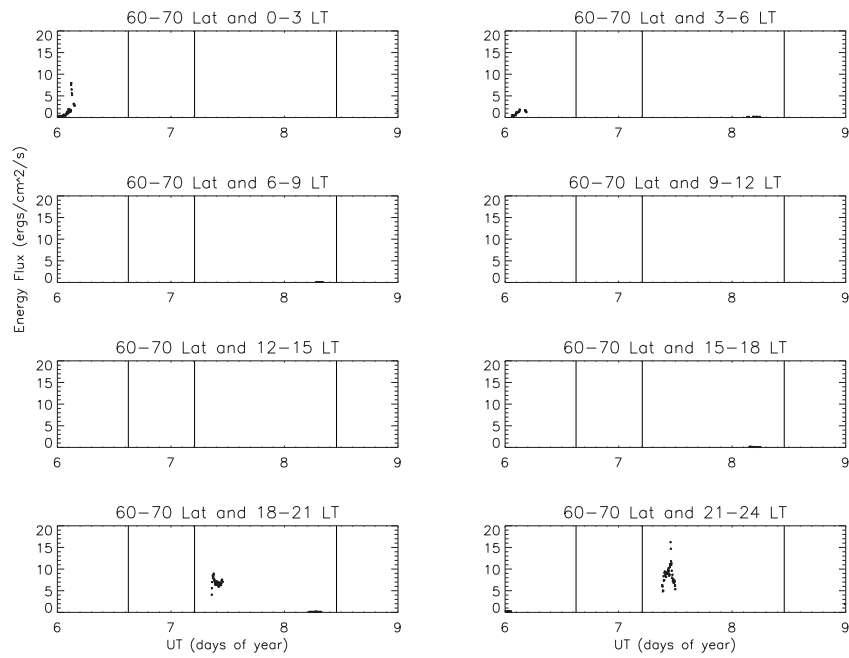
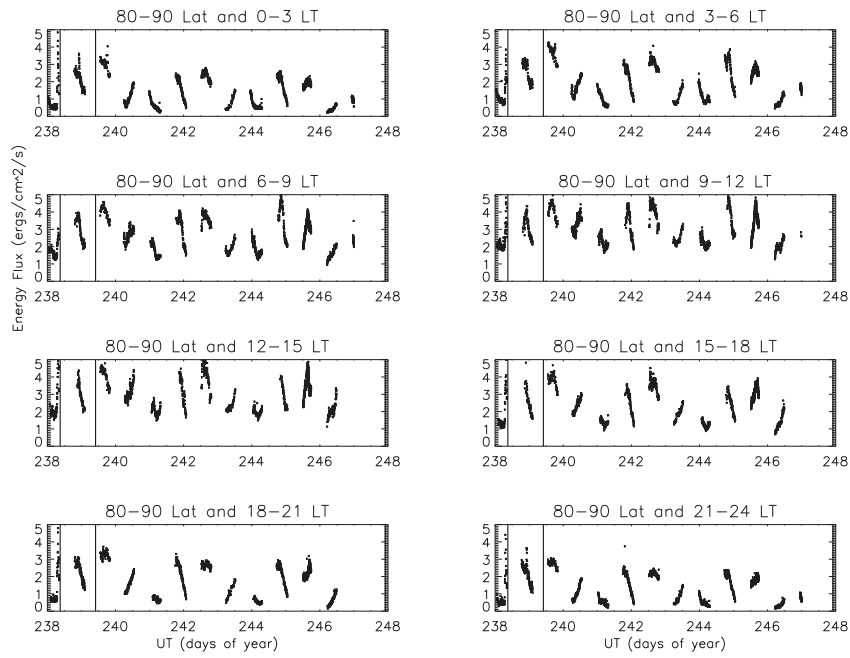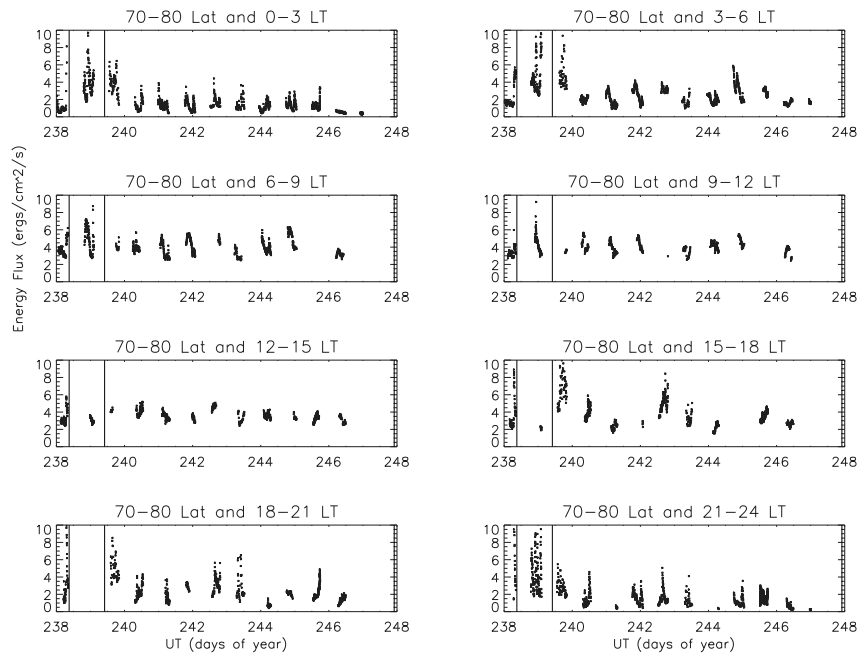Figure A.3 - Energy flux computed from 60 to 70° magnetic latitude for each 3h LT. January 6-8, 1998, SRP (Event 1).
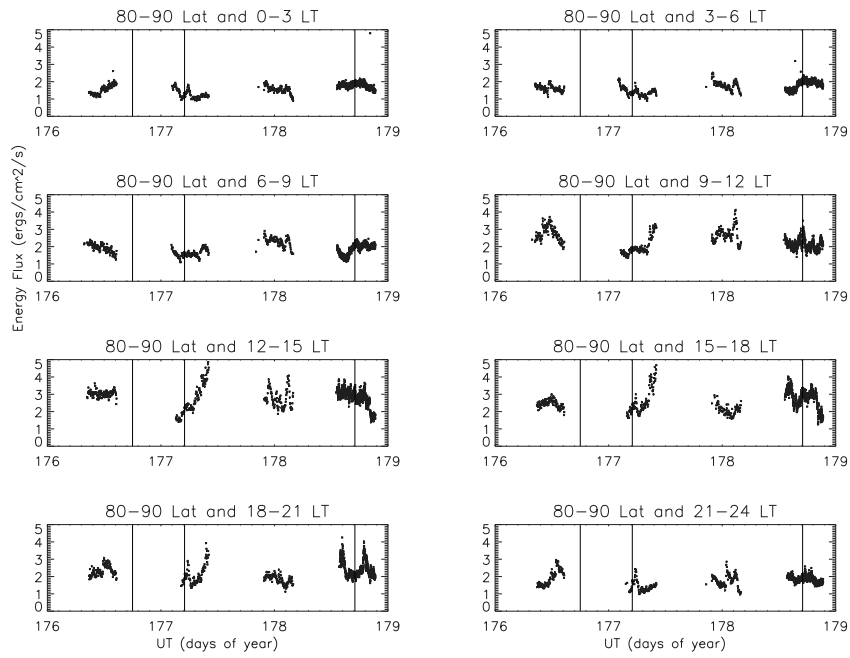
Figure A.4 - Energy flux computed from 80 to 90° magnetic latitude for each 3h LT. June 25-27, 1998, SRP (Event 3).
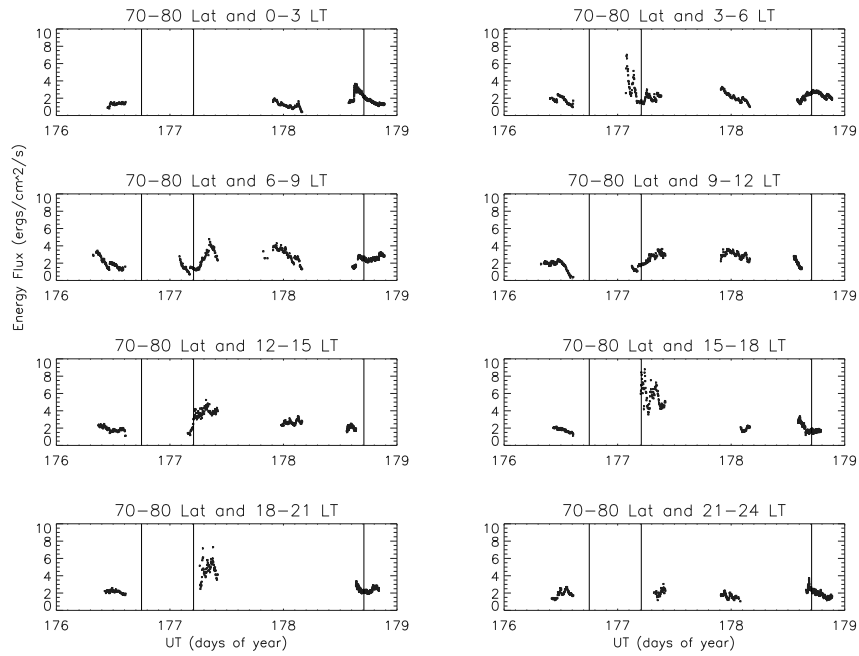
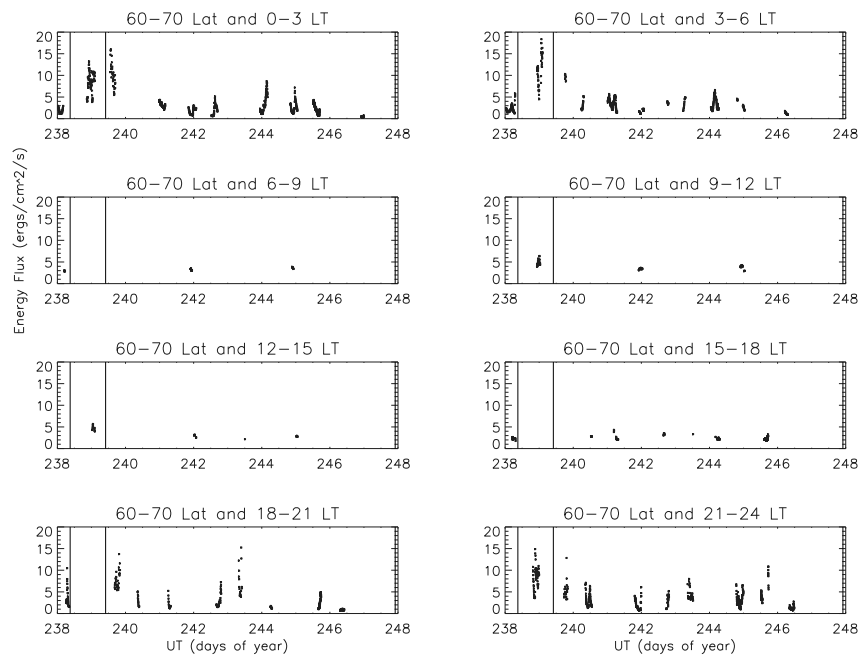Figure A.5 - Energy flux computed from 70 to 80° magnetic latitude for each 3h LT. June 25-27, 1998, SRP (Event 3).
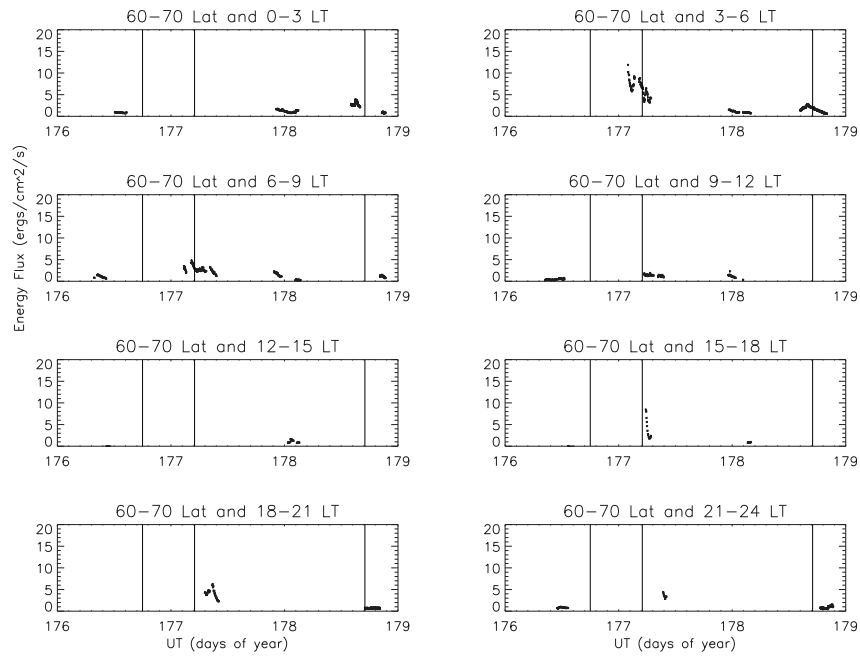
Figure A.6 - Energy flux computed from 60 to 70° magnetic latitude for each 3h LT. June 25-27, 1998, SRP (Event 3).
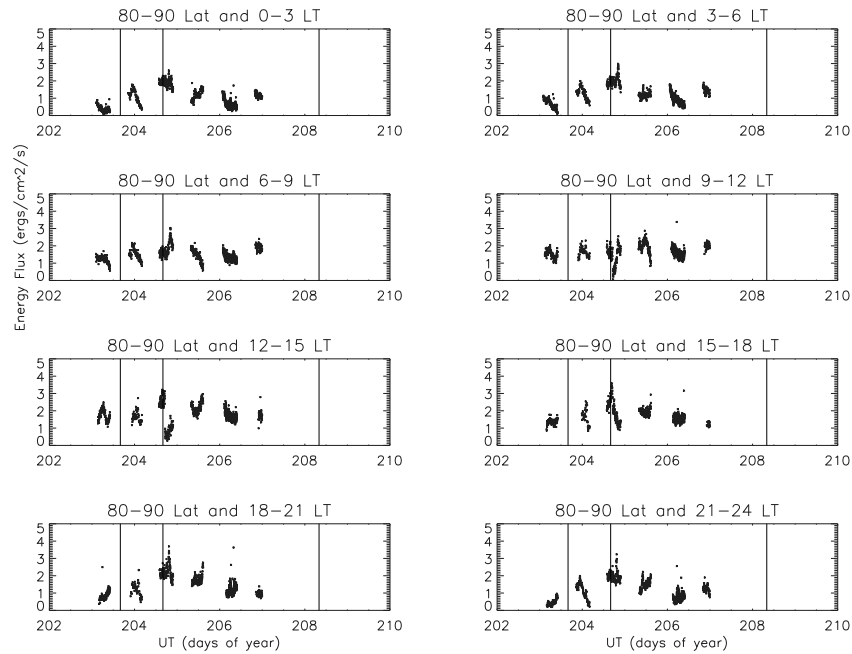
Figure A.7 - Energy flux computed from 80 to 90° magnetic latitude for each 3h LT. July 22-29, 1998, LRP (Event 5).

116

Figure A.8 - Energy flux computed from 70 to 80° magnetic latitude for each 3h LT. July 22-29, 1998, LRP (Event 5).

Figure A.9 - Energy flux computed from 60 to 70° magnetic latitude for each 3h LT. July 22-29, 1998, LRP (Event 5).

Figure A.10 - Energy flux computed from 80 to 90° magnetic latitude for each 3h LT. August 26 to September 3rd, 1998, LRP (Event 6).

Figure A.11 - Energy flux computed from 70 to 80° magnetic latitude for each 3h LT. August 26 to September 3rd, 1998, LRP (Event 6).

Figure A.12 - Energy flux computed from 60 to 70° magnetic latitude for each 3h LT. August 26 to September 3rd, 1998, LRP (Event 6).

APPENDIX B - Energy flux versus Local time sectors

Figures B.1 and B.4 display energy flux versus LT sector number for each 10° ML during main and recovery phase for a SRP and LRP magnetic storms. Sector number refer to 3h LT intervals starting at midnight (0 LT). Then, sectors 1, 2, 7 and 8 are located in the nightside while 3 to 6 sector numbers refer to the dayside.
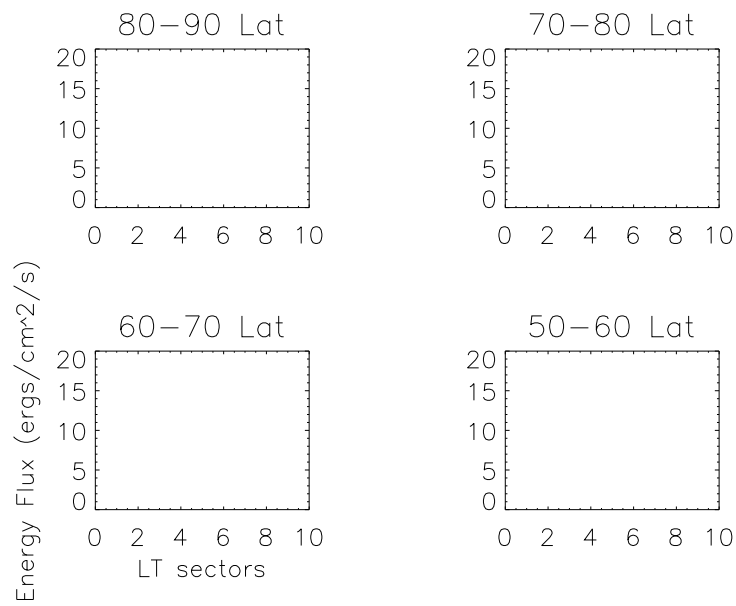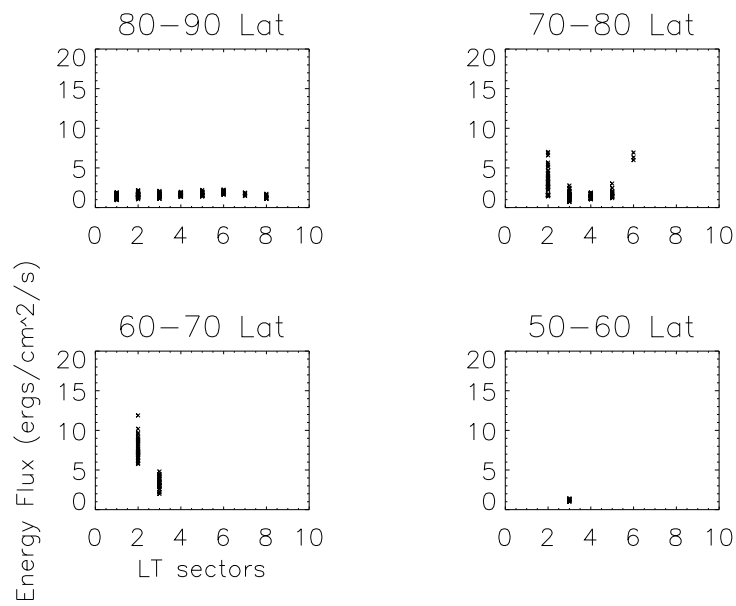
(a) Main phase
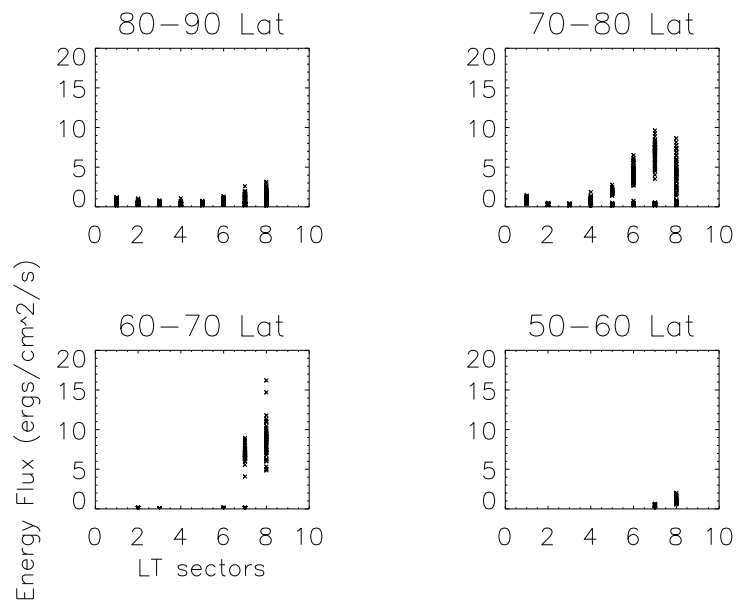
(b) Recovery phase

Figure B.1 - Energy flux versus LT sector number for each 10° ML. Sector number refer to 3h LT intervals starting at midnight (0 LT). SRP (event 1)
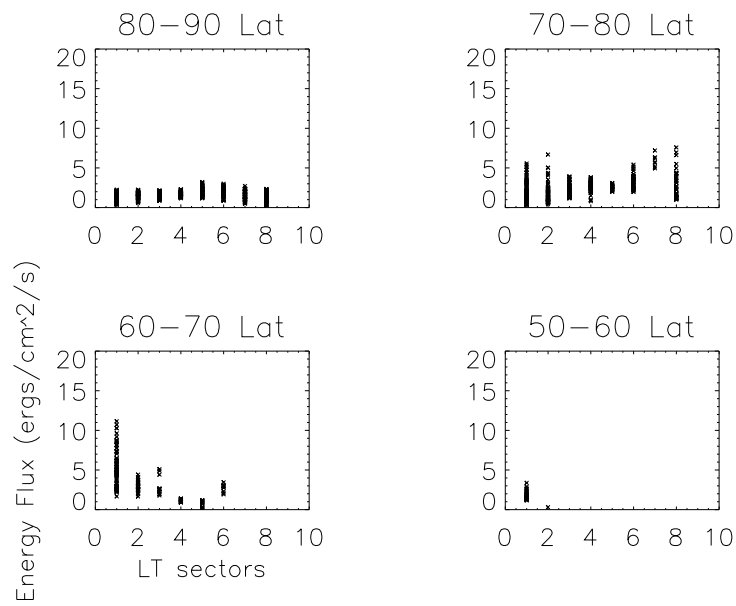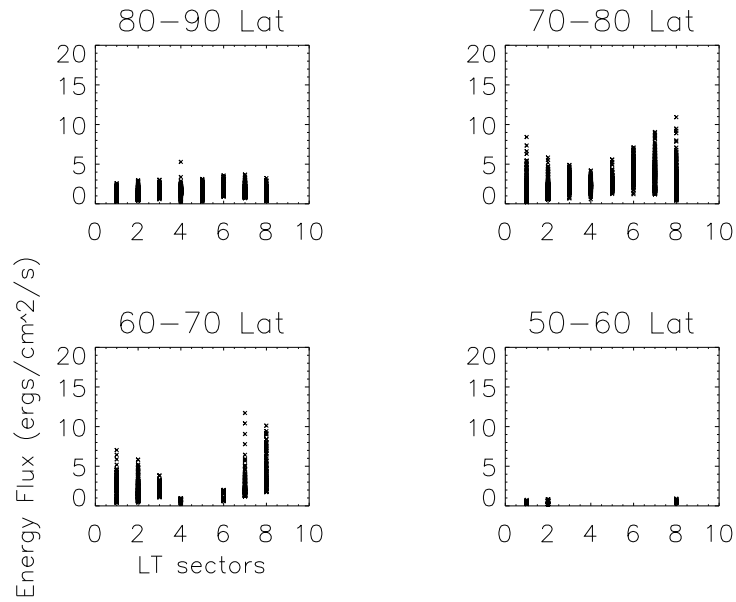
(a) Main phase
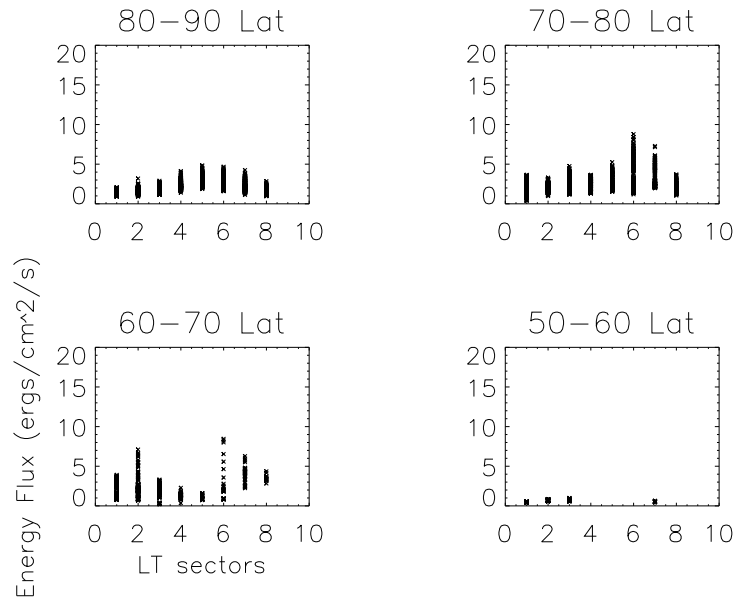
(b) Recovery phase

Figure B.2 - Energy flux versus LT sector number for each 10° ML. Sector number refer to 3h LT intervals starting at midnight (0 LT). SRP (event 3)
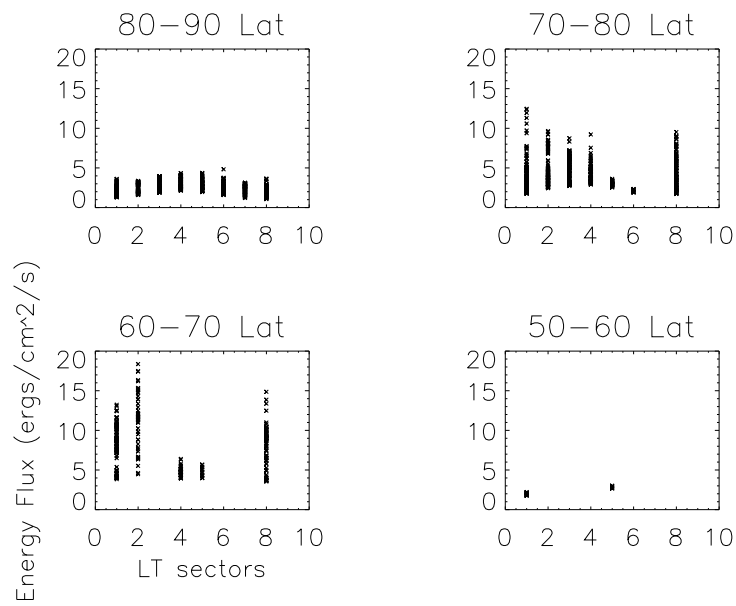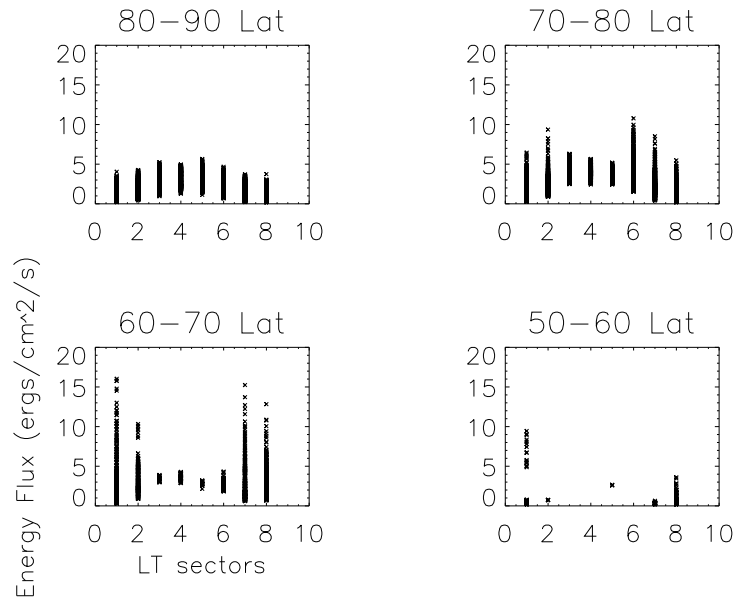
(a) Main phase

(b) Recovery phase

Figure B.3 - Energy flux versus LT sector number for each 10° ML. Sector number refer to 3h LT
intervals starting at midnight (0 LT). SRP (event 5)

124

(a) Main phase

(b) Recovery phase

Figure B.4 - Energy flux versus LT sector number for each 10° ML. Sector number refer to 3h LT intervals starting at midnight (0 LT). SRP (event 6)